Spring 2010

Beyond the Born Approximation: A Precise Comparison of e+p and e-p Elastic Scattering in the CEBAF Large Acceptance Spectrometer (CLAS)

Megh Raj Niroula
Old Dominion University

BEYOND THE BORN APPROXIMATION: A PRECISE COMPARISON OF e^+p AND e^-p ELASTIC SCATTERING IN THE CEBAF LARGE ACCEPTANCE SPECTROMETER (CLAS)

by

Megh Raj Niroula
M.S. May 2005, Old Dominion University

A Dissertation Submitted to the Faculty of
Old Dominion University in Partial Fulfillment of the
Requirement for the Degree of

DOCTOR OF PHILOSOPHY

PHYSICS

OLD DOMINION UNIVERSITY
May 2010

Approved by:

Lawrence B. Weinstein (Director)

Charles I. Sukenik

Gail E. Dodge

Hari Areti

Scott R. Sechrist

ABSTRACT

BEYOND THE BORN APPROXIMATION: A PRECISE COMPARISON OF e^+p AND e^-p ELASTIC SCATTERING IN THE CEBAF LARGE ACCEPTANCE SPECTROMETER (CLAS)

Megh Raj Niroula
Old Dominion University, 2010
Director: Dr. Lawrence B. Weinstein

How well we know the structure of the proton depends on our knowledge of the form factors of the proton. The ratio of the electromagnetic form factors of the proton measured by the Rosenbluth and the polarization transfer methods differ by a factor of 3 at four momentum transfer squared (Q^2)=5.6 GeV^2. The two photon exchange (TPE) effect is the leading candidate to explain this discrepancy. The theoretical estimates of the TPE effect are model dependent so precise measurement is required to resolve this problem. The TPE effect can be measured in a model independent way by measuring the ratio of positron-proton to electron-proton elastic scattering cross-sections. We produced a simultaneously mixed electron-positron beam in the engineering test run conducted in October 2006 and measured the e^+p/e^-p ratio using the CEBAF large acceptance spectrometer (CLAS). Due to the luminosity constraint our kinematic coverage is limited to low Q^2 and high ε (longitudinal polarization of the virtual photon). We continued our background study through GEANT4 simulation developed for the test run design in order to find more background sources and to design required shielding. The simulation is validated by using the test run data and is used further to optimize the luminosity for the final experiment. We are able to increase the luminosity by an order of magnitude for the upcoming final run. The final experiment will extend the data in high Q^2 and low ε region where TPE effect is expected to be large.

ACKNOWLEDGMENTS

This dissertation would not have been possible without help from various people. First and foremost, I wish to express my sincere gratitude to my advisor Larry Weinstein for giving me inspiration and guidance during my research work. I am very thankful to him for investing a lot of time teaching me. I would also like to thank Larry and his wife Carol for providing very important suggestions regarding my personal life. I will never forget their valuable suggestions while I was going through a very difficult time.

I am grateful to Hari Areti for his help and support while I was new at Jefferson Lab. I would like to thank him for his encouragement and advice during my entire graduate study years.

I would like to thank all the members of my dissertation committee: Gail Dodge, Charles Sukenik, Hari Areti, and Scott Sechrist for their valuable comments on this dissertation. I am also grateful to all the professors at Old Dominion University for being very friendly and teaching exciting physics. I would like to acknowledge Mark Havey as one the best professors I have ever taken classes with. I would like to thank Wally Melnitchouk at Jefferson Lab for a great discussion on two photon exchange physics.

I would like to thank all my collegues at Old Dominion University for their friendships. My special thanks goes to Jixie for sharing his computer programming skills.

I would like to thank my family, specially my parents who send me to college for my better future. I can not forget my brother Krishna who is my first teacher and role model due to which I am here today. He taught me to smile even in difficult times. Finally, I wish to thank my son Miraj for his patience throughout this work, and my loving wife Rekha for her selfless support.

TABLE OF CONTENTS

LIST OF TABLES

LIST OF FIGURES

CHAPTER I

INTRODUCTION

I.1 OVERVIEW

When the proton and the neutron were discovered, they were considered to be point like, without any internal structure. So they should each have Dirac magnetic moment [1] $\mu_D = \frac{q}{mc}|\vec{s}|$ where q, m and s are the electric charge, mass and the spin of the particle. According to this assumption, the magnetic moment of the neutron should be zero because the neutron has zero charge. But the nucleons' magnetic moments are $\mu_p = 2.79\mu_N$ and $\mu_n = -1.91\mu_N$ where $\mu_N = \frac{e\hbar}{2M_p} = 3.1525 \times 10^{-14}$ MeV T^{-1} is the nuclear magneton. This is the first evidence for nucleon substructure. Thus protons and neutrons, which were considered to be the fundamental constituents of matter, are themselves composite particles made up of smaller particles called quarks and gluons. At the current understanding of our knowledge, the leptons, quarks and gluons are the basic fundamental building blocks of all the particles in nature.

Electron scattering experiments were used to reveal the underlying structure of the nucleon. The electron is a point like particle and has no internal structure which makes it a very clean probe to study the target nucleus. In this kind of process, the electron scatters off a nuclear target by exchanging a single virtual photon. The electron-photon vertex does not involve any structure since both are point like particles so one can calculate the amplitude of the process within the frame work of Quantum Electrodynamics (QED). So the information extracted from this interaction reflects only the structure of the target nucleus where the photon interacts with a nucleon such as a proton or neutron. The photon-proton vertex is complicated and can not be calculated exactly from first principles because the proton is not a point like particle and has internal structure. In order to parameterize the structure of the proton, two Q^2 (four momentum transfer squared) dependent functions, $G_E(Q^2)$ and $G_M(Q^2)$, that contain all the information about the unpolarized, elastic photon-proton vertex were introduced and are called the electromagnetic form factors of the proton. In the non-relativistic limit, $Q^2 \ll M_p^2$, the form factors can be interpreted as the Fourier transforms of the charge and magnetization distributions of the proton. In the relativistic limit they are related to the component of the proton

This dissertation follows the style of *Physical Review D*.

transition current [2]. So form factors are very important parameters that reveal the fundamental properties of the nucleon structure.

In order to understand the electromagnetic structure of the proton we have to measure its electromagnetic form factors precisely. In the past, a large number of experiments have measured elastic electron-proton scattering cross sections to extract the electric and magnetic form factors, $G_E(Q^2)$ and $G_M(Q^2)$ by using the Rosenbluth technique [3]. The results of these measurements [4, 5] have shown that $\mu_p \frac{G_E}{G_M} \approx 1$, where μ_p is the magnetic dipole moment of the proton.

Recently, elastic electron-proton polarization transfer measurements have been performed in order to measure the ratio $\frac{G_E}{G_M}$. The recent measurements [6, 7, 8] have shown a roughly linear decrease of the value of $\mu_p \frac{G_E}{G_M}$ from unity at $Q^2 = 0.3$ to about 0.3 at $Q^2 = 5.7$ GeV^2. Currently, a large discrepancy exists between the ratio of electric to magnetic form factors of the proton extracted from the Rosenbluth and polarization transfer techniques. This discrepancy indicates either an experimental or a theoretical problem in one of the two techniques.

If the polarization transfer method gives a more accurate result then also we need reliable cross-section measurements in order to extract form factors separately from the ratio $\frac{G_E}{G_M}$. It is because we can not get the separate form factors directly from the polarization transfer method; only the ratio $\frac{G_E}{G_M}$ can be extracted. So it is very important to understand the discrepancy between these two methods of measurements of electromagnetic form factors of the proton.

Many theorists and experimentalists have worked hard to solve the form factor discrepancy. High precision Rosenbluth determination of form factors [9] reproduced the previous Rosenbluth result with better accuracy. The result of this experiment clearly rules out the possibility of experimental flaw.

Recent theoretical estimates indicate that the discrepancy is a failure of the Born approximation where only one photon exchange effects are taken into account. The addition of two photon exchange contributions to calculations of elastic electron-proton scattering might be able to explain the discrepancy [10].

The Two Photon Exchange (TPE) corrections can not be calculated exactly from first principles. There are several models to estimate these corrections but there is a large model dependence and none of the models can explain the discrepancy fully. So model independent measurement of the TPE correction is required in order to constrain the theoretical models and to solve the form factor discrepancy. This

experiment will measure the TPE contributions to the form factor measurements using precise comparison of e^+p and e^-p elastic scattering.

I.2 METHODS OF MEASUREMENT OF PROTON FORM FACTORS

The proton form factors are measured by Rosenbluth and polarization transfer methods. The results of these two methods disagree. The cause of the discrepancy is believed to be due to TPE corrections which were not included in the previous Rosenbluth data analysis. In this section I will describe these two methods of measuring form factors of the proton, the discrepancy and possible sources of discrepancy. A model independent way of measuring TPE corrections is also described in brief.

I.2.1 Rosenbluth Separation

When an electron scatters elastically from a proton it exchanges a virtual photon with the proton as shown in Fig. 1. In electron scattering experiments the coupling constant ($\alpha \approx \frac{1}{137}$) is small so one can work only at the leading order of perturbation theory.

$$e(k) + P(p) \rightarrow e(k') + P(p'), \tag{1}$$

where $k = (E, \vec{k})$ and $k' = (E', \vec{k'})$ are the four momenta of the initial and final electrons. The four momentum transfer q carried by the virtual photon is constrained by momentum conservation $q = (k - k')$. The square of the four momentum transfer is a Lorentz invariant that can be expressed in terms of the incident energy E, final energy E' and the electron scattering angle θ as

$$Q^2 = -q^2 = -(\omega^2 - \vec{q}^2) = -(k - k')^2 = 4EE' \sin^2 \frac{\theta}{2}, \tag{2}$$

where $\omega = \frac{Q^2}{2M_p}$ is the energy transferred by the virtual photon from the electron to the proton and $\vec{q}$ is the spatial component of the four momentum transfer. The mass of the electron is neglected because $E \gg m_e$. Since a large Q^2 is associated with a very short wavelength, the virtual photon, $\gamma^*(\omega, \vec{q})$, can probe the internal structure of the proton.

The leptonic vertex, $e(k) \rightarrow e(k') + \gamma^*(\omega, \vec{q})$, where an electron emits a virtual photon, is fully described by QED (Quantum ElectroDynamics) and is well understood. However the hadronic vertex $\gamma^*(w, \vec{q}) + P(p) \rightarrow P(p')$, where the virtual

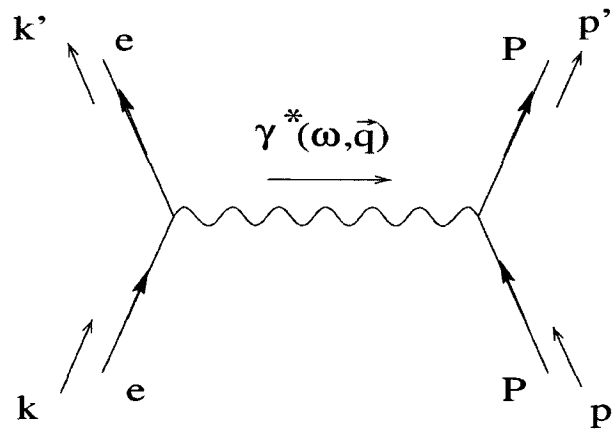

FIG. 1: Feynman diagram of elastic scattering of an electron off a proton in one photon exchange approximation (Born Approximation).

photon is absorbed by the proton, is not easy to calculate due to the structure of the proton.

To calculate the cross section of the reaction we need to calculate the amplitude of elastic scattering that depends on the leptonic and hadronic vertices. If the proton were point like, the cross section could be calculated within the framework of QED [4] which gives

$$\sigma_{\text{Mott}} = \frac{d\sigma_{\text{Mott}}}{d\Omega} = \frac{E'}{E}\frac{\alpha^2 \cos^4\frac{\theta}{2}}{4E^2 \sin^4\frac{\theta}{2}}, \tag{3}$$

where α is the fine structure constant. But the proton is not a point like particle. The spatial extent of the electromagnetic charge and current densities of the proton introduces the form factors in the cross section measurement. In this case we can express the cross section [3, 4, 11] as

$$\frac{d\sigma}{d\Omega} = \sigma_{\text{Mott}}\{F_1(Q^2) + \frac{\kappa_p^2 Q^2}{4M_p^2}F_2(Q^2) + \frac{Q^2}{2M_p^2}[F_1(Q^2) + \kappa_p F_2(Q^2)\tan^2(\frac{\theta}{2})\}, \tag{4}$$

where κ_p=1.79 is the proton's anomalous magnetic moment. $F_1(Q^2)$ and $F_2(Q^2)$ are the Dirac and Pauli form factors respectively. These form factors depend only on Q^2 and contain the information about the internal structure of the proton.

We can simplify the above expression using the Sachs form factors [5] $G_E(Q^2)$ and $G_M(Q^2)$. Sachs form factors can be expressed as a linear combination of the Dirac and Pauli form factors as

$$G_E(Q^2) = F_1(Q^2) - \kappa_p \frac{Q^2}{2M_p^2}F_2(Q^2), \tag{5}$$

$$G_M(Q^2) = F_1(Q^2) + \kappa_p F_2(Q^2). \tag{6}$$

At $Q^2 = 0$, $G_E(0) = 1$ and $G_M(0) = \mu_p = 1 + \kappa_p$ where μ_p is the proton magnetic moment. So we can rewrite the expression for the cross section as

$$\frac{d\sigma}{d\Omega} = \sigma_{\text{Mott}} \left(\frac{G_E^2(Q^2) + \tau G_M^2(Q^2)}{1+\tau} + 2\tau G_M^2(Q^2) \tan^2(\frac{\theta}{2}) \right), \tag{7}$$

where $\tau = \frac{Q^2}{4M_p^2}$. This expression for the cross section is known as the Rosenbluth formula in the one photon exchange approximation (Born Approximation). Both $G_E(Q^2)$ and $G_M(Q^2)$ depend only on Q^2.

In order to separate the form factors we can define the reduced cross section as

$$\sigma_R = \frac{d\sigma}{d\Omega} \frac{(1+\tau)\varepsilon}{\sigma_{\text{Mott}}} = \tau G_M^2(Q^2) + \varepsilon G_E^2(Q^2), \tag{8}$$

where $\varepsilon = \{1 + 2(1+\tau)\tan^2(\frac{\theta}{2})\}^{-1}$ is a measure of the longitudinal polarization of the virtual photon. For a fixed value of Q^2 it depends only on the electron scattering angle θ.

So at fixed Q^2, i.e at fixed $\tau = \frac{Q^2}{4M_p^2}$, the form factors are constant and the reduced cross section depends only on ε. We can measure the scattering cross sections at fixed Q^2 at different beam energies by varying the scattering angle. This changes the virtual photon polarization (ε).

Since the reduced cross section is linear in ε for fixed Q^2, the form factors can be extracted from a linear fit to the reduced cross section measurements made at constant Q^2 but different ε values. The extraction of form factors using the Rosenbluth separation method is shown in Fig. 2.

$G_E^2(Q^2)$ equals the slope of the reduced cross section versus ε, and $\tau G_M^2(Q^2)$ equals the intercept. Since $\tau \propto Q^2$ the reduced cross section is dominated by $G_M(Q^2)$ at all ε values for high Q^2 and the $G_M(Q^2)$ term contributes more than 90% to the reduced cross section for $Q^2 > 4$ GeV^2. This makes the precision measurement of G_E more difficult. The uncertainties in $G_M(Q^2)$ are 1–2% except at very low Q^2 but for $G_E^2(Q^2)$ they are about 5–10% for Q^2 in the range 2–4 GeV^2 and grow rapidly at higher Q^2 [13].

The world data for $G_E(Q^2)$ and $G_M(Q^2)$ extracted using Rosenbluth separations is shown in Fig. 3. The data show that the electric and magnetic charge distributions of the proton have the same spatial dependence because $G_E(Q^2)$ and $G_M(Q^2)$ are both approximately 1.0.

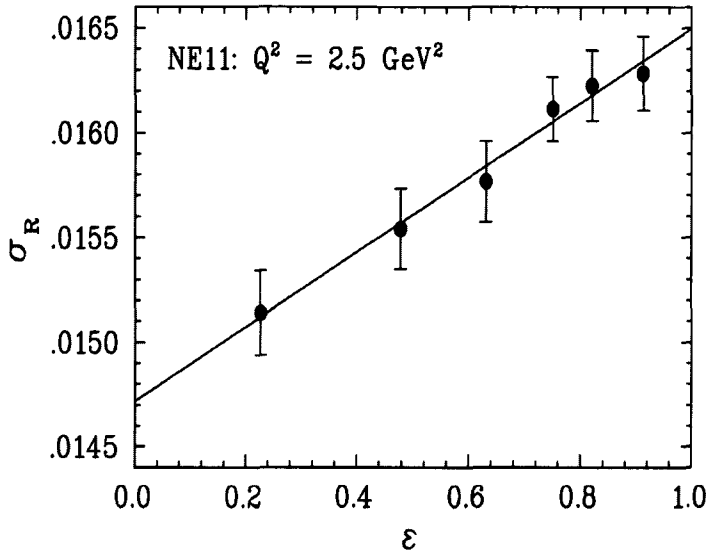

FIG. 2: The reduced cross section versus virtual photon polarization at Q^2= 2.5 GeV^2. The line shows the linear fit used to extract $G_E^2(Q^2)$ and $G_M^2(Q^2)$ [12].

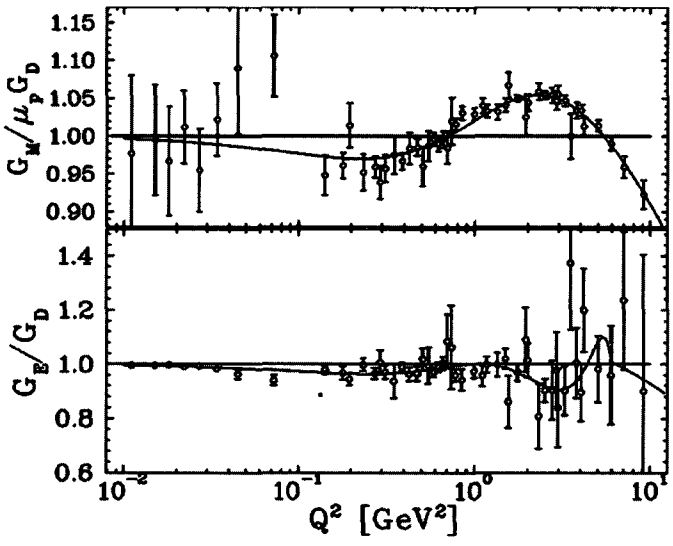

FIG. 3: G_M (top) and G_E (bottom) from Rosenbluth separation [14]. G_D is the dipole form factor. The solid lines are the global fit to all the existing data [14].

Recently, a new category of Rosenbluth data has become available where the recoiling proton is detected [9]. The new data which are shown in black filled circles in Fig. 3 appear to confirm the older data with better systematic uncertainties compared to the experiment where the scattered electron was detected. The two photon exchange contributions are the same whatever particle is detected but the cross-section and momentum variation with beam energy and scattering angle is very small compared to the previous Rosenbluth measurement. This makes the momentum dependent correction to G_E small.

The new Rosenbluth separation result [9] verified the previous Rosenbluth result and also ruled out the possibility that the discrepancy is due to experimental flaws in the Rosenbluth separation method. Reanalysis of the existing data [11] has also confirmed that the data from previous Rosenbluth separations methods are consistent with each other.

I.2.2 Polarization Transfer Technique

In the Rosenbluth separation technique, as Q^2 increases the extraction of $G_E(Q^2)$ becomes more difficult. People have measured this small term, $G_E(Q^2)$, in the presence of a large $G_M(Q^2)$ term using spin degrees of freedom [7, 8]. The ratio $\frac{G_E(Q^2)}{G_M(Q^2)}$ can be determined in polarization transfer experiments where longitudinally polarized electrons are scattered from unpolarized protons and the struck proton's polarization is measured.

In the one photon exchange approximation, the scattering of longitudinally polarized electrons results in a transfer of polarization to the recoil proton with only two non-zero components, P_t perpendicular to, and P_l parallel to the proton momentum in the scattering plane. The normal component P_n is zero in elastic scattering in the one photon exchange approximation. These two nonzero components can be expressed as [7, 8]

$$\sigma_{red} P_t = -2\sqrt{\tau(1+\tau)} G_E G_M \tan\frac{\theta}{2}, \tag{9}$$

$$\sigma_{red} P_l = \frac{E+E'}{M_p}\sqrt{\tau(1+\tau)} G_M^2 \tan^2\frac{\theta}{2}, \tag{10}$$

where σ_{red} is defined slightly differently as

$$\sigma_{red} = G_E^2 + \frac{\tau}{\varepsilon} G_M^2. \tag{11}$$

The ratio $\frac{G_E}{G_M}$ can be obtained from a simultaneous measurement of the two recoil polarization components P_l and P_t.

$$\frac{G_E}{G_M} = -\frac{P_l}{P_t}\frac{(E+E')}{2M_p}\tan\frac{\theta}{2}. \tag{12}$$

In this method the ratio of form factors is extracted directly without any cross-section measurements.

The data for $\mu_p\frac{G_E(Q^2)}{G_M(Q^2)}$ extracted using polarization transfer with statistical uncertainties is shown in Fig. 4. The data agree with the Rosenbluth results for $Q^2 < 1.0$ GeV^2. For the region where $Q^2 > 1.0$ GeV^2 the ratio decreases with increasing Q^2.

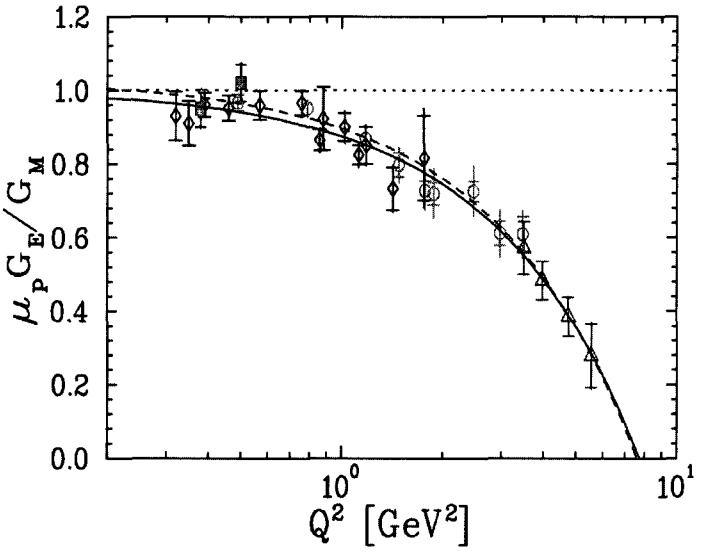

FIG. 4: The data for the proton form factor ratio $\mu_p\frac{G_E}{G_M}$ extracted using polarization transfer. Solid squares from MIT Bates and hollow diamonds, circles and triangles from Jlab measurements [7, 8]. The solid line is a fit to data from Ref. [7, 8] and dashed line is a combined fit, including the systematic uncertainties [11].

I.3 DISCREPANCY OBSERVED BETWEEN THE TWO METHODS OF MEASUREMENT

The electromagnetic form factors of the proton have been measured using two methods, Rosenbluth separation and polarization transfer. The ratio of form factors measured by the Rosenbluth technique ($\mu_p\frac{G_E}{G_M} \approx 1$) is almost constant with Q^2. But the ratio measured by polarization transfer shows a linear decrease of $R = \frac{G_E}{G_M}$ over

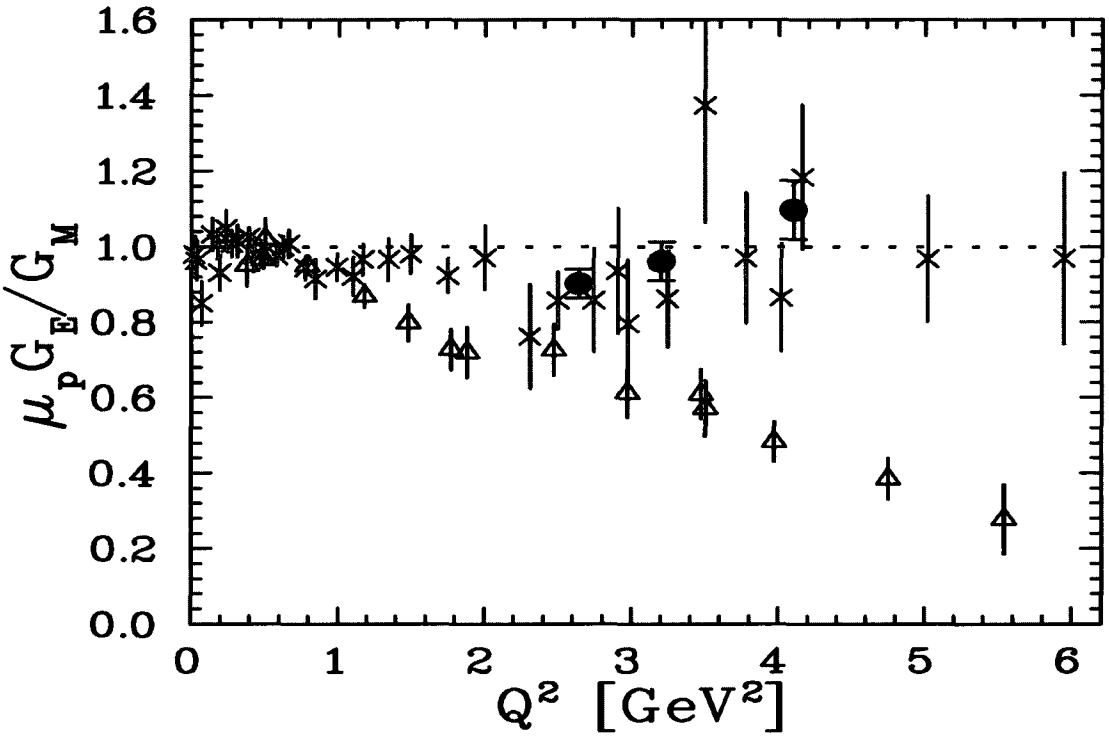

FIG. 5: The value of $\mu_p \frac{G_E}{G_M}$ that is measured by the Rosenbluth separation and the Polarization transfer technique vs. Q^2, for selected measurements [9]. The cross marks show the results of the Rosenbluth measurement. The triangles show the results of the polarization transfer measurement. The filled circles are from the super-Rosenbluth measurement [12].

the same range in Q^2 as shown in Fig. 5. The ratios of form factors measured using the two techniques differ by at least a factor of three at high Q^2.

This discrepancy on the form factors measurement raises questions about our use of elastic scattering experiments as a precise tool to determine the structure of the nucleon. Our understanding of the structure of proton depends upon the electron scattering experiments that are interpreted in terms of the single photon exchange approximation. Therefore it is essential to solve the form factor discrepancy.

I.4 POSSIBLE SOURCE OF DISCREPANCY

A possible source of the discrepancy may be due to higher order corrections to the cross-section measurement. In the Rosenbluth and polarization transfer techniques only one photon exchange effects were taken into account, because the electromagnetic coupling constant α is very small. So two or multi photon exchange effects should be of order α smaller than the leading order term. Currently, it is believed that TPE is the leading candidate to explain the existing discrepancy [10, 15, 16].

I.4.1 Radiative Corrections

The Rosenbluth formula for elastic electron-proton scattering assumes the one photon exchange approximation. The total cross-section depends on the higher order radiative processes as well so one has to include all these terms in the cross section calculation. The higher order radiative corrections are taken into account while analyzing the data. These terms include the electron vertex, electron and proton bremsstrahlung, vacuum polarization, the proton vertex and two photon exchange corrections as shown in Fig. 6. Most of the terms that do not depend on proton structure are already taken into account in the standard experimental radiative corrections and are directly implemented in the data analysis. But the terms that do depend on proton structure such as the finite proton vertex and TPE corrections are generally neglected. Due to the discrepancy in the measurement of form factors, recently there has been a growing interest in these diagrams.

The radiative correction terms such as the electron vertex correction (a), electron bremsstrahlung (c,d) and vacuum polarization (b) can be calculated using QED [17]. The radiative correction terms such as the proton vertex correction (g), two photon exchange (e, f), and proton bremsstrahlung (h) involve the proton which is not a

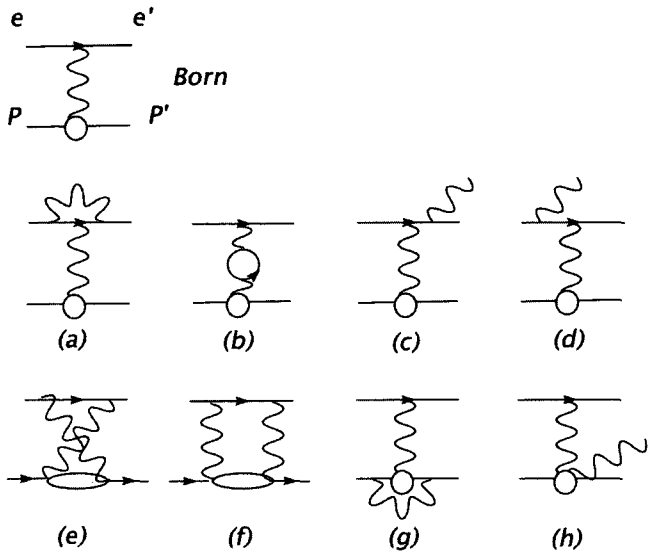

FIG. 6: Feynman diagrams for the elastic electron-proton scattering, with 1st-order QED radiative corrections. Diagrams (e) and (f) show the two photon exchange terms, where the ellipse represents a sum over all possible intermediate states.

point like particle and has various intermediate states. As a result, calculation of these terms requires inclusion of all the possible excited states of the proton such as nuclear resonances because they all contribute to the cross-section. This kind of calculation depends largely on models of nucleon structure. Of these terms, the proton vertex correction is small for high Q^2 and is ε independent at fixed Q^2. Proton bremsstrahlung is well understood by the low energy theorem and is very small at these Q^2 [17]. The least understood term which was not fully included in the earlier radiative corrections [18, 19] is the two photon exchange term. Since it is not possible to calculate the TPE correction in a model independent way, it is very important to measure the TPE contribution precisely in order to constrain models of TPE as well as to extract the correct electromagnetic form factors of the proton.

I.4.2 Two Photon Exchange (TPE)

In the Rosenbluth separation, G_E is extracted from the ε dependence of the elastic electron-proton scattering cross-section. The contribution of G_E to the cross section is small compared to G_M for large 4-momentum transfers, $Q^2 > 1$ GeV^2. Addition of the two photon exchange effect gives an additional ε-dependent term in the cross

section [10]. So what we measure in the Rosenbluth separation is not only G_E but G_E plus some additional ε dependent term as shown in Fig. 7. Based on the existing difference between the Rosenbluth and polarization transfer measurement of G_E, a (5–8%) ε dependent TPE correction to the cross section is required to explain the discrepancy [10, 17].

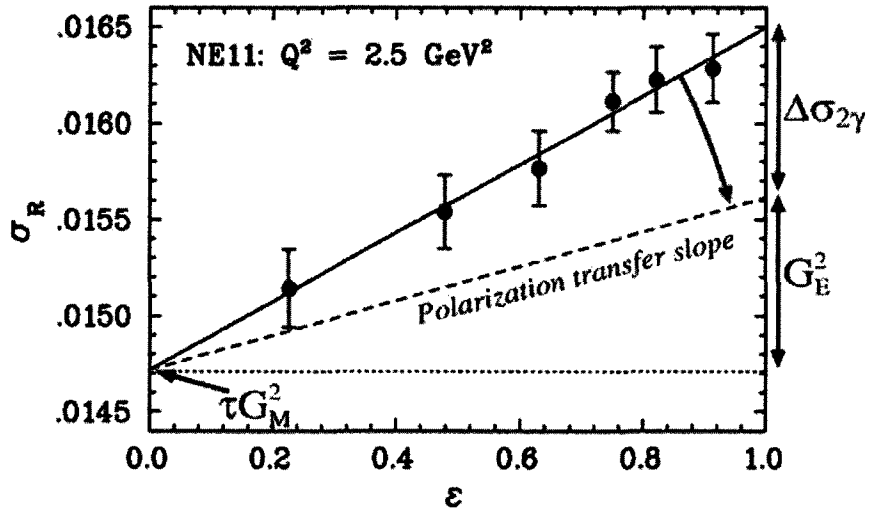

FIG. 7: Plot of σ_R versus ε. Rosenbluth data (solid circles) from the SLAC NE11 experiment. Solid line is a linear fit to the data. The dashed line shows the slope predicted by polarization transfer. The difference between these two slopes may be due to the TPE effect.

I.4.3 Model Independent Way of Measuring TPE

Most of the radiative correction terms (a, b, c and d) shown in Fig. 6 are identical for electron and positron proton scattering because they are independent of the charges of the incident particles. The only term that depends on the charges of the incident particles is the interference term between electron or positron bremsstrahlung and proton bremsstrahlung. So the comparison of electron-proton and positron-proton elastic scattering cross-section is a very clean way of measuring the effect of TPE terms that were not well understood theoretically. The effect of all the radiative

corrections that are similar for the electron and the positron cancel in the ratio so what is left in the ratio comes only from the TPE or higher order processes. The amplitude of elastic electron-proton (or positron-proton) scattering up to order α_{em}^2 can be written as [17]

$$A_{ep\to ep} = e_e e_p A_{Born} + e_e^2 e_p A_{e.br.} + e_e e_p^2 A_{p.br.} + (e_e e_p)^2 A_{2\gamma}, \tag{13}$$

where e_e and e_p are the electron (or positron) and proton charges respectively. A_{Born}, $A_{e.br.}$, $A_{p.br.}$ and $A_{2\gamma}$ describe the Born, electron bremsstrahlung, proton bremsstrahlung and TPE amplitudes respectively. Only the terms that contribute to the charge asymmetry were included in Eq. (13). Squaring the amplitude in Eq. (13), keeping only the corrections up to order α_{em} with only odd powers of the electron charge, we get

$$|A_{ep\to ep}|^2 = (e_e e_p)^2[|A_{Born}|^2 + e_e e_p A_{Born} 2\mathcal{R}e(A_{2\gamma}^*) + e_e e_p 2\mathcal{R}e(A_{e.br.} A_{p.br.}^*)], \tag{14}$$

where $\mathcal{R}e$ represent the real part of the amplitude.

Using Eq. (13) for electron and for positron scattering off a proton, the charge asymmetry in the ratio of positron-proton to electron-proton elastic scattering cross section can be expressed as

$$R^{e^+e^-} \equiv \frac{d\sigma^{(e^+)}}{d\sigma^{(e^-)}} \approx \frac{|A_{Born}^{(e^+)}|^2 + 2\mathcal{R}e\{A_{Born}^{(e^+)\dagger} A_{2\gamma(e^+)}\}}{|A_{Born}^{(e^-)}|^2 + 2\mathcal{R}e\{A_{Born}^{(e^-)\dagger} A_{2\gamma(e^-)}\}}, \tag{15}$$

where the Born amplitude A_{Born} changes sign under the interchange $e^- \leftrightarrow e^+$ but the two photon exchange amplitude $A_{2\gamma}$ does not. The interference of the A_{Born} and $A_{2\gamma}$ amplitudes therefore has the opposite sign for electron and positron scattering. Therefore the TPE radiative corrections can be written as

$$\sigma(e^\pm) = \sigma_{Born}(1 \mp \delta_{2\gamma}), \tag{16}$$

where $\delta_{2\gamma}$ is the TPE correction. This gives a charge asymmetry of:

$$R^{e^+e^-} \equiv \frac{d\sigma^{(e^+)}}{d\sigma^{(e^-)}} = 1 - 2\delta_{2\gamma}, \tag{17}$$

which is a direct and model independent measure of the TPE effect for elastic electron positron scattering.

The existing e^+/e^- cross section ratio data have been reexamined [13] to see if they are compatible with TPE effects of the size necessary to account for the Rosenbluth and polarization transfer discrepancy. The data show a small ε-dependent

correction to the positron to electron elastic scattering cross section ratio. But these data are not adequate. They are at Q^2 or large ε (see section II.2 for a detailed description of the existing world data). Better data are needed over much large range in ε and Q^2 in order to extract two photon exchange corrections directly.

In our experiment [17] we will extend these e^+/e^- cross section ratio measurements to low ε and $0.5 < Q^2 < 2.0$ GeV^2 values with high statistical precision in order to determine the TPE effect.

CHAPTER II

THEORY MODELS AND EXISTING DATA

II.1 OVERVIEW

Beyond the Born approximation, when two or more photons are exchanged, calculating the amplitude of the scattering process becomes very complicated because one needs to include of all the excited states of the proton. As a result of this there are several incomplete models to calculate multi-photon processes.

Guichon and Vanderhaeghen [10] extracted the magnitude of the TPE correction term by fitting the discrepancy between the Rosenbluth and polarization transfer data, using the full Two Photon Exchange (TPE) cross section.

Blunden et al. [15] calculated the TPE amplitude using the elastic nucleon intermediate state. They found the TPE correction of the proper sign and magnitude to partially resolve the discrepancy. They later included contribution of the $\Delta(1232)$ [20] in the intermediate state. The addition of the $\Delta(1232)$ partially cancelled the effects from the elastic intermediate state. Recently they extended their work [21] by including other higher resonances in the intermediate state. They found the additional corrections to be small but the addition of their total corrections to the Rosenbluth data gave a better agreement with the polarization transfer result.

Chen et al. [22] calculated the hard TPE elastic electron-proton scattering amplitude at large momentum transfer by relating the scattering process on the nucleon to Generalized Parton Distributions (GPDs). This method claims to sum over all the possible excitations of inelastic nucleon intermediate states. They found that the TPE corrections to the Rosenbluth process can resolve the discrepancy.

A recent calculation by Kivel and Vanderhaeghen [16] found that the leading TPE amplitude behaves as $1/Q^4$ relative to the one photon exchange amplitude. They expressed the TPE amplitude in terms of leading twist nucleon distribution amplitudes (DAs) and used several models of nucleon DAs to estimate the TPE corrections.

The above models are discussed in detail in the following sections. The existing world data on measuring the TPE effect by comparing the positron-proton to electron-proton elastic scattering cross-section will be described in the last section of this chapter.

II.1.1 Phenomenological Estimates

In order to reconcile the Rosenbluth and polarization transfer measurements of form factors, Guichon and Vanderhaeghen [10] made phenomenological estimates of the TPE contribution to the one photon exchange approximation. They used the phenomenological form factors to describe the full electron-nucleon scattering amplitude. They expressed the T matrix of elastic ep scattering as

$$T = \frac{e^2}{Q^2}\bar{u}(k')\gamma_\mu u(k) \times \bar{u}(p')\left(\tilde{G}_M\gamma^\mu - \tilde{F}_2\frac{P^\mu}{M} + \tilde{F}_3\frac{\gamma\cdot K P^\mu}{M^2}\right)u(p), \tag{18}$$

where $\tilde{G}_M$, $\tilde{F}_2$ and $\tilde{F}_3$ are complex functions of ε and Q^2. In the Born approximation these are functions of Q^2 only and $\tilde{G}_M$=G_M, $\tilde{F}_2$=F_2 and $\tilde{F}_3$=0. Using this technique they calculated approximate expressions for the cross-section and polarization transfer as

$$\frac{d\sigma}{C_B(\varepsilon,Q^2)} \simeq \frac{|\tilde{G_M}|^2}{\tau}\left\{\tau + \varepsilon\frac{|\tilde{G_E}|^2}{|\tilde{G_M}|^2} + 2\varepsilon(\tau + \frac{|\tilde{G_E}|}{|\tilde{G_M}|})\mathcal{R}e\left(\frac{\nu\tilde{F}_3}{M^2|\tilde{G_M}|}\right)\right\}, \tag{19}$$

where $C_B(\varepsilon,Q^2)$ is a phase space factor.

$$\frac{P_t}{P_l} = -\sqrt{\frac{2\varepsilon}{\tau(1+\varepsilon)}}\left\{\frac{|\tilde{G_E}|}{|\tilde{G_M}|} + (1 - \frac{2\varepsilon}{1+\varepsilon}\frac{|\tilde{G_E}|}{|\tilde{G_M}|})\mathcal{R}e\left(\frac{\nu\tilde{F}_3}{M^2|\tilde{G_M}|}\right)\right\}, \tag{20}$$

where $\tilde{G}_E = \tilde{G}_M - (1+\tau)\tilde{F}_2$ and $\mathcal{R}e$ represents the real part. In order to separate the Born and higher order corrections, the generalized form factors were split into Born and TPE correction terms as $\tilde{G}_E = G_E + \delta G_E$, $\tilde{G}_M = G_M + \delta G_M$ and $\tilde{F}_3 = \tilde{F}_3$.

They simplified the above two equations by assuming that the Rosenbluth slope is linear in ε and the generalized amplitudes are independent of ε (these assumptions are consistent with the ε dependence of the cross-section data of Andivahis et al. [5]).

Finally they were able to show that what is measured using the Rosenbluth method is

$$(R^{exp}_{Rosenbluth})^2 = \frac{|\tilde{G_E}|^2}{|\tilde{G_M}|^2} + 2\left(\tau + \frac{|\tilde{G_E}|}{|\tilde{G_M}|}\right)Y_{2\gamma}, \tag{21}$$

where $\frac{|\tilde{G_E}|}{|\tilde{G_M}|}$ and $Y_{2\gamma}$ are independent of ε. In the Born approximation, $(R^{exp}_{Rosenbluth})^2 = (\frac{G_E}{G_M})^2$. According to their calculation, the polarization transfer ratio is

$$(R^{exp}_{polarization}) = \frac{|\tilde{G_E}|}{|\tilde{G_M}|} + (1 - \frac{2\varepsilon}{1+\varepsilon}\frac{|\tilde{G_E}|}{|\tilde{G_M}|})Y_{2\gamma}, \tag{22}$$

rather than $(R^{exp}_{polarization}) = \frac{G_E}{G_M}$. The dimensionless ratio

$$Y_{2\gamma}(\nu, Q^2) = Re\left(\frac{\nu \tilde{F}_3}{M^2 |\tilde{G_M}|}\right), \tag{23}$$

contains the effect of the TPE term ($\tilde{F}_3$). They solved the Eqs. (21) and (22) numerically by fitting the data with polynomial function in Q^2 and extracted $Y_{2\gamma}$, which measures the relative size of the TPE amplitude $\tilde{F}_3$.

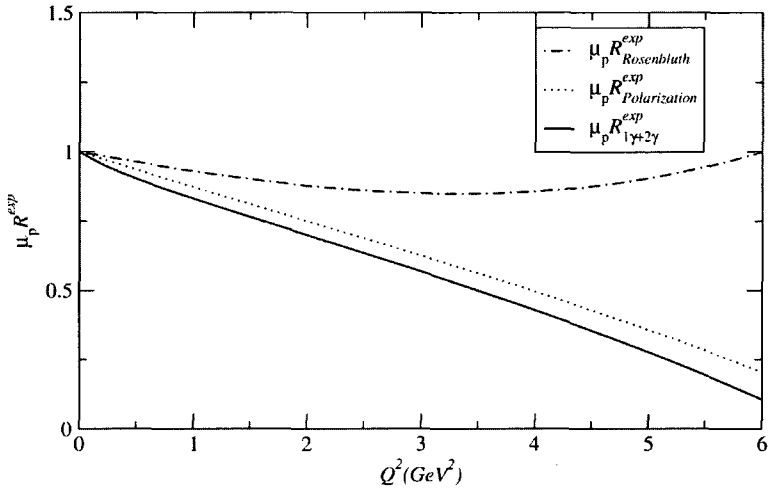

FIG. 8: Rosenbluth and polarization transfer ratio compared with the TPE corrected ratio extracted using phenomenological estimates [10]. The dotted dash and dotted lines show the polynomial fits to the Rosenbluth [5] and polarization transfer [7, 8] data. The solid line shows the TPE corrected ratio $\mu_p \tilde{G_E}/\tilde{G_M}$ extracted by fitting the discrepancy between the Rosenbluth and polarization transfer.

They found that $Y_{2\gamma}$ is small and introduces no noticeable ε dependence in the polarization transfer result. They used this to extract a corrected $\mu_p G_E/G_M$ from the Rosenbluth and polarization transfer data (see Fig. 8). Even though $Y_{2\gamma}$ is only a few percent, this correction resolves the discrepancy. From Fig. 8 we can see that their corrected data is in good agreement with the polarization transfer result. On the basis of this fit to the data they concluded that the TPE effect should be up to 6–10% on the positron to electron scattering cross section ratio in the Q^2 range 2–6 GeV^2.

II.1.2 Simple Hadronic Model

Blunden et al. [15] calculated the 2γ exchange contribution to the electron-proton elastic scattering cross section using a simple hadronic model. They only considered

the elastic proton intermediate states while evaluating the TPE amplitude.

They wrote the amplitude for the one-loop virtual corrections $\mathcal{M}_1$ as the sum of a factorizable term which is proportional to the Born amplitude $\mathcal{M}_0$ and a non-factorizable part $\bar{\mathcal{M}}_1$.

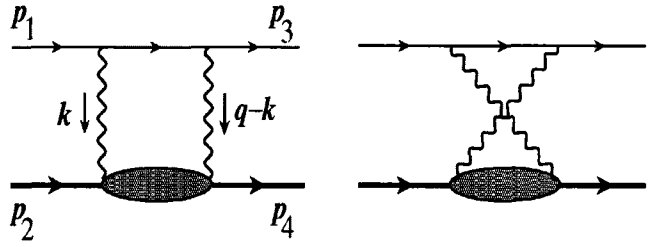

FIG. 9: Two photon exchange box and crossed box diagrams. The blob represents the excited states of the proton.

$$\mathcal{M}_1 = f(Q^2, \epsilon)\mathcal{M}_0 + \bar{\mathcal{M}}_1, \tag{24}$$

where the factorizable term parameterized by $f(Q^2, \varepsilon)$ contains all the terms that are independent of the proton structure. The ratio of the full to Born cross sections gives,

$$1 + \delta = \frac{|\mathcal{M}_0 + \mathcal{M}_1|^2}{|\mathcal{M}_0|^2}, \tag{25}$$

where

$$\delta = 2f(Q^2, \epsilon) + 2\frac{Re\{\mathcal{M}_0^\dagger \bar{\mathcal{M}}_1\}}{|\mathcal{M}_0|^2}. \tag{26}$$

From the radiative correction term δ most of them are already taken into account in the standard radiative correction and they do not depend on proton structure. The terms that depend on proton structure such the two photon exchange are included in $\bar{\mathcal{M}}_1$. The finite proton vertex correction was found to be not strongly dependent on ε and was less than 0.5% for $Q^2 < 6$ GeV^2 [15]. Therefore the only radiative correction which has significant epsilon dependence is the 2γ exchange diagrams shown in Fig. 9. It is denoted by $\mathcal{M}^{2\gamma}$

$$\delta^{2\gamma} \to 2\frac{Re\{\mathcal{M}_0^\dagger \mathcal{M}^{2\gamma}\}}{|\mathcal{M}_0|^2}, \tag{27}$$

where $\mathcal{M}^{2\gamma}$ includes all possible proton intermediate states in Fig. 9.

They first considered only the elastic contribution to the full response function and assumed that the proton propagates as a Dirac particle. They use the phenomenological form factors at the γp vertices. The 2γ exchange amplitude representing Fig. 9 can be written as

$$\mathcal{M}^{2\gamma} = e^4 \int \frac{d^4k}{(2\pi)^4} \frac{N_{box}(k)}{D_{box}(k)} + e^4 \int \frac{d^4k}{(2\pi)^4} \frac{N_{x-box}(k)}{D_{x-box}(k)}, \tag{28}$$

where numerators N_{box} and N_{x-box} are the matrix elements and the denominators D_{box} and D_{x-box} are the products of propagators [15].

They calculated the total infrared (IR) divergent TPE contribution to the cross-section as

$$\delta_{IR} = -\frac{2\alpha}{\pi} \ln(\frac{E_1}{E_3}) \ln(\frac{Q^2}{\lambda^2}), \tag{29}$$

where E_1 and E_3 are the initial and final electron energies respectively and λ is the infinitesimal photon mass required to regulate the IR divergences in the photon propagator. The IR divergence appears when one of the virtual photons carries almost zero four momentum transfer and the other carries almost the entire four momentum transfer.

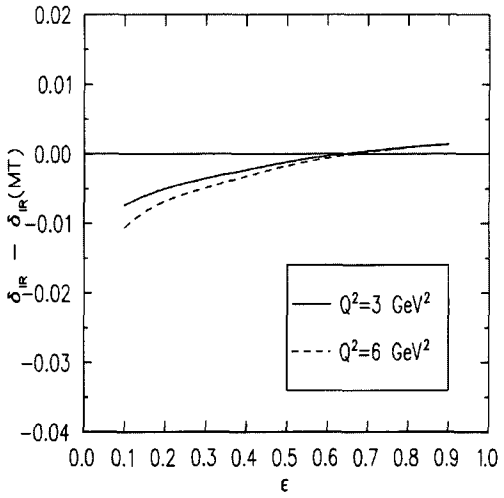

FIG. 10: Difference between the model independent IR divergent part of the TPE correction calculated by Blunden et al. [15] and that calculated by Mo and Tsai [18].

The difference between the total and the standard Mo and Tsai IR divergent TPE corrections [18] is shown in Fig. 10. The difference is plotted against ε for $Q^2 = 3$ GeV^2 and $Q^2 = 6$ GeV^2. This shows that the different treatments of the IR divergent term can lead to about a 1% change in the cross section over the range

of ε. This effect alone gives a reduction of the order of 3% and 7% in the ratio $R = \mu_p \frac{G_E(Q^2)}{G_M(Q^2)}$ for $Q^2 = 3$ GeV^2 and $Q^2 = 6$ GeV^2 respectively [15].

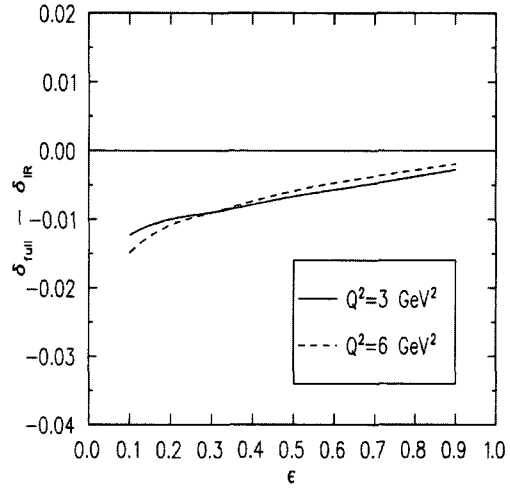

FIG. 11: Difference between the full TPE correction and the model independent IR divergent part of the TPE correction calculated by Blunden et al. [15].

They also compare the ε dependence of the full calculation (δ_{full}) with δ_{IR} by calculating the difference $\delta_{full} - \delta_{IR}$. The difference between the full calculation of the TPE diagrams and the model independent IR divergent result is shown in Fig. 11. The IR contribution is the same in both the results so the IR divergence cancels in the difference and hence we get the contribution of the finite part from the difference. So the finite term in the TPE amplitude also shows the significant ε dependence that increases with Q^2 slightly. The correction is largest at backward angles and small at forward angles.

They calculated the effect on the ratio R in the Rosenbluth separation assuming that the modified cross-section is approximately linear in ϵ and has the form

$$d\sigma = (aA)\tau G_M(Q^2)[a + (B\tilde{R}^2 + b)\epsilon], \tag{30}$$

where $B = \frac{1}{\mu_p^2 \tau}$ and $\tilde{R}$ is the corrected ratio R, a and b are the parameters of the linear fit function and A is a constant.

$$\tilde{R} = R^2 - \frac{b}{B}. \tag{31}$$

This shift in $R = \mu_p \frac{G_E(Q^2)}{G_M(Q^2)}$ due to the extra TPE correction is shown in Fig. 12. They showed that the addition of the TPE correction to the Rosenbluth measurement

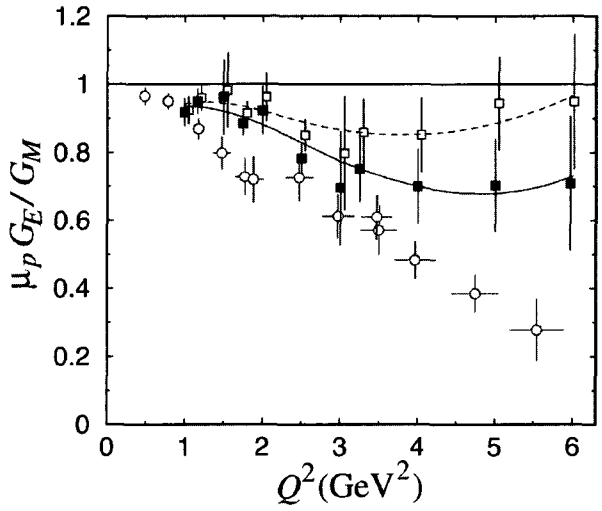

FIG. 12: The ratio of form factors using Rosenbluth separation (hollow squares), polarization transfer (hollow circles) and corrected Rosenbluth result due to two photon exchange corrections (filled squares) by Blunden et al.. Error bars in the two photon exchange corrected results are kept unchanged [15].

partially resolves the form factor discrepancy.

II.1.3 Higher Nuclear Resonances

The TPE box and cross box diagrams shown in Fig. 9 contain the full spectrum of proton excited states as intermediate states. So the total TPE correction is the sum of contributions from all the proton intermediate states. So it is important to include all the resonances in the calculations to see their contributions.

In addition to the nucleon contribution [15] to the TPE correction, contribution of the Δ resonance [20] and other heavier resonances [21] were also studied. It was shown in [20] that the Δ contribution to the cross section is about -1% to $+2\%$ and was found to be largest at backward angles. They extended their work to include other heavier resonances such as the P_{33} (Δ), D_{13}, D_{33}, P_{11}, S_{11} and S_{31} in [21] (see Fig. 13). Adding the higher resonances to the TPE calculation improves the agreement with the data.

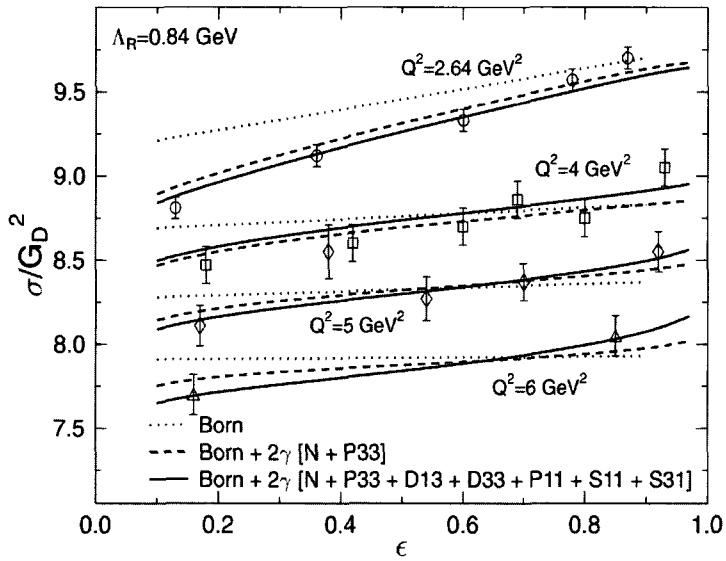

FIG. 13: Result of adding TPE corrections to the Born cross-section. The TPE corrections include the nucleon [15] and mentioned resonances [20, 21]. The dotted line shows the cross section calculated in the Born approximation using the polarization transfer form factors. The dashed line also includes Two Photon Exchange effects with a proton or Δ in the intermediate state. The solid line also includes higher resonances in the intermediate state. Note that the solid line is reasonably consistent with the measured cross sections.

II.1.4 Partonic Calculation

Afanasev et al. [23] estimated the TPE contribution to elastic electron-proton scattering at large momentum transfers ($Q^2 \gg M^2$) by considering the scattering of an electron off a parton in the proton. This is a high energy model and is not valid at $Q^2 < 1.0$ GeV^2. In this process the leptons scatter from quarks in the proton with the exchange of a virtual photon as shown in Fig. 14. They related the process in the proton to generalized parton distributions (GPDs). The generalized parton distributions give the probability of finding a quark with a certain longitudinal momentum fraction x in the proton to interact with a virtual photon and being able to reinsert that quark in the proton with momentum fraction x'. They described the lepton-quark scattering process represented by H in Fig. 14 by box and crossed box diagram as shown in Fig. 9. In this approximation both of the virtual photons interact with the same quark in the proton.

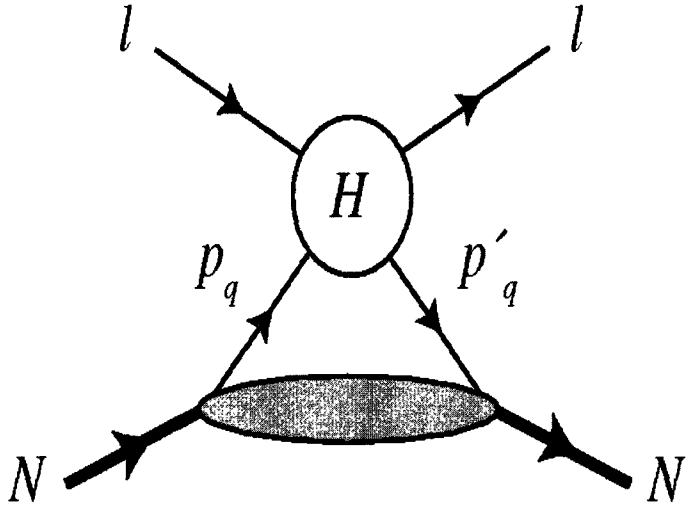

FIG. 14: Elastic lepton-nucleon scattering at large momentum transfer. H represents the partonic scattering process in which leptons scatters from quarks in the nucleon. GPD's of the nucleon is represented by the lower blob [23] .

This model shows that the Rosenbluth ratio becomes nonlinear at large ε values. The results depend on which of the two GPDs they used. Addition of TPE correction calculated by this model to the reduced cross-section assuming one photon exchange make the better agreement with the data as shown in Fig. 16. The slope of the Rosenbluth plot shows a significant ε dependence as well. This model could

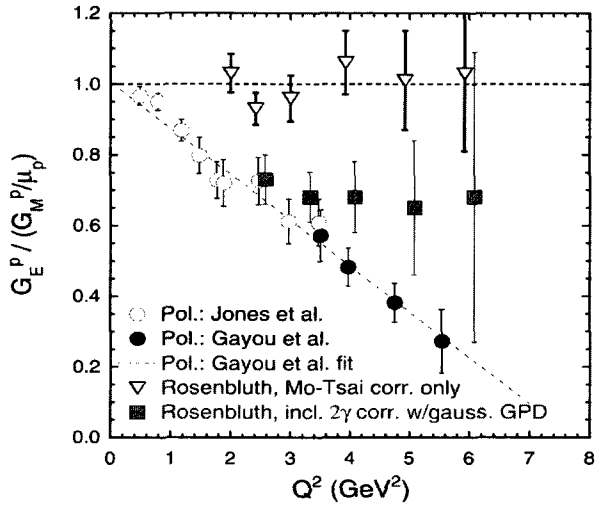

FIG. 15: Electric to magnetic form factors ratio including TPE corrections calculated using partonic model [23]. The Rosenbluth data [5] corrected with their TPE correction using Gaussian GPD is shown in filled squares.

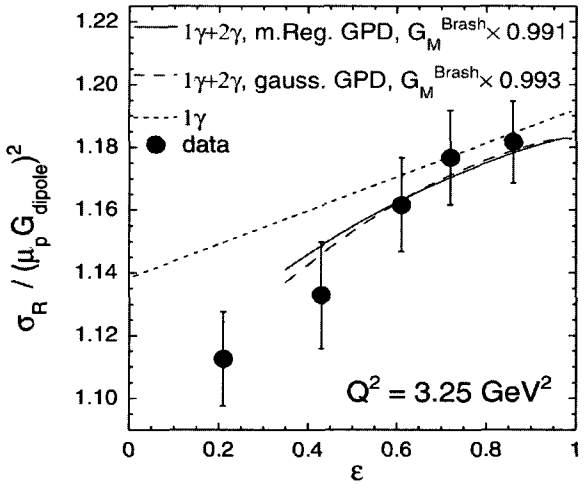

FIG. 16: Reduced cross-section σ_R divided by $(\mu_p G_{\text{dipole}})^2$ as a function of ε. Dotted line represents the Borm approximation, using G_E/E_M from polarization transfer data [7, 8]. Solid curve is the result of partonic model [23] using modified Regge GPD and the dashed curve is for Gaussian GPD for $Q^2 > M_p^2$. The data points are from [5].

resolve the discrepancy for Q^2 in the range of 2-3 GeV^2 which is shown in Fig. 15 and partially resolve the discrepancy at high Q^2. The detailed description of this calculation can be found in references [22, 23, 24]. Since this model is only valid at $Q^2 > 1.0$ GeV^2, experimental verification of the validity of this result is important.

II.1.5 QCD Factorization Approach

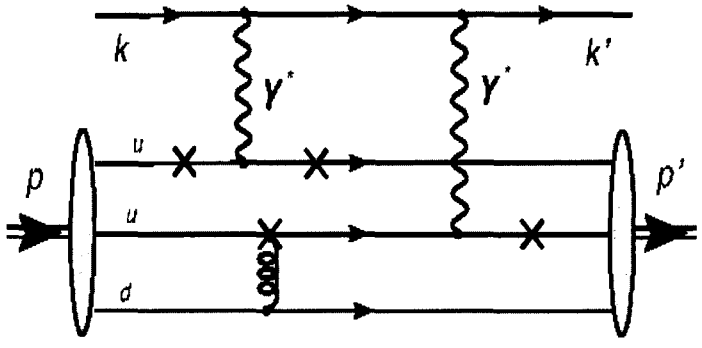

FIG. 17: Feynman diagram for elastic electron-proton scattering with two hard photon exchanges. The momentum is then shared with the third quark by gluon exchange. Cross indicates the other possibilities to attach gluon.

Kivel and Vanderhaeghen [16] used the QCD factorization approach to calculate the TPE contribution to elastic electron-proton scattering at large momentum transfer ($Q^2 \gg M^2$). They used the process as described in Fig. 17 where the electron interacts with different quarks in the proton through the exchange of two hard virtual photons. During this process gluon exchange takes place between the quarks. They computed $\delta\tilde{G}_M$ and $\tilde{F}_3$ by using a convolution integral of the proton distribution amplitudes (DAs), the functions that describe the distribution of quarks in the proton, with the hard coefficient function.

They showed that the TPE corrections due to hard two photon exchange are

$$\delta\tilde{G}_M = \frac{\alpha_{em}\alpha_s(\mu^2)}{Q^4}\left(\frac{4\pi}{3!}\right)^2(2\zeta-1)\int d[y_i]\,d[x_i]\frac{(4x_2y_2)}{D}$$
$$\times\ \{Q_u^2[(\acute{V}+\acute{A})(V+A)+4\acute{T}T](3,2,1)+Q_uQ_d[(\acute{V}+\acute{A})(V+A)+4\acute{T}T](1,2,3)$$
$$+\ Q_uQ_d^2[(\acute{V}V+\acute{A}A)](1,3,2)\}, \qquad (32)$$

$$\frac{\nu}{M^2}\tilde{F}_3 = \frac{\alpha_{em}\alpha_s(\mu^2)}{Q^4}\left(\frac{4\pi}{3!}\right)^2(2\zeta-1)\int d[y_i]\,d[x_i]\frac{(2x_2\bar{y}_2+\bar{x}_2y_2)}{D}$$
$$\times\{Q_u^2[(\acute{V}+\acute{A})(V+A)+4\acute{T}T](3,2,1)+Q_uQ_d[(\acute{V}+\acute{A})(V+A)+4\acute{T}T](1,2,3)$$
$$+Q_uQ_d^2[(\acute{V}V+\acute{A}A)](1,3,2)\}, \qquad (33)$$

where Q represents the quark charges and A, V and T are nucleon distribution amplitudes (see reference [16] for a detailed explanation). They showed that the TPE corrections to the form factors $\tilde{G}_M$ and $\nu/M^2\tilde{F}_3$ goes as $1/Q^4$ at large Q^2.

In order to evaluate the convolution integral shown in Eqs. (32) and (33) they used two models for nucleon DAs, COZ and BLW.

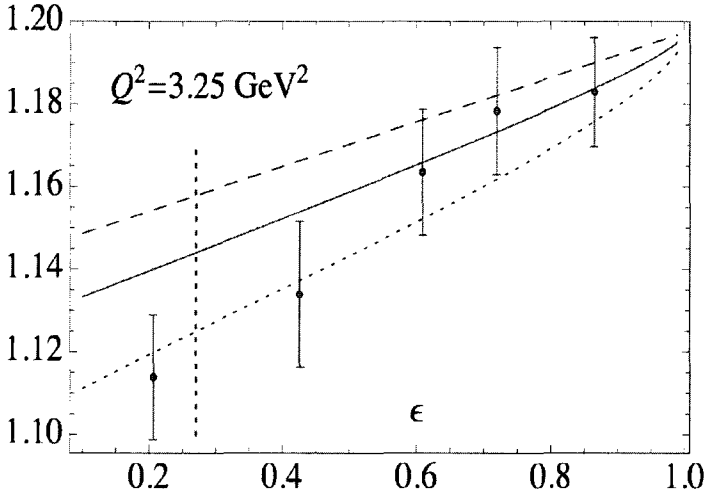

FIG. 18: The reduced cross-section σ_R (y axis) as a function of ε (x axis). Dashed curve: result of one photon exchange using G_E/E_M from polarization transfer data [6, 8]. Their calculation with BLW (COZ) model is shown in solid (dotted) line respectively. The vertical dotted line indicates the epsilon value above which their description for hard photons is valid. The data points are from [5].

The result of their calculation is shown in Fig. 18. It shows that adding the TPE correction changes the slope of the Rosenbluth data. Nonlinearity is seen only for very forward scattering angles and the TPE corrected result is in good agreement with the data. The COZ and BLW nucleon distribution amplitudes give very different results indicating the size of some of the model uncertainty in their calculation. The TPE correction due to the COZ model for nucleon DAs is twice the BLW. They predict that the e^+/e^- ratio of cross-sections deviates from unity by 2.5% (BLW) to 5% (COZ).

II.1.6 Summary of Theory Models

The calculation of the TPE contribution to elastic electron-proton scattering was done either at $Q^2 < 1.0$ GeV^2 where only nucleon intermediate states were considered or at high Q^2 where the calculations are done at the partonic level.

Although all the models have different regions of validity and quantitative differences, they all predict that the TPE effect is small at larger ε and depends weakly on Q^2. They all resolve part of the discrepancy and predict a TPE effect of the size needed to explain the existing discrepancy.

So we need very precise positron data to measure the TPE correction in a model independent way which will constrain the TPE models and give a the clear answer whether TPE is the cause of the discrepancy in the two methods of measuring the form factors of the proton.

II.2 EXISTING WORLD'S POSITRON DATA

Several experiments were performed over the last fifty years in order to investigate the importance of TPE corrections to electron-proton elastic scattering. They measured the ratio of positron-proton to electron-proton elastic scattering cross sections in order to estimate the size of the TPE effect. This section summarizes the results of the previous experiments, the experimental techniques used and the kinematic ranges covered.

II.2.1 Yount et al., 1962

This experiment [26] used the Stanford Mark III linear accelerator to produce the positron beam by passing the electron beam from the accelerator through a tantalum radiator of thickness 3.2 radiation lengths. The low energy positrons ($\approx$ 10 MeV) emerging from the radiator were accelerated to 300 MeV using the remainder of the accelerator. The beam was momentum analyzed by using a magnet system. They used a liquid hydrogen target positioned along the beamline. The scattered electrons and positrons were detected using two plastic scintillators in coincidence.

The ratio

$$R = \frac{\sigma_- - \sigma_+}{\sigma_- + \sigma_+}, \tag{34}$$

where σ_- and σ_+ are the differential scattering cross-section for electron-proton and positron-proton at identical beam energies and scattering angles was measured to

determine the TPE effect on elastic electron-proton scattering.

The two different beam energies (0.205 and 0.307 GeV) were used for both electron and positron scattering. The ratio R was measured at three different scattering angles (30°, 45° and 130°). This data is at low Q^2 ($Q^2 < 0.3$ GeV^2) and is consistent with $R = 1$, as shown in Fig. 19.

II.2.2 Browman et al., 1965

Browman et al. [27] performed two experiments using the electron and positron beams from the Stanford Mark III linear accelerator. They used a liquid hydrogen target. They used "open" counters to count the recoiling electron and proton in coincidence in the first experiment. The "open" counters consisted of a Lucite absorber followed by a proton telescope. The absorber was used to reject background. They found a large probability of recording unwanted background events for the highest momentum transfer points. They remeasured the highest momentum transfer point by detecting the electrons and positrons using a counter telescope located at the focal plane of a magnetic spectrometer. They used a Lucite absorber followed by a lead-scintillator shower counter to identify the electrons and positrons.

In this experiment, the positron-proton to electron-proton cross-section ratio $R = \frac{\sigma_+}{\sigma_-}$ was measured at several beam energies in the range 500–900 MeV at different scattering angles. This data covers a wide range in ε at low Q^2 ($Q^2 < 0.8$ GeV^2). The data from this experiment is shown in Fig. 19.

II.2.3 Anderson et al., 1967

Anderson et al. [28, 29] used the 2 GeV photon beam from the Cornell synchrotron to produce leptons (electrons and positrons) in order to measure the positron-proton to electron-proton cross-sections ratio $R = \frac{\sigma_+}{\sigma_-}$. Leptons were produced by pair production when the photon beam hit a lead radiator in the photon beamline. They used a liquid hydrogen target. They used a thin foil spark chamber and a counter telescope consisting of two scintillation counters and a lead-glass Cherenkov shower counter to detect electrons in the polar angular range from 25° to 75°. They selected the elastic events using coplanarity and elastic kinematic cuts.

They collected data in two runs at 1.2 GeV and 0.8 GeV. This data covers the Q^2 range from 0.3 to 1.0 GeV^2. Unlike the Browman et al. [27], this data does not show any Q^2 dependence of the ratio and it does not indicate any significant TPE

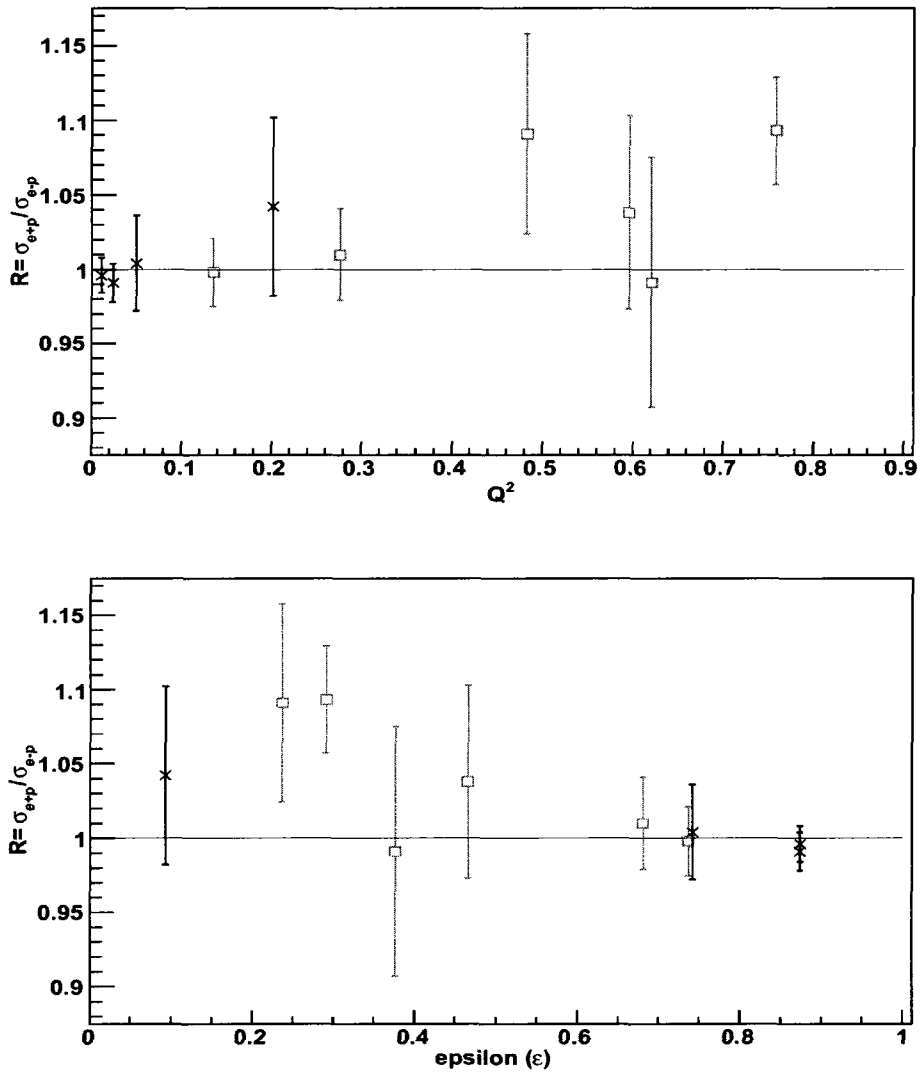

FIG. 19: Top: positron-proton to electron-proton cross-section ratio (R=$\frac{\sigma_+}{\sigma_-}$) versus Q^2: crosses are from Yount et al. [26] and hollow squares from Browman et al. [27]. Bottom: positron-proton to electron-proton cross-section ratio ($R = \frac{\sigma_+}{\sigma_-}$) versus ε. Markers are same as the left plot.

correction to the elastic electron-proton scattering measurements. The data from this experiment is shown in Fig. 20.

II.2.4 Cassiday et al., 1967

This experiment used a 1.7 GeV electron beam from the Cornell Synchrotron to produce electrons and positrons. The beam was incident on a one radiation length lead target. Electrons and positrons exiting the target were selected by using a beam transport system that momentum analyzed the particles and focused them to a 46 cm long liquid hydrogen target. The beam intensity (average electron or positron intensity) of this experiment was 2×10^6 sec^{-1} [30]. The scattering angle was measured by using thin-foil spark chamber and scintillation counters. The chambers were triggered by simultaneous observation of an electron from one side and a proton from the other. The elastic events were selected by putting cuts on polar and azimuthal angles of each event and by examining the pulse height of the electrons in the Cherenkov counters that were arranged symmetrically on opposite sides of the target.

They measured the ratio of positron-proton to electron-proton differential elastic scattering cross sections at Q^2 of 0.8 and 1.0 GeV^2. They calculated the higher order radiative correction 2δ by using the relation

$$R = \frac{\sigma_+}{\sigma_-} = 1 - 2|\delta|. \tag{35}$$

Their measured value of correction $2|\delta|$ is 0.038 with estimated error of ±0.005.

II.2.5 Bartel et al., 1967

In this measurement [31] a 6 GeV electron beam hit a 1.5 cm thick Cu-radiator placed behind the outlet window of the synchrotron vacuum chamber. Leptons leaving the converter were momentum analyzed, collimated and steered onto a long hydrogen target using a magnetic channel. They measured the ratio of cross-sections, $R = \frac{\sigma_+}{\sigma_-}$, at two points, one at $Q^2 = 0.45$ GeV^2 and scattering angle of 17.5°, and the other at $Q^2 = 1.36$ GeV^2 and scattering angle of 35°. Their ratio is consistent with unity for both the points within the error bars and does not show any TPE correction to the elastic electron-proton scattering measurements. The data from this experiment is shown in Fig. 21.

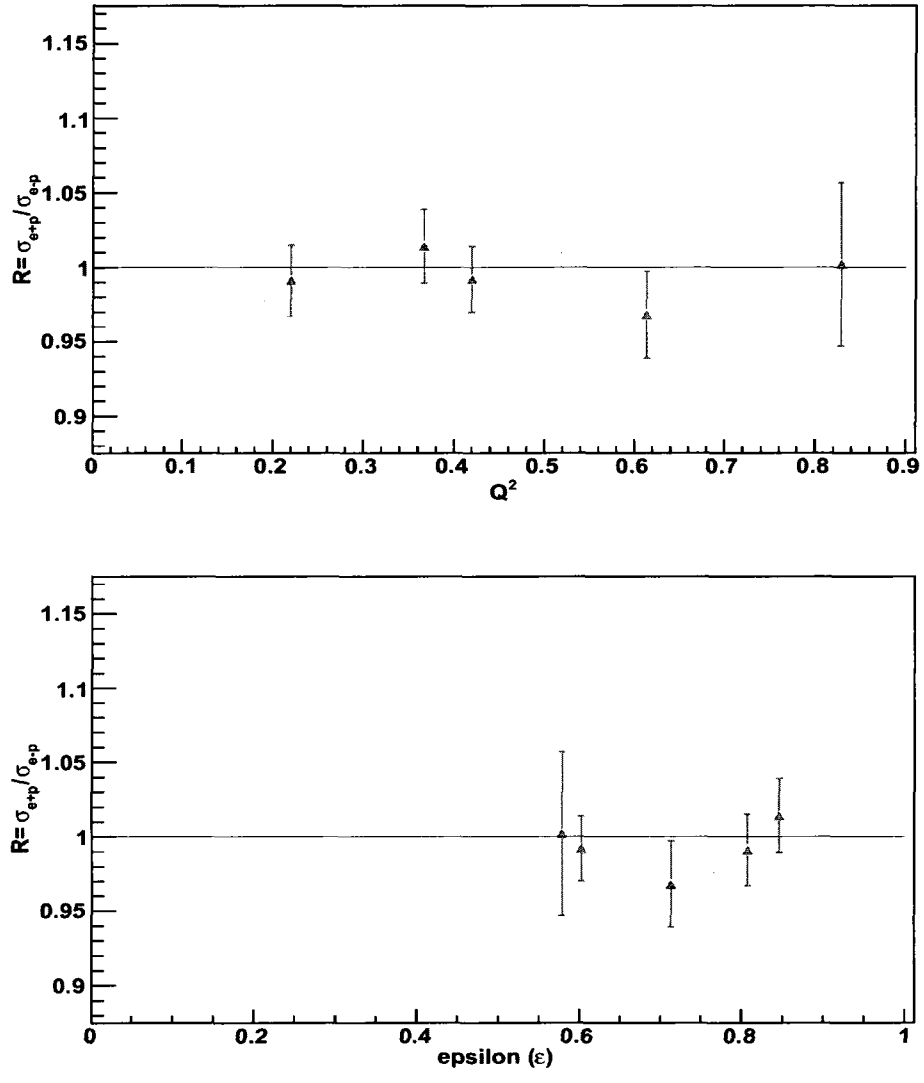

FIG. 20: Top: positron-proton to electron-proton cross-section ratio (R=$\frac{\sigma_+}{\sigma_-}$) versus Q^2: filled circle is from Anderson et al. [28] and filled triangles are from Anderson et al. [29]. Bottom: positron-proton to electron-proton cross-section ratio ($R = \frac{\sigma_+}{\sigma_-}$) versus ε. Markers are same as the left plot.

II.2.6 Bouquet et al., 1968

This experiment measured the ratio R at 180° scattering angle, unlike the other experiments which mostly measured the ratio at small electron scattering angles. They used Gourdin's model [32] to define the elastic electron-proton and positron-proton scattering and measured the ratio using this model which assumes that the accuracy of the measured value of TPE correction will be very accurate when measured at 180° scattering angles. They detected the recoil proton at 0° in coincidence with the backward electron or positron.

They used a magnetic spectrometer to detect the leptons and protons. The scattering leptons were detected using scintillator counters and the recoil proton was detected using a 9 channel ladder counter sandwiched between two scintillator counters. The elastic scattering peak is recorded on the proton ladder counter after coincidence with electron and positron counters [32]. They measured the ratio $R = \frac{\sigma_+}{\sigma_-}$ at two Q^2 points 0.3 and 1.25 GeV^2. The data from this experiment is shown in Fig. 21.

II.2.7 Mar et al., 1968

Mar et al. [33] used the electron beam from the Stanford Linear Accelerator to generate lepton beams by hitting a copper radiator. The low energy leptons so produced were accelerated to generate the required beam for the experiment. They measured the ratio R for the scattering angle range $12.5° \leq \theta \leq 35.0°$ and $2.6° \leq \theta \leq 15.0°$ with incident leptons energies of 4 GeV and 10 GeV respectively. They extended the Q^2 range to higher value than previous experiments. They made some measurements at moderate Q^2 that covers smaller angular region than previous experiment. The data from this experiment is shown in Fig. 21.

II.2.8 Summary of World's Positron Data

The data described above is plotted in Fig. 21 for the ratio of positron-proton to electron-proton elastic scattering cross-sections as a function of Q^2. It is hard to see the clear Q^2 dependence from this data due to the large uncertainty for high Q^2 data points. All the experiments done in the past had a very low luminosity. Due to this, the uncertainty is large, especially for high Q^2 where the cross-section is small.

The existing data covers a fairly large Q^2 and ε range. However, there are only

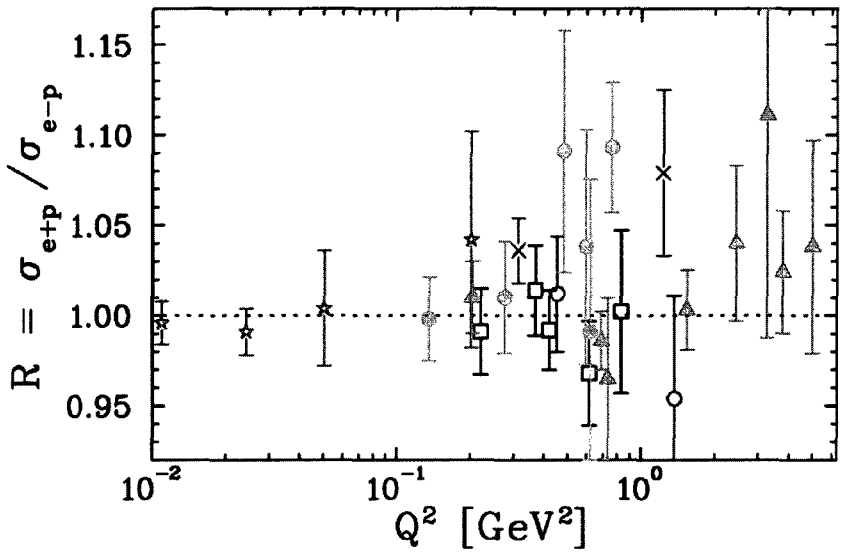

FIG. 21: World data for the positron-proton to electron-proton cross-section ratio ($R = \frac{\sigma_+}{\sigma_-}$) versus Q^2. Different symbols indicate the different experiments: solid triangles [33], stars [26], filled circles [27], diamonds [29], squares [28], crosses [32], hollow circles [31]. The plot is taken from [34].

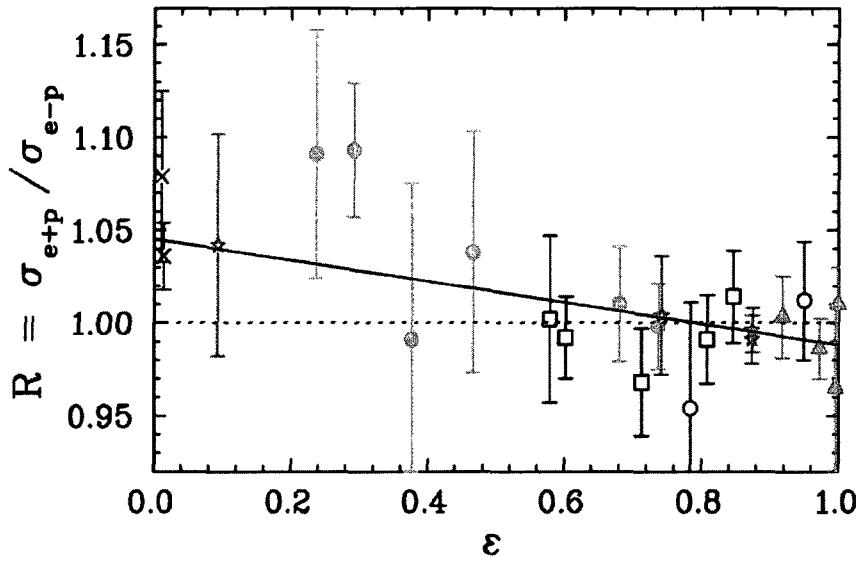

FIG. 22: World data for the positron-proton to electron-proton cross-section ratio ($R = \frac{\sigma_+}{\sigma_-}$) versus ε. Color and symbols indicate the different experiments: solid triangles [33], stars [26], filled circles [27], diamonds [29], squares [28], crosses [32], hollow circles [31]. The plot is taken from [34].

a few high Q^2 data points with larger error bars and limited ε range. According to Arrington reanalysis of this data [34], it supports the idea that TPE can resolve the discrepancy on the extraction of form factors. He found that the size and ε dependence of TPE effects (see Fig. 22) is consistent with the estimated correction based on the observed discrepancy.

Hence this emphasizes the need for additional high precision positron data which covers a wide range in ε and reasonably high Q^2. This kind of data would allow us to extract the TPE correction in a model independent way and determine if the TPE effects can fully explain the existing discrepancy. This is the primary goal of this experiment and the final version of this experiment will certainly meet this goal.

CHAPTER III

EXPERIMENTAL SETUP

The Two Photon Exchange (TPE) experiment was done using the primary electron beam delivered by the Continuous Electron Beam Accelerator Facility (CEBAF) to experimental Hall B. The beam from the accelerator was used to make the mixed beam of electrons and positrons by modification to the existing CEBAF Large Acceptance Spectrometer (CLAS) beamline. The standard CLAS detectors as well as the triggering system were used without modification. In this chapter I will describe CEBAF, the TPE beamline, the CLAS detector and the triggering and data acquisition system.

III.1 CONTINUOUS ELECTRON BEAM ACCELERATOR FACILITY (CEBAF)

The Continuous Electron Beam Accelerator Facility (CEBAF) at the Thomas Jefferson National Accelerator Facility (Jefferson Lab) uses superconducting cavities to accelerate the electron beam. The accelerator can deliver a high quality polarized or unpolarized continuous electron beam with energy up to 6 GeV. The beam can be delivered to the three experimental halls, A, B and C, at the same time. The schematic of the accelerator and the experimental halls is shown in Fig. 23. The electron beam is produced from a strained GaAs photocathode. It is accelerated to a certain energy (45 MeV) in a set of cryomodules and is fed to the racetrack type accelerator that consists of two linacs, the north linac and the south linac. Each linac consists of 20 cryomodules and each cryomodule contains 8 superconducting niobium cavities.

At present the CEBAF accelerator can accelerate the beam up to 0.58 GeV per linac. The beam is first accelerated in the north linac and then enters the recirculating arc. It is then accelerated again in the identical south linac. At this point the beam has made one complete circulation. After a complete pass the beam can be delivered to the experimental halls or it can be recirculated for higher beam energy. The beam can be recirculated up to 5 times, accelerating the electron beam up to 6 GeV.

The accelerator delivers beam currents sufficient to produce luminosities of several times 10^{38} cm^{-2} s^{-1} to experimental halls A and C [35]. The luminosity for Hall B

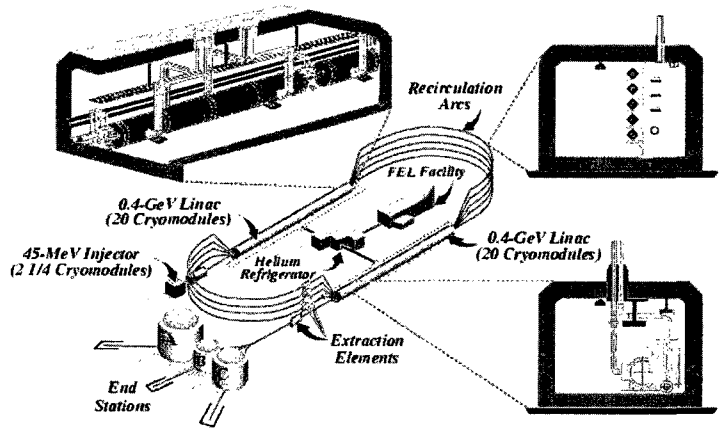

FIG. 23: A schematic view of the accelerator. One of the cryomodules is shown in the upper left corner. A vertical cross section of a cryomodule is shown in the lower right corner. A cross section of the five recirculation arcs is shown in the upper right corner.

is limited by detector occupancies to about 10^{34} cm^{-2} s^{-1}.

III.2 TPE BEAMLINE

The TPE experiment needs a simultaneous electron-positron beam. The beam is made by using the primary electron beam delivered by the CEBAF accelerator. In order to generate the electron-positron beam some additional components were added in the beamline. A simulated picture of the test run beamline is shown in Fig. 24.

The primary electron beam hit a 0.5% radiator located upstream of the tagger magnet. The photon beam so produced is transmitted along the beamline and the electron beam is bent by the tagger magnet to send it to the tagger dump. The photon beam is collimated by an existing 12.7 mm diameter, 12 inch long nickel collimator. The collimated photon beam hit a 5% convertor and generated electron-positron pairs. The unconverted photon beam then travels along the beamline and is absorbed in a "photon blocker", a 4 cm wide, 10 cm high, 20 cm long tungsten block.

The electron-positron beam enters a chicane made up of 3 dipole magnets. We used Frascati Italian Dipoles (IDs) as the first and the third chicane magnets. The Frascati magnets have an aperture of 0.2 m and a pole length of 0.34 m and a maximum field of 1.2 T. The Pair Spectrometer (PS) magnet is used as the second

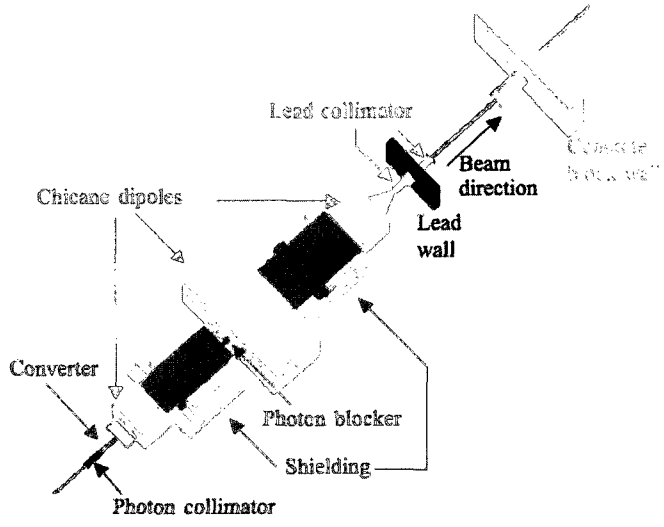

FIG. 24: Picture of the test run beamline used to produce mixed e^+/e^- beam.

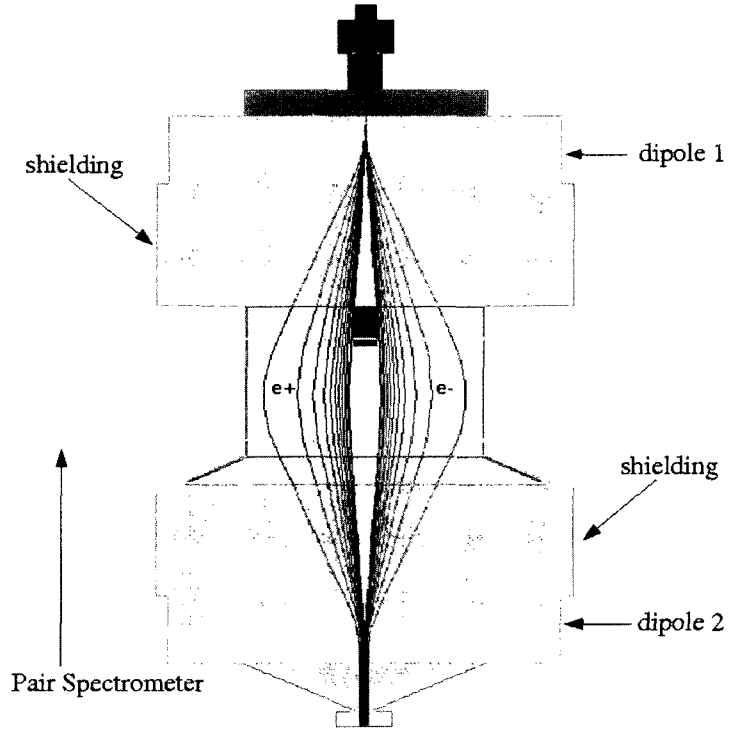

FIG. 25: The simulated trajectories of the leptons through the chicane magnetic system for the test run conditions. The two Frascati dipoles labeled dipole 1 and dipole 2 have fields of 0.42 T, and the pair spectrometer field is equal to -0.385 T. The e^- and e^+ trajectories are shown in right and left of the figure respectively. The beam enters from the top and travels downwards.

chicane magnet. The PS magnet has a 0.5 m aperture (0.4 m within the vacuum box), a 1 m long pole face, and a maximum field of 1.9 T. The chicane is used to separate the electron and positron beams spatially and then recombine them as shown in Fig. 25. The unconverted photon beam is blocked by the photon blocker in the region where the electron-positron beam is separated. Two low energy collimators are also inserted in order to remove the low energy part of the lepton beams. Either lepton beam can also be blocked fully or partially by using one of the two low energy collimators. The photon blocker is represented by a small red rectangle at the entrance of the PS magnet in Fig. 25.

The energy acceptance of the chicane system is from 0.5 GeV to 5 GeV. This gives us all the high energy leptons and removes leptons with $E < 0.5$ GeV. The limitation comes from the aperture of the pair spectrometer magnet (40 cm) and the width of the photon blocker (4 cm). The energy acceptance of the chicane can also be changed by using low energy collimators or by changing the chicane magnetic fields.

The functionality of the chicane system was verified in the October 2006 test run. One of the two lepton beams was blocked by a lead brick covering half of the ID exit aperture and then the first and the third magnet currents were varied together, keeping the PS magnet current fixed. While doing the above procedure, the beam spot was monitored with a scintillating fiber monitor (see Fig. 26) located at the entrance of the CLAS. The procedure was repeated by blocking the other lepton beam. We used the result of the scan as shown in Fig. 27 to identify the chicane magnet currents that optimize the centering and overlap of the lepton beams. After the chicane the beam was then collimated and transported to the target through the CLAS beamline.

After the chicane, a lead shielding wall along with clean up collimators were placed to shield low energy lepton backgrounds. The background rates were recorded using different collimator apertures as well as various clean up collimators. Another useful shielding addition during the test run is also shown in Fig. 24 which is labeled as "concrete block wall". The detail of the shielding study will be described in the next chapter.

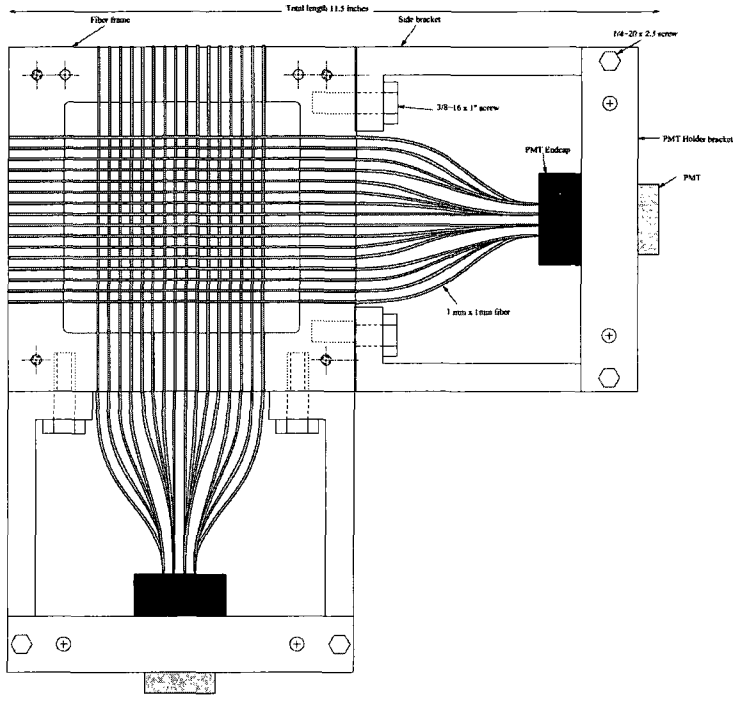

FIG. 26: Scintillating fiber monitor used in the TPE testrun to measure the lepton beam position.

III.2.1 Scintillating Fiber Monitor

A scintillating fiber monitor was used to measure the lepton beam position during the test run. It was located at the entrance of the CLAS immediately before the downstream collimator. The diagram of the scintillating fiber monitor is shown in Fig. 26. It consists of 1 mm by 1 mm multiclad Bicron (BCF-12) fibers with 42 cm radiation length. Half of the fibers were positioned horizontally and the remaining half vertically in order to measure the x and y position of the beam. A set of 16 fibers was attached to a 16 pixel photomultiplier tube in order to amplify and transfer the signals to readout electronics. The online run monitoring software (EPICS) was modified to display the fiber monitor readout during the run. The result of the beam scan with the help of the fiber monitor is shown in Fig. 27.

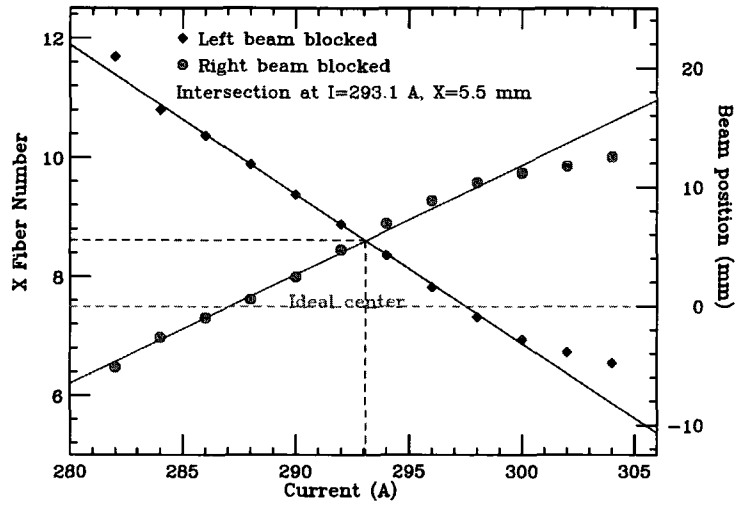

FIG. 27: The lepton beam positions as a function of the first and third dipole magnet current. Data points are the measured beam centroid positions at the fiber monitor and the lines are fits to points 2-10.

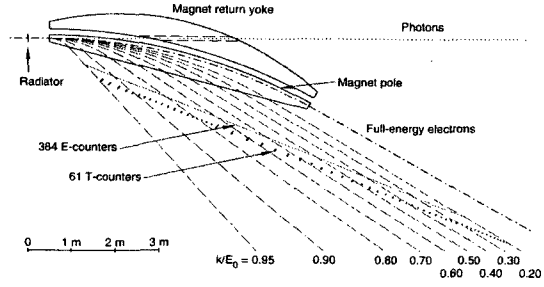

FIG. 28: Tagging system of CLAS. Typical electron trajectories are labeled according to the fraction of the incident energy that was transferred to the photon.

III.3 THE CLAS BEAMLINE AND TAGGING SYSTEM

III.3.1 The Photon Tagger

Electrons from the CEBAF accelerator strike a radiator just upstream of the photon tagging magnet (the "tagger"). The radiator is a thin sheet of a high-Z material such as gold or tungsten. The electron radiates a photon when it is scattered by the electromagnetic field of the nucleus. The energy transferred to the nucleus is negligible. $E_\gamma = E_0 - E_e$ where E_γ is the energy of the emitted photon, E_0 is the energy of the primary electron and E_e is the energy of the scattered electron. The overall geometry of the tagging system is shown in Fig. 28.

E_0 is the known beam energy supplied by the accelerator. At energies above a few MeV, the outgoing electron and photon emerge at very small angles relative to the incident beam direction. The angular distribution of photons has a characteristic angle $\theta_c = m_e c^2/E_0$ and the electron's characteristic angle is given by $\theta_e = \theta_c E_\gamma/E_e$ [36]. At GeV energies both of these angles are of the order of 1 mr or smaller. Thus both the electron and photon travel along the original beam direction. The photon beam is collimated by using the photon collimator. Collimators with several apertures were available for our test run. We used a 12.7 mm diameter collimator which gave us the better signal to background ratio by removing the widely spread low energy part of the photon beam coming out of the radiator.

The electrons that do not radiate follow a circular path just inside the curved edge of the pole face of tagger magnet and are directed to a shielded beam dump below the floor of the experimental hall. Electrons that do radiate experience a smaller radius of curvature in the tagger field and come out of the tagger magnet somewhere along the straight edge of the pole gap. We did not detect these electrons in the TPE experimental test run. They hit the floor.

The tagger magnet is a C-Magnet with a 68000 kg steel yoke. It is completely open along the straight edge to allow free passage for radiated electrons along the entire length. It has a full energy radius of curvature of 11.8 m and deflection angle of 30°. It is 6.06 m in length along the open chord, and has a gap of 5.7 cm. The pole width of the magnet is approximately 0.5 m at the midpoint, tapering to 0.16 m at the ends. A typical magnetic field in the gap for a beam energy of 4 GeV is 1.13 T [36].

III.3.2 Beam Devices

The electron beam delivered to Hall B is monitored by several beam monitoring devices located along the beamline. The beam position and current are measured by beam position monitors (BPMs). The BPMs are made up of three position sensitive RF cavities. There was one BPM located 36 m upstream of the CLAS target that can read the beam current at a rate of 1 Hz. The information from the BPMs helps to keep the beam centered on the target or the radiator.

Another beam monitoring device is called a Harp. The beam profile is measured by moving thin wires (20 and 50 μm tungsten and 100 μm iron) through the beam and detecting the scattered electrons via Cherenkov light in the glass windows of PMTs. The wires are oriented along the x and y axes with the direction of motion at 45° with respect to the horizontal axis. There are three harps upstream of the CLAS target. The TPE experiment used only the tagger harp which is located just upstream of the tagger magnet to measure the electron beam profile. The width of the beam at this location was less than 500 μm.

The harp scan procedure intercepts the beam and hence can only be performed when CLAS is not taking data. It is done after any major changes to the electron delivery or if any other systems show problems with the electron beam.

III.3.3 Target

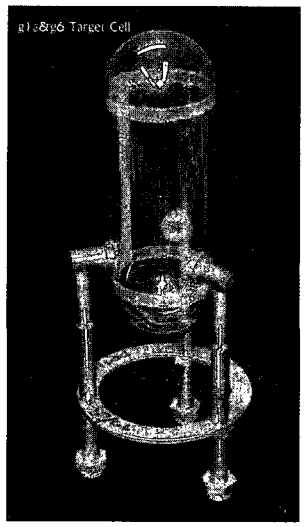

FIG. 29: TPE liquid hydrogen target cell. The mylar target cell is supported by hollow stainless steel legs with copper nozzles.

Several targets are used in CLAS depending on particular needs of electron or photon running. Liquid H_2 is the most commonly used target in CLAS. The target is normally placed at the center of the CLAS detector. It is inserted from the upstream end of the CLAS and is positioned using a support structure. For the TPE test run we used a 18 cm long and 6 cm diameter liquid H_2 target as shown in Fig. 52. Due to the beam divergence, we used a larger diameter target so that it intercepts most of the good beam of leptons. A cryogenic system is used to keep the target liquid. A copper heat exchanger was attached to the target cell and was cooled using liquid hydrogen. The temperature, pressure and density of the target were 20.5° K, 1160 mbar and 0.0708 gm/cm^3 respectively.

III.4 CEBAF LARGE ACCEPTANCE SPECTROMETER (CLAS)

The CLAS (CEBAF Large Acceptance Spectrometer) detector is located in Hall B at Jefferson Lab. It is an almost 4π spectrometer. CLAS can detect almost all of the charged particles produced as a result of nuclear interactions. It uses a toroidal magnetic field for charged particle tracking. The toroidal nature of the magnetic field enables CLAS to measure charged particles with very good momentum resolution. The CLAS magnetic field is provided by six superconducting coils arranged around the beam line. The field points mainly in the ϕ direction. The detector and its components are shown in Fig. 30.

The CLAS detector consists of drift chambers to determine the trajectories of charged particles, gas Cerenkov counters for electron identification, scintillation counters for time of flight (TOF) measurement, and electromagnetic calorimeters to detect showering particles such as electrons and photons and neutrons. The toroidal magnet coils divide the detector into six independent sectors. The sectors are individually instrumented to form six independent spectrometers with a common target, trigger and data acquisition (DAQ) system [35].

The CLAS uses a two level trigger system to initiate data conversion and readout. Each of the components of the detector is described in the following sections.

III.4.1 Torus Magnet

The torus magnet is used to produce the magnetic field for measuring the momentum of charged particles. The field is produced by six superconducting coils arranged in a

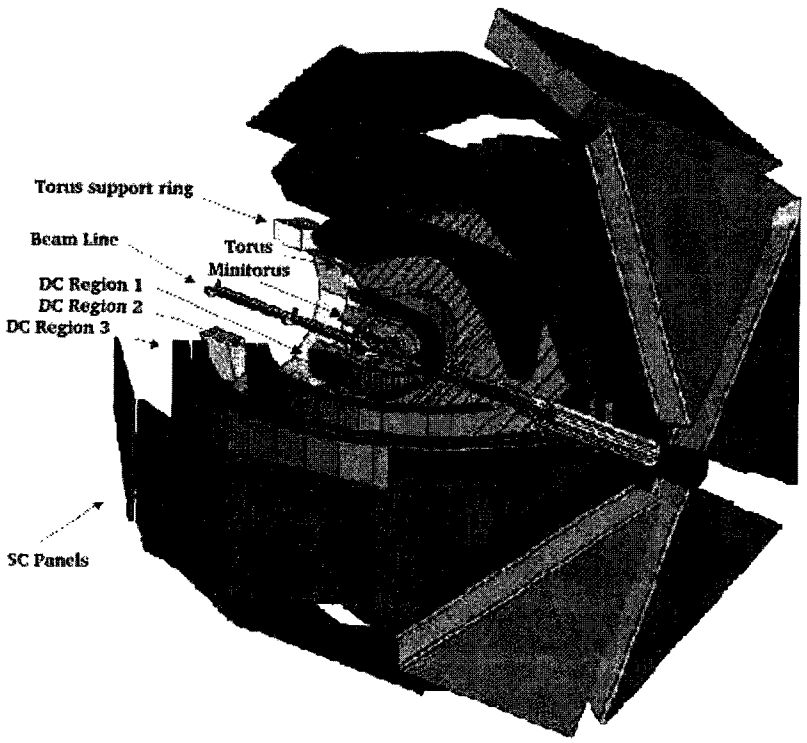

FIG. 30: Three dimensional view of CLAS.

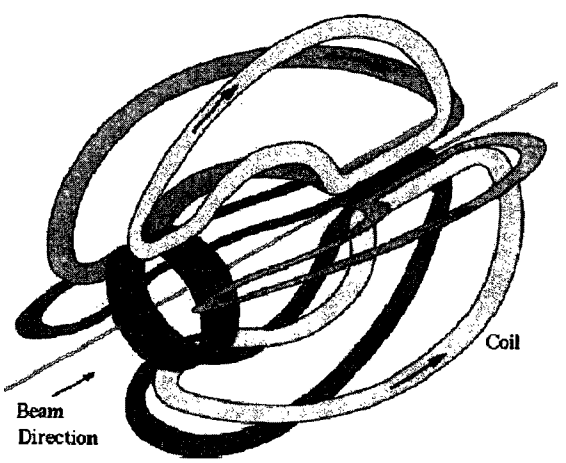

FIG. 31: Configuration of the torus coils.

toroidal geometry around the beam line as shown in Fig. 31. The layout of the coils and contours of constant absolute field strength are shown in Fig. 32. The magnetic field vectors in a plane perpendicular to the torus axis at the target position are shown in Fig. 32. The main field component is in the ϕ direction and there are significant deviations from a pure ϕ field close to the coils. The circular inner shape of the coils minimizes the effect of these deviations on particle trajectories. The magnetic field bends the trajectories of charged particles either toward the beam axis (inbending) or away from the beam axis (outbending)

The shape of the coils is designed so that the forward going particles experience a high field integral (about 2.5 Tm) and large angle particles experience a lower field integral (about 0.6 Tm). The design of the coils also provides a field free region for the operation of the polarized target.

III.4.2 Drift Chambers

Drift chambers are used to measure the trajectories and momenta of charged particles [37]. They track charged particles coming out of the target with momenta greater than 200 MeV/c over the polar angular range from 8° to 142° while covering up to 80% of the azimuth.

In order to do so, all the charged particle tracks that lie within the active part of the drift chambers need to be reconstructed. The track resolution obtained from the CLAS drift chamber system for a 1 GeV/c charged particle is $\delta p/p \leq 0.5\%$ for the reconstructed momenta and $\delta\theta$, $\delta\phi \leq 2$ mrad [37] for the reconstructed scattering angles. To achieve this resolution the track has to be measured at three locations along its trajectory with an accuracy of 100 μm in the bend plane of the magnetic field and 1 mm perpendicular to the bend plane. Total material in the tracking region of the detector needs to be less than one percent of a radiation length in order to reduce multiple scattering.

The magnet coils separate the detectors into 6 independent sectors. In order to simplify the detector design and construction, 18 separate drift chambers were built and placed at three radial locations in each of the six sectors. These radial locations are called regions.

The region one chambers are closest to the beamline and surround the target in an area of no magnetic field. The region 2 chambers are somewhat larger and are situated between the magnet coils in an area of high field near the point of maximum

track sagitta and the region 3 chambers are the largest devices and are radially located outside of the magnet coils.

The wedge shaped sector of the drift chambers are filled with wires stretched between two end plates each parallel to its neighboring coil plane. The end plates are tilted at 60° with respect to each other. This design provides the maximum sensitivity to the track curvature since the wire direction is approximately perpendicular to the bend plane. The wire pattern in the drift chambers is quasi-hexagonal with six field wires surrounding one sense wire. The cell size increases with increasing radial distance from the target. The average distance between field and sense wires for region 1, region 2 and region 3 drift chambers are 0.7 cm, 1.5 cm and 2.0 cm respectively. For pattern recognition and tracking redundancy the wire layers in each chamber are grouped into two superlayers of six wire layers each, one axial to the magnetic field and the other tilted at a 6° stereo angle to provide azimuthal information. Due to space constraints the stereo superlayer of region 1 contains only four wire layers. There are 128 sense wires per layer in region 1 and 192 wires per layer in regions 2 and 3. This gives a total of about 35,000 sense wires in the drift chamber system of CLAS.

The drift chambers are filled with an 90/10% mixture of argon and CO_2 [37]. This choice is based on system safety and operation lifetime. An active feedback system maintains constant differential pressure at the chamber regardless of atmospheric fluctuations by making small adjustments to the outflow. The gas has a fairly saturated drift velocity of about 4 cm/μs, and has an operating voltage plateau of several hundred volts before breakdown occurs. It also provides good efficiency, adequate resolution and reasonable collection times.

The high voltage system maintains the sense wires at a positive potential and the field wires at a negative potential whose absolute value is half that of the sense wire. The high voltage settings were determined from a plateau run, resulting in individual layer efficiencies of greater than 98%. The operating voltages for sense wires of regions 1, 2 and 3 are 1266 V, 1400 V and 1500 V respectively [37].

The charged particles passing through the drift chambers ionize the gas molecules. The electrons and ions produced in the ionization process drift towards the cathode (sense) and anode (field) wires respectively. When the drifting electrons move closer to the sense wires they experience higher fields and at some point they acquire sufficient energy to ionize other gas molecules. This results in a multiplication of collected

electrons and ions. The detected electric signals provide information about the particle's drift time which can be translated to the hit positions of the original charged particles passing through the drift chambers. The electrical signals then pass through pre-amplifiers mounted on printed circuit boards attached to the chamber endplate. The outputs from the pre-amplifiers are passed to a crate-mounted post-amplifier and discriminator board (ADB) which produces digital output pulses. These pulses are fed to the multi-hit, common-stop time-to-digital (TDC) board. The TDCs are then stopped by the event trigger.

Tracking resolution is the deviation of the reconstructed momenta and angles of the charged particle tracks from their true values at the interaction vertex. Tracking uncertainties arise due to multiple scattering in the material along the particle trajectory, from geometrical misalignments of the separate chambers, lack of knowledge of the real value of the traversed magnetic field strength and the single wire resolution. The average single wire resolution is about 200–250 μm. The whole-cell average resolution is about 310, 315, and 380 μm for region 1, region 2 and region 3 chambers respectively [35, 37].

The tracking efficiency decreases at high luminosity. A one percent increase in chamber occupancy (average hits per sector per event) decreases the tracking efficiency by approximately one percent. The efficiency of region 1 chambers decreases significantly above an occupancy of 4%. So region one chambers are operated at an occupancy of less than 3%.

III.4.3 Čerenkov Counters

The Cherenkov Counter (CC) is used in CLAS for triggering on electrons and separating electrons from pions. It covers the polar angular range from 8° to 45° and is designed in such a way that it covers most of the solid angle in each of the six sectors. In order to achieve better energy resolution, the least possible amount of material is used. Light collecting cones and photo multiplier tubes (PMTs) are placed in the region of ϕ that is already blocked by the torus magnet coils. The light collection optics focus the light only in the ϕ direction, which preserves the information on the electron polar angle θ.

The full θ range of each of the 6 sectors are divided into 18 regions and each θ segment is divided into two modules about the symmetry plane bisecting each other. As a result, there are 12 identical sub-sectors around the ϕ direction for each

θ interval and 216 light collection optics. The optics of each θ module is designed to focus the light into a PMT associated with that module. The optical arrangement of one module is shown in Fig. 34.

Charged particles traveling through the medium with a speed exceeding the local phase velocity of light emit electromagnetic radiation. The velocity threshold for Čerenkov light emission is β=1/n where n is the refraction index of the medium. The Čerenkov material used is perfluorobutane C_4F_{10}, which has n=1.00153. That corresponds to a threshold in energy of the particle:

$$E = \frac{m}{\sqrt{1-\beta^2}} = \sqrt{\frac{n}{n-1}}m = 18.09\ m,$$

where m is a mass of the particle. This provides an acceptably high pion momentum threshold ($p_\pi > 2.5$ GeV/c) [38].

We did not use the CC for this TPE test run.

III.4.4 Time of Flight System

The Time of Flight (TOF) counters are used to measure the arrival time of the particles with very good timing resolution. It is used for particle identification and triggering. It covers the polar angular range between 8° to 142° and the entire range in azimuthal angle ϕ. It consists of arrays of scintillators which are located radially outside of the tracking system and the Cherenkov counter but in front of the calorimeters. The view of the TOF counters in one sector is shown in Fig. 35.

Each of the six sectors has 57 scintillators with a photomultiplier tube (PMT) attached at each end. The last 18 scintillators are paired into nine logical counters which result in a system with a total of 48 logical counters per sector. These counters are mounted in four panels in each of the six sectors. Panel 1 consists of scintillators 1 to 23 and covers the polar angular range less than 45° and are called forward angle counters. Panels 2, 3, and 4 are called large angle counters. The forward angle counters consist of 15 cm wide scintillators with 2 inch PMTs whereas the large angle counters have 22 cm wide scintillators with 3 inch PMTs [39]. All of the scintillators are 5.08 cm thick to give a large signal for minimum ionizing particles compared to the background. The lengths of the counters vary from 12 to 445 cm. Bicron BC-408 is used for the scintillation material. This provides the required fast time response and low light attenuation. The 2 inch Thorn EMI 9954A PMTs are used for the forward angle TOF system. This selection is based on cost effective solution to cover

large area while maintaining good time resolution compared to other PMTs. In the case of the large angle counters, the requirements for angular and timing resolution were reduced so the 3 inch Philips XP432 B/D PMTs are used.

The TOF electronics processes prompt signal for the CLAS Level 1 trigger as well as signals for pulse height and timing analysis. A trigger from a TOF counter is initiated by events that deposit energy in the scintillator greater than a certain threshold value. The PMT dynode pulses go to a pre-trigger circuit where two signals are produced. One of these signals goes to the Level 1 trigger and the other is used to accept the corresponding signals of the low level discriminators. Custom electronics are used for the energy discrimination in the pre-trigger circuit. The charge of the anode pulse is recorded by a LeCroy 1881M FASTBUS ADC for later analysis. The time of the particle is recorded by a LeCroy 1872A FASTBUS TDC [39]. Using the arrival time of the particle from the TOF counter in conjunction with the tracking information, the TOF system allows us to measure the velocity of the particle and hence help identify the particle mass using the relation $m = p\sqrt{(1-\beta^2)}/\beta$. The average time resolution of the scintillator counters is about 140 ps, which allows us to separate reliably pions and protons up to a momentum of 2.5 GeV/c.

III.4.5 Electromagnetic Shower Calorimeter

The Electromagnetic Calorimeter (EC) of CLAS is used to identify electrons, neutrons, and photons. Generally it is used for detection and triggering of electrons at energies above 0.5 GeV, detection of photons at energies above 0.2 GeV, and detection of neutrons, assuming their separation from photons based on timing information [40].

The forward Electromagnetic Calorimeter (EC) covers the polar angular range up to 45°. It is made up of layers of scintillators strips and lead sheets with a total thickness of 16 radiation lengths. It is a lead scintillator sandwich where the lead to scintillator ratio is 0.24. The EC is divided into six EC modules, one for each sector of CLAS. The lead-scintillator sandwich has the shape of an equilateral triangle. Each sandwich contains 39 layers and each layer is made up of a 10 mm thick scintillator followed by a 2.2 mm thick lead sheet. The area of each successive layer of EC increases linearly with the distance from the nominal target position. For readout purposes, each scintillator layer is made up of 36 strips parallel to one side of the triangle with the orientation of the strips rotated by 120° in successive

layers as shown in Fig. 36.

Thus there are three orientations or views labeled U, V and W, each containing 13 layers that provide stereo information on the location of energy deposition. Each orientation containing 13 layers is further sub-divided into an inner (5 layers) and outer (8 layers) stack, to provide longitudinal sampling of the shower for improved particle identification. Each module thus requires 36 strips $\times$ 3 views $\times$ 2 stacks = 216 PMTs. There are 1296 PMTs and 8424 scintillator strips in the six EC modules used in CLAS detector [40].

A fiber optic light readout system is used to transmit the scintillator light to the PMTs. These fibers are bent in a controlled way to form semi-rigid bundles originating at the end of scintillator strips and terminating at a plastic mixing light guide adapter coupled to a PMT.

In order to reconstruct a hit in the EC, energy deposition is required in all three views (U, V and W) of the inner or outer layers of a module. The groups of strips fired in each of the three views are identified. Neighboring strips are also placed in groups if their PMT signals are above a software threshold. The position centroid and root mean square of each group are calculated. After finding all groups, intersection points of different groups from each view are reconstructed. Each intersection corresponds to a hit. Using the path lengths from the hit position of readout edge, the energy and time of the hit are calculated. An event with hits reconstructed in five EC modules is shown in Fig. 37.

The energy resolution of EC can be parameterized as $\frac{\sigma}{E} = \frac{10.3\%}{\sqrt{E(GeV)}}$. The position resolution for an electron shower with more than 0.5 GeV of energy is 2.3 cm. The timing resolution for electrons is about 200 ps over the entire detector [35].

III.5 TRIGGER AND DATA ACQUISITION (DAQ)

III.5.1 Trigger

CLAS uses a two-level hierarchical trigger system to collect events of interest. The level 1 trigger uses prompt information from PMT channels to determine the desired event. In this measurement it used the signals from the fast PMT channels of the TOF detector (SC) and the Electromagnetic Calorimeter (EC). The hit patterns from these detector subsystems are compared to patterns preloaded in memory tables for rapid response.

In order to reject events that do not have matching particle trajectories in the drift chamber system, the Level 2 trigger is used. It finds likely tracks in each sector of the drift chamber, performs a correlation with the Level 1 trigger, and generates a "Level 2 fail" signal if no correlated tracks are found. Level 2 processing time is related to the dead time of the detector.

Likely tracks are identified by finding track segments in five superlayers in each sector. Track segments are found by comparing DC hits with nine templates that are designed to catch all tracks passing through a superlayer at angles of up to 60°. A likely track in a sector is tagged when track segments are found in three of the five superlayers.

The Trigger Supervisor (TS) uses Level 1 and Level 2 triggers as inputs and produces all common signals, gates and resets required by the detector electronics. It can be programmed to require only a Level 1 input (CLASS1) or to require both a Level 1 input and a Level 2 confirmation (CLASS2). In case of a CLASS1 trigger, the TS generates the gates upon receiving any Level 1 input, waits for conversion of all crates to complete and then places the event on a readout queue to initiate readout. In the CLASS2 trigger, the TS also generates the gates on Level 1 input, but then waits about 3.2 μs for a Level 2 confirmation. If Level 2 fails, TS sends a fast clear which causes all the electronics to reset and become active again. If Level 2 is satisfied, the front end modules will be allowed to convert, and the event will be placed on the readout queue for readout.

In this experiment, the leptons are created by the pair production process at the convertor and are tertiary particles of unknown energy. Since the initial lepton energy is unknown, we need to detect both the scattered lepton and the recoil (scattered) proton to fully reconstruct an event. The usual single-electron trigger used by CLAS is not suitable for this purpose. The CLAS trigger which is based on the Cerenkov counter and electromagnetic shower calorimeter would miss electrons and positrons at larger angles, which would limit the kinematic coverage in ϵ. It may also be biased by the Cerenkov counter due to its different efficiency for outbending and inbending tracks.

So in order to meet our requirements a trigger designed to detect $e^+ - p$ coincidences was used. This trigger required two charged tracks in opposite sectors and was constructed by requiring hits in the time of flight (TOF) counters in opposite sectors. For a few runs, a Level 2 (drift chamber) trigger in the opposite sector was

also required [17]. This requirement is fulfilled by the usual Level 2 CLAS trigger.

A simple simulation was performed to determine the kinematic coverage in the (Q^2, ϵ) plane using the opposite sector TOF trigger. The kinematically allowed region in Q^2 and ϵ for an opposite sector TOF trigger is shown in Fig. 38. This plot shows only those events for which both the electron and proton strike a paddle in the TOF system. The kinematically allowed TOF paddle number combinations in opposite sectors are shown in Fig. 39 where the TOF panel boundaries are separated by vertical and horizontal lines. To reduce the accidental trigger rate due to uncorrelated panel-4/panel-4 coincidences, we used a trigger that required a hit on TOF panel 1 in one sector in coincidence with a TOF hit on any panel in the opposite sector. A minimum ionizing signal in the forward calorimeter was also required in the same sector as the TOF panel 1 hit [17]. This trigger eliminates a small region of the allowed (Q^2, ε) plane that corresponds to panel-2/panel-2 coincidences as shown in Fig. 39. In the future, this small hole in the kinematically covered space can be removed by allowing events that have TOF hits on panel 2 in one sector and panel 2 in the opposite sector.

III.5.2 Data Acquisition (DAQ) and CLAS Data Flow

The CLAS DAQ system was designed for an event rate of 2 kHz. The continued development of the DAQ over the years resulted in operation in the range of 3–4 kHz. The present data output rate is 25 MByte/s, constrained by the file system (use of UNIX or speed of the raid disks that store the data) not by the experimental hardware.

The CLAS data flow system is described in Fig. 40. The data of all the detectors are digitized in FASTBUS and VME crates within the Hall and collected by the VME Readout Controllers (ROCS) in the crates. Arrays of digitized values are translated into tables in which each data value is associated with a unique identity number describing the active component within the detector. These data arrays are buffered and then transferred to the CLAS online acquisition computer (CLON10). The main data flow element in the CLON10 consists of the Event Builder (EB), Event Transport (ET) and Event Recorder (ER). EB assembles the incoming fragments into complete events. For some detectors like the DC, the EB combines some crate fragments into larger tables and banks. Finally, the completed event is labeled by a run and event number, an event type, and the trigger bits and all are combined in a

header bank.

EB passes the completed event to shared memory (ET1). The ET system manages this shared memory allowing access by various event producer and continue process on the same or remote processor systems. The ER picks up all events for permanent storage. It writes the data to the RAID disks and the data from the RAID disks are later transferred to the remote tape silo for permanent storage. Some events are also transferred to the remote ET systems ET2 and ET3 as shown in Fig. 40 for raw data checks such as hit maps, status and event displays. It can also be used for online reconstruction, analysis and monitoring.

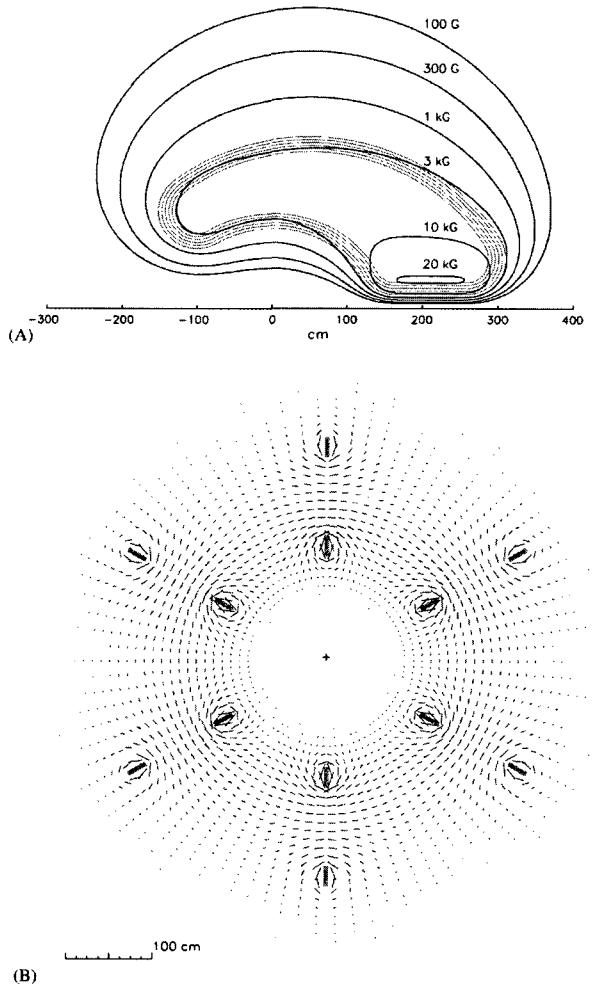

FIG. 32: (A) Contours of constant absolute magnetic field for the CLAS toroid in the midplane between two coils; (B) Magnetic field vectors of the CLAS toroid transverse to the beam in a plane centered on the target. The six coils are shown in cross-section.

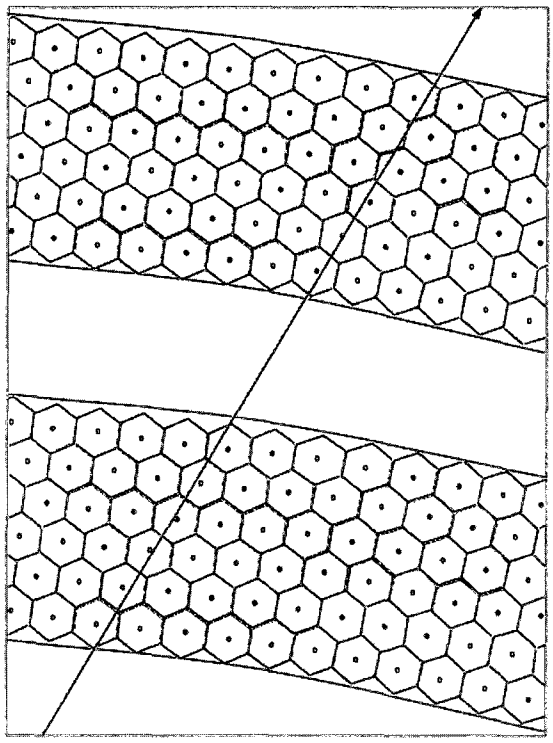

FIG. 33: Portion of region 3 drift chamber showing the layout of its two superlayers. The wires are arranged in hexagonal patterns. The sense wires are at the center of each hexagon and the field wires are at the vertices. Passage of a charged particle is shown by the highlighted drift cells.

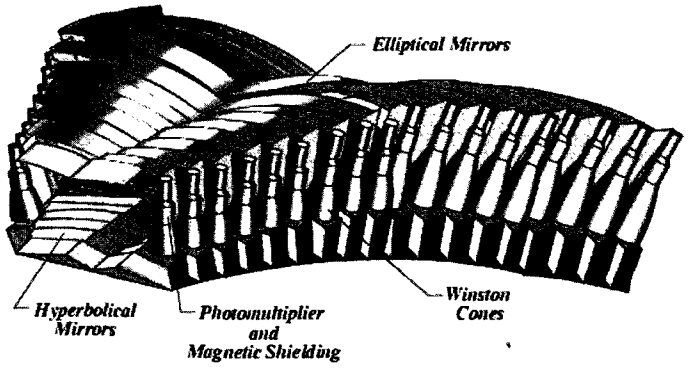

FIG. 34: Array of CC optical modules in one of six sectors.

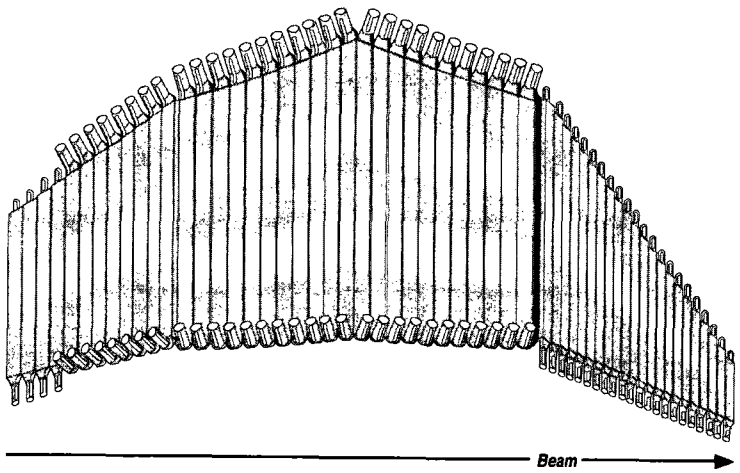

FIG. 35: The four panels of TOF scintillator counters for one of the sectors. Scintillators have different light guides and PMT's for different scattering angle coverage.

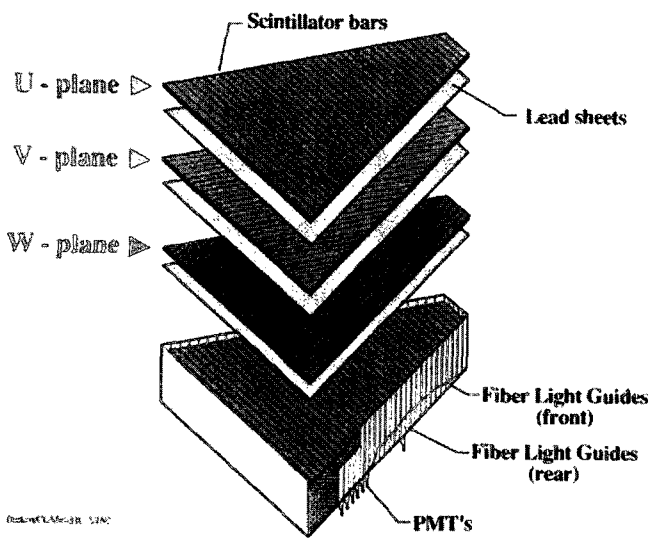

FIG. 36: View of one of the six CLAS electromagnetic calorimeter modules.

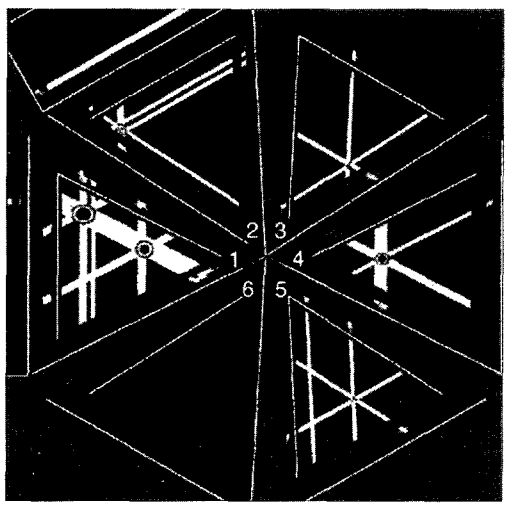

FIG. 37: Event reconstruction in the EC. In sectors 2, 3, 4 and 5, a single intersection of peaks on each view (U, V, W) is found, while in sector 1, two hits are reconstructed. The transverse energy spread is represented by the size of the oval.

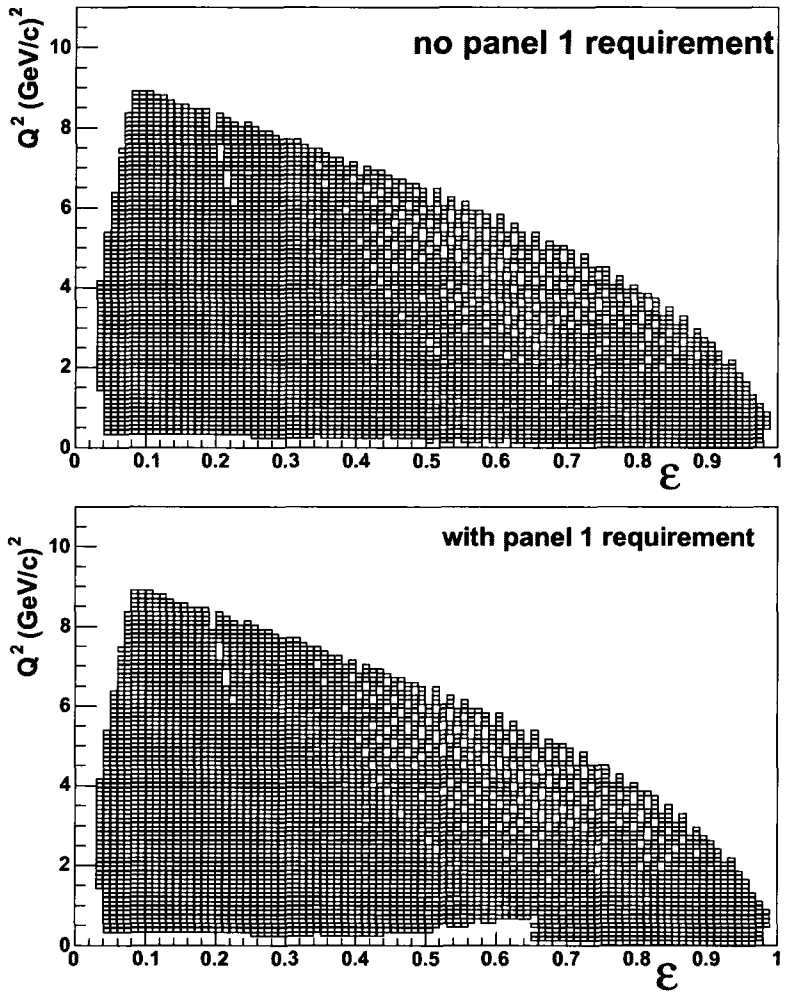

FIG. 38: The kinematically allowed region in Q^2 and ε for an opposite sector TOF trigger for I_{torus} = 1250 A. The top figure does not require a hit in TOF panel-1 while the bottom figure requires a hit in TOF panel–1 in either sector.

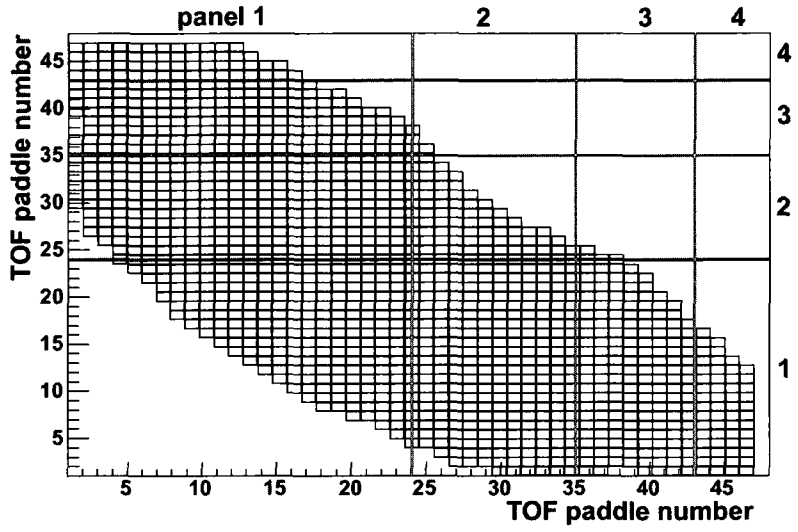

FIG. 39: The kinematically allowed TOF paddle pairs for an opposite sector TOF trigger. The vertical and horizontal solid lines indicate the TOF panel boundaries.

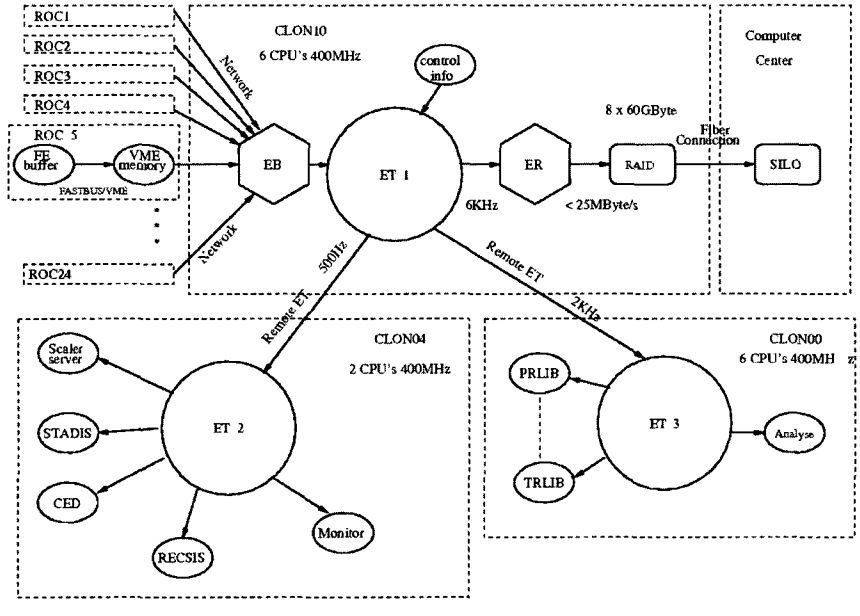

FIG. 40: Data flow schematic for CLAS.

CHAPTER IV

BACKGROUND STUDY

The Two Photon Exchange (TPE) experiment requires a simultaneous mixed electron-positron beam to study the positron-proton to electron-proton elastic scattering cross-section ratio. The beam is produced starting from a high energy primary electron beam from the CEBAF accelerator. In order to produce a high luminosity tertiary beam it is crucial to reduce the backgrounds to a very low level. This requires a detailed study to find background sources and the ways to control them.

We did several test runs and developed a simulation in parallel to thoroughly understand the backgrounds. The simulation was validated by using the latest test run data taken in October 2006 and the valid simulation was used to further improve the beamline design by finding more background sources, removing the possible sources and shielding the remaining sources of backgrounds. The detailed study is described in the following sections of this chapter.

IV.1 EARLIER TEST RUNS

It was assumed in the earlier estimates that the dominant background that limits the luminosity must be from the photon blocker since it absorbs the high energy photon flux and is not very far from the CLAS center. But the earlier test runs indicated that the backgrounds from the photon tagger and the tagger dump are much larger than that from the photon blocker. These were from electrons striking the exit flange of the tagger vacuum box. The electrons that do not radiate leave the tagger vacuum box through the tagger exit beam pipe but the electrons that radiate low energy photons are bent slightly more by the tagger field and hit the exit beam pipe, a flange or the end of the vacuum box itself. This was tested in the December 2004 test run by measuring the background rates in the TOF detectors. The tagger magnet field was varied to change the beam position inside the tagger beampipe. The TOF rates were recorded (see Fig. 41).

The highest counts were in the near most TOF counters that were closest to the tagger vacuum box exit. The higher magnetic field bends the electrons more and more electrons hit the bottom side of the beampipe. For the case of lower magnetic field, the electrons bend less and fewer electrons hit the bottom side of the beampipe.

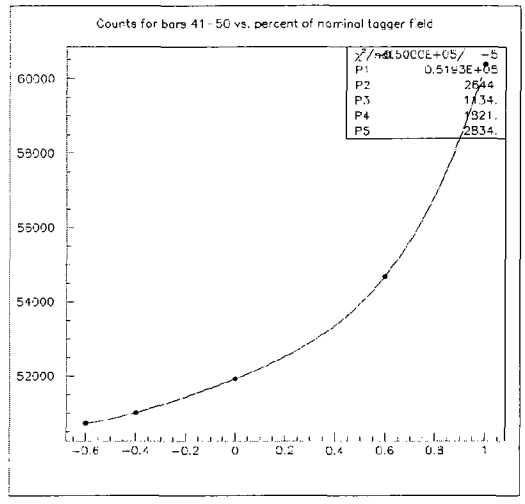

FIG. 41: Counts in the back angle TOF detectors 41-48 vs. the shift in the tagger magnetic field (%).

This test clearly showed that the radiated electrons hit the exit beampipe, flanges and the tagger vacuum box exit present in the tagger beamline as shown in Fig. 42 and creates backgrounds which can easily reach the outer CLAS detectors such as TOF.

Another parasitic test run was conducted in June 2005 to measure the neutron backgrounds in the hall. A borated polyethylene (BPE) shield wall (60 cm thick, 120 cm wide and about 3.5 m tall) was added downstream of the concrete wall on the floor of the hall. The BPE was placed on the right side of the beam and two liquid scintillator neutron detectors (ND) were placed 2.5 m above the floor downstream of the concrete wall. One ND was placed beam right behind the BPE and the other was placed beam left to check the effect of the BPE on the background. The prompt and delayed signal from NDs were recorded in order to isolate neutron and non neutron backgrounds. Only a few percent (1-3%) of the backgrounds was found to be neutrons. The effect of the BPE wall was found to be very small and no difference in TOF rates between beam left (sector 6) and beam right (sector 5) was observed.

We also measured neutron rates using twenty Thermoluminescence Dosimeter (TLD) badges with a neutron-sensitive chip (CR-39) with a 0.5 MeV threshold placed in many locations in the hall. This test run was conducted parasitically during the g8 run with standard photon beam. So this study was done without using a

FIG. 42: The exit of the tagger vacuum box before modification. The beam exit pipe is the straight pipe exiting the figure in the middle of the right side. The background sources in this area such as small diameter beam pipe, flanges and pump out port are also shown.

photon blocker. The TLD measurements clearly indicated that the tagger vacuum box exit is the major source of neutron background and this is shielded by lead and concrete walls downstream of the tagger exit. The photon beamline through which the radiated photon travels towards the target was also found to be a small source of neutron background. This may underestimate the neutron background from the photon beamline because of the absence of the photon blocker. The distribution of the neutrons in the hall is shown in Fig. 43.

During the g8 run period some data was taken with DC and TOF detectors on. The DC wire hits and TOF rates were recorded during the run. This was a photon run so there was no photon blocker to stop the photon beam. The result of this test run is shown in Fig. 44. This showed the higher occupancy in R3 DC as well as several hot spots in the R1 DC which is shown in Fig. 44 (left). The TOF rate on the back angle TOF paddles are found to be higher compared to the forward angle paddles (40–48) as shown in Fig. 44 (right). This result is consistent with the TOF rates seen in December 2004 test run shown in Fig. 41.

Based on these test runs results we started the GEANT4 simulation of the TPE

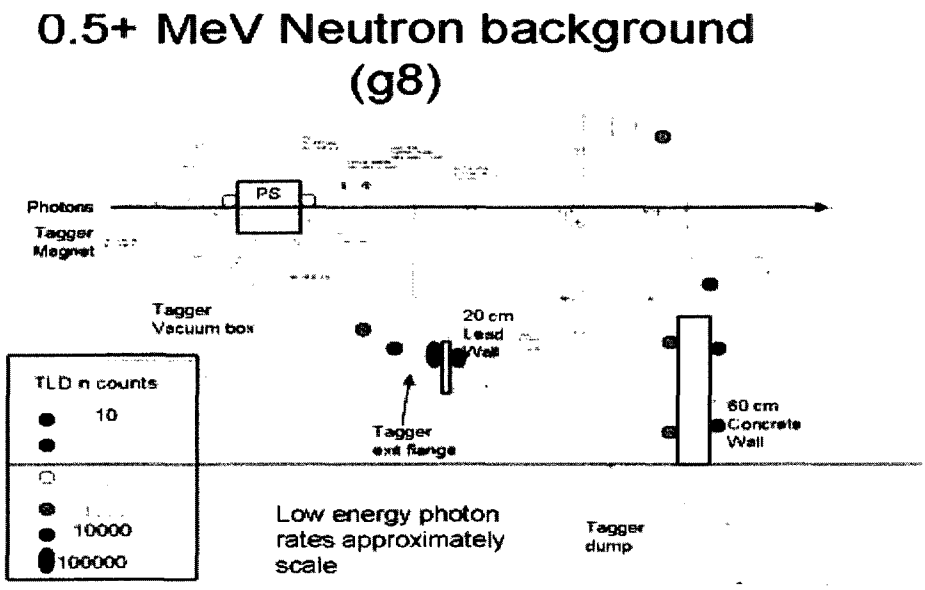

FIG. 43: The relative counts in the CR-39 neutron detectors located at various positions in the hall during the g8 run period. The tagger vacuum box exit shows the highest background. The lowest background is downstream of the concrete shield wall.

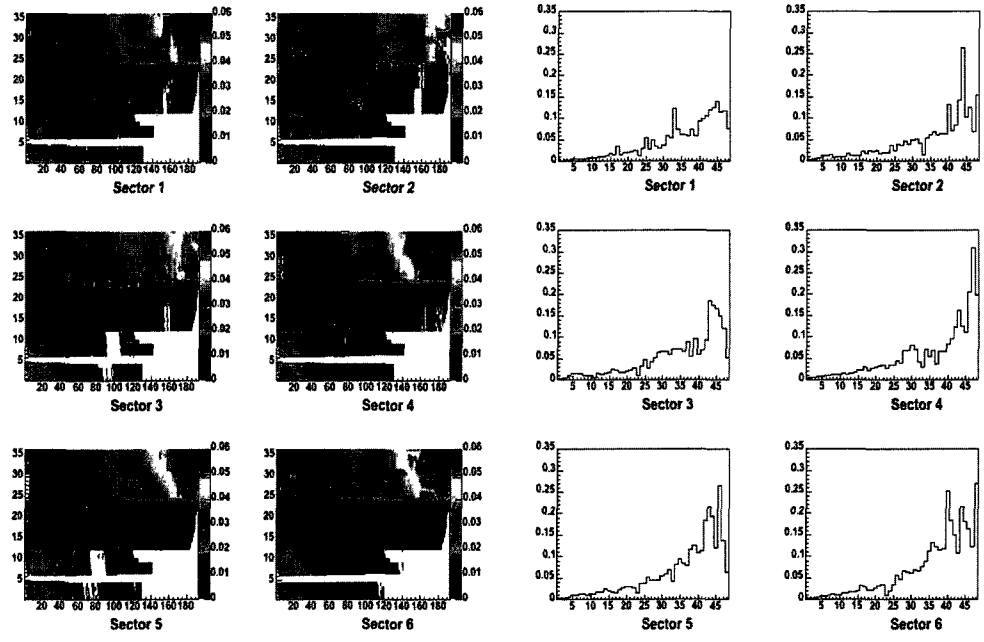

FIG. 44: The DC and TOF background rates measured during g8 run period. Left: DC wire layer vs. scattering angles for each sector. Right: TOF rates vs. paddle number for each sector.

beamline. Various beamline and shielding configurations were tried in order to reduce the tagger related backgrounds observed in the test runs described above.

IV.2 TPE SIMULATION PACKAGE

The TPE simulation package is built using GEANT4 version 4.8.1. GEANT4 is a simulation toolkit used to simulate the interaction of particles with matter. It is written in the object oriented C++ programming language. The detectors, the particles, the physics processes, the event generator as well as all the requirements of the simulation must be provided by the user to GEANT4 using GEANT4 toolkit classes. The description of GEANT4 is beyond the scope of this thesis. Detailed information regarding GEANT4 can be found in reference [41].

In the GEANT4 simulation, the geometry of each and every component of the experimental setup needs to be defined by the user. Simulation of the TPE experimental setup is complicated because it requires the inclusion of most of the CLAS beamline components and the detectors. To make it simple and user friendly, we divided the entire experimental setup into several small branches consisting of particular parts of CLAS. It is mainly divided into Hall B, beamline, tagger, dc, tof and target.

- Hall B: Hall B is the "mother volume", a very large geometrical volume similar to the experimental hall where all the components of the experimental setup are placed, made as a very big rectangular box filled with air. It contains all the geometry and detectors (daughter volumes) of the TPE setup. The shape, size, position, orientation and material of the every component of CLAS were extracted from the official Hall B engineering drawings and were implemented in the simulation as closely as possible. All the daughter volumes (components of Hall B) were placed inside the mother volume (Hall B) in their respective position by using the position information extracted from the above mentioned drawing.

- Photon Beamline: The photon beamline starts at the very upstream part of the CLAS and consists of all the beamline components such as radiator, collimators, convertor, magnetic chicane, photon blocker, vacuum and beampipes.

- Tagger Beamline: The tagger beamline part of the simulation starts at the

tagger magnet and continues to the tagger beam dump. It consists of all the components in the taggerline as well as the shielding we added to control the backgrounds.

- TOF Detector: The TOF detector was originally simulated as a simple concentric spherical shell of scintillating materials. This was used to find background sources and shielding before the 2006 test run and was only capable of providing qualitative measurements of the backgrounds. After the 2006 test run this was developed into a more realistic and complicated TOF detector similar to that of CLAS.

- Drift Chambers: Drift chambers were built in the earlier version of the TPE simulation as the segment of sphere made up of DC gas but were not used much in the simulation before the 2006 test run. After the 2006 test run, DC region 1 and 3 were developed and used to study the background rates and to find the background sources. All the DC cells were added into the simulation and now we can simulate the data similar to the test run and compare.

- Target: The target consists of a target cell, scattering chamber, condenser ring, beampipe, shielding and all the crucial components downstream of the target.

An event starts with an electron generated at a point very upstream of the CLAS beamline. The electron is propagated along the beamline. The electron interacts with the materials in the beamline. We used the GEANT4 standard physics libraries and added some more libraries such as LHEP-BIC-HP and QGSP-BERT-HP to handle the particle interactions with matter. All the daughter particles produced in the interaction were tracked starting from the radiator to the CLAS detector. Information of the particles such as energy, position, and type were recorded at various locations by putting tracking planes at each location. For each particle's track, DC wire hits and total energy deposited in the TOF scintillator paddles were recorded.

The TPE simulation package can be executed in two ways. The interactive mode is used to visualize the geometry and the path of the particle tracks. When the run is started in this mode, it shows an OpenGL graphics window in which we can see the geometry and the tracks of the particle paths. This helps in finding overlaps between different geometrical volumes and visualizing the particles' tracks as they

pass through different materials. One can use different colors to identify the tracks of particles depending on the particle charge or type.

The batch mode is used to run jobs in order to simulate the particular configuration after debugging everything in the interactive mode. Any number of events can be simulated in batch mode and the output can be stored in root files for further analysis. This type of simulation study requires submitting many jobs for various configurations and needs a larger computing facility. We used the Jefferson Lab scientific computing system to submit jobs.

In GEANT4 once the run begins neither the detector setup nor the physics processes can be changed until all the jobs were done completely. So in order to save time we made several input files for each branch of the geometry that contains parameters that need to be changed for the various configurations to be simulated. Using a set of input files for each configuration one can submit jobs with the same executable. This requires modifying only the input parameters in input files for the different configurations and we do not need to compile the package for each of the configurations. This makes it possible to simultaneously submit set of jobs with different configurations to the Jlab scientific computing system.

IV.3 SIMULATION PRIOR TO TEST RUN 2006

The purpose of the simulation prior to the 2006 test run was to reproduce the results of the earlier short test runs and then use it to find the primary background sources, improve the beamline to reduce the backgrounds, and design the experimental setup for the upcoming engineering test run. To begin with we simulated the existing CLAS beamline starting from the tagger which was found to be the major source of backgrounds in the earlier test runs described above. The simulation of the photon beamline and target area were developed simultaneously in order to identify and reduce the background sources in these areas. The detailed study of tagger, beamline and target related backgrounds is described in the following subsection.

IV.3.1 Tagger Related Backgrounds

The primary electrons hit a thin radiator upstream of the tagger magnet and radiate bremsstrahlung photons. The photons so produced travel along the photon beamline towards the target. The electrons that do not radiate are bent less by the tagger

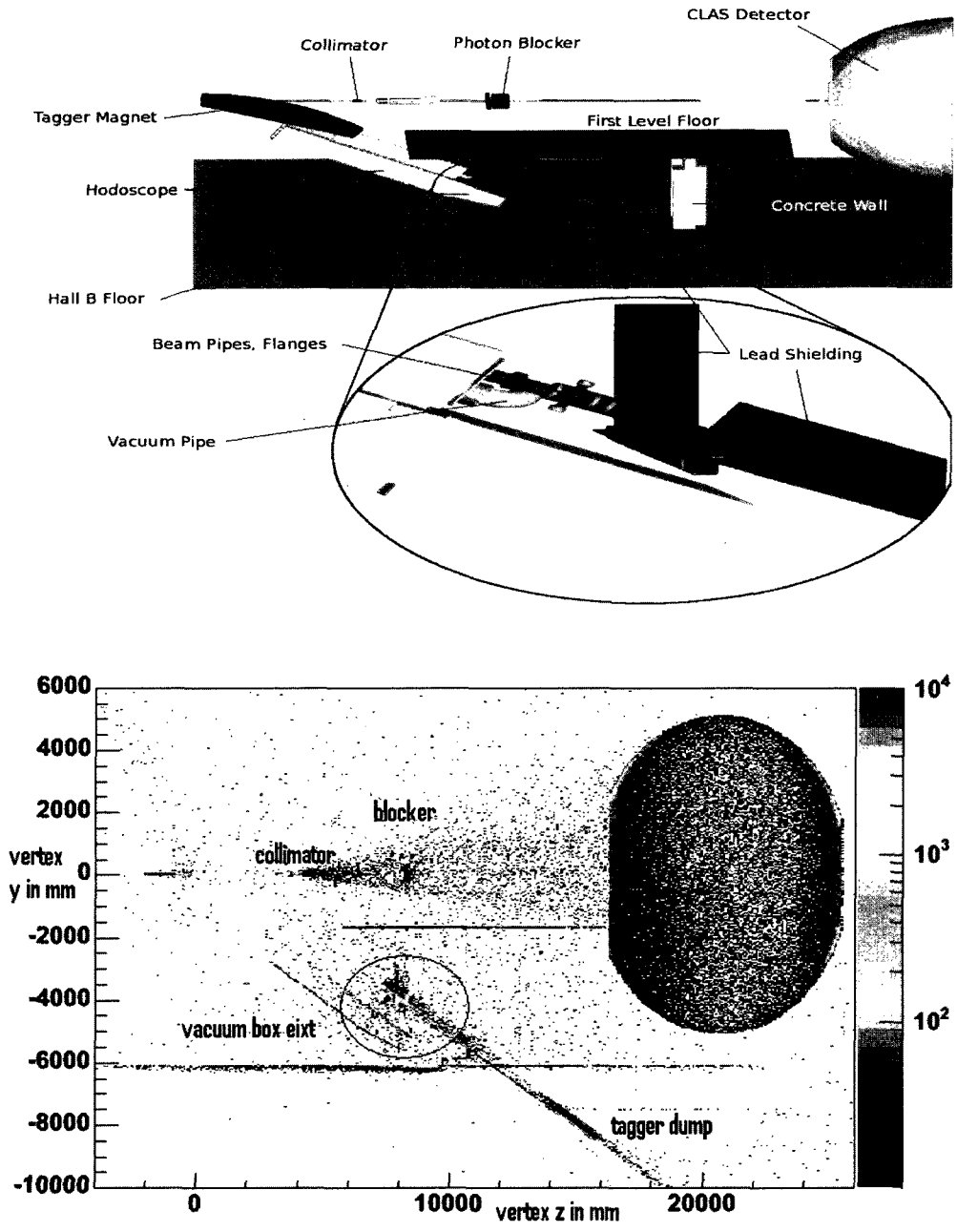

FIG. 45: Simulated picture of beamline before any modification (top) and the vertex position of tracks that pass through CLAS TOF detectors (bottom). The CLAS TOF is the big sphere on the right side of the figures. The photon beamline is at $y = 0$ where the two bright spots on the photon beamline at $z = 4000$ mm and 8000 mm corresponds to the collimator and the photon blocker. The hall floor lies at $y = -6000$ mm. The major sources of background along the tagger beamline are the tagger vacuum box exit shown by circles and the tagger beam dump. See text for details.

magnetic field. As a result they pass through a circular arc inside the tagger magnet and get dumped into a shielded beam dump below the floor of the experimental hall. The electrons that radiate photons have a wide range of energies and are bent more by the tagger magnetic field. As a result they can hit any material along the tagger beamline. The interactions of these electrons can create all kind of particles that can fly in any directions and hit various components in the hall and generate backgrounds that can reach the CLAS detectors.

We simulated the tagger beamline in detail by adding as many components as possible. The simulated picture of the tagger is shown in Fig. 45 (left). The vertex position, the location where a particle is created, of the tracks that pass through the TOF detector is shown in Fig. 45 (right). This shows that the major source of background is the area of the tagger vacuum box exit. We found that this part of the tagger has a large amount of unnecessary mass as shown in Fig. 42. This result is consistent with the earlier test run results (Fig. 41).

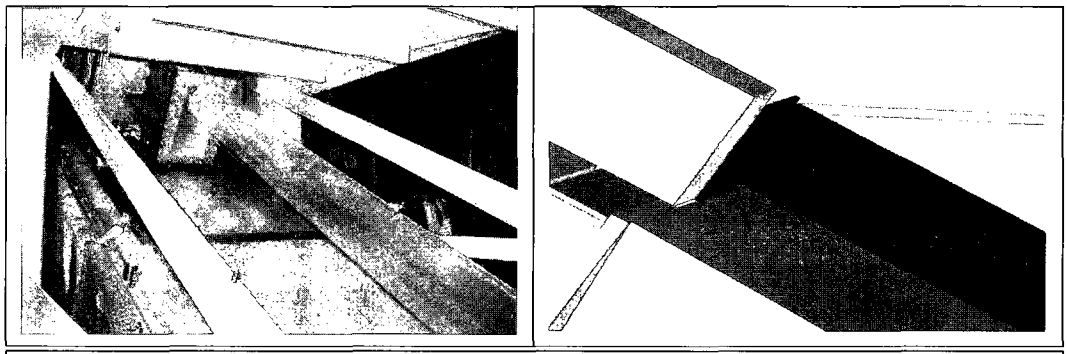

Tagger vacuum box exit area, left: photograph, right: simulated Picture.

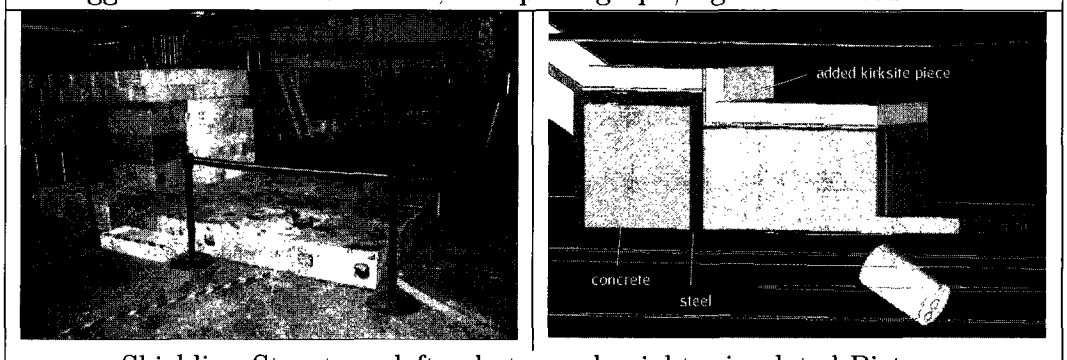

Shielding Structure, left: photograph, right: simulated Picture

FIG. 46: Top: the exit of the tagger vacuum box after modification. The beam pipe is replaced by a helium bag and other unnecessary materials are removed. Bottom: photograph of the shielding structure designed to shield remaining backgrounds coming from the tagger exit, floor and the beam dump.

In order to reduce the backgrounds produced in this area many possible options were simulated and the one that gave us the best result was used for the 2006 test run. We removed all the unnecessary materials and flanges in the tagger vacuum box exit area. The vacuum pump and the beampipe were replaced by a helium bag that can go all the way to the tagger dump (see Fig. 46 (top)). This reduced backgrounds generated in this area by about a factor of 4 compared to the existing tagger beamline. To control the backgrounds due to unavoidable sources we added mass shielding wherever necessary. We added the giant concrete blocks on the floor just above the tagger dump to stop any backgrounds coming from the tagger dump area. A complicated shielding structure as shown in Fig. 46 (bottom) made up of several materials was designed and placed around the tagger vacuum box exit area. The additional shielding gave us a factor of 5 more reduction in the backgrounds. So we finally got a factor of 20 background reduction coming from the tagger beamline. All of these changes in the tagger beamline were implemented in the October 2006 test run.

IV.3.2 Photon Beamline

The key components in the photon beamline are the radiator, photon collimator, convertor, chicane magnets, photon blocker, downstream collimator and condenser ring and cooler pipe and coil. These beamline pieces were added very carefully one at a time and their functionality as well as contribution to the background were studied in detail. They were optimized by trying various shapes and sizes. To control background we designed several shielding possiblities and used the one that gave us the better signal to background ratio.

In most of the cases only the TOF was used to find the background sources and to measure the background rate qualitatively. The background was the number of leptons depositing energy greater then 1 MeV in a scintillator detector. The signal is the number of high energy leptons in the beam at the target. The background ratio was the ratio of the number of scintillator hits to the number of the beam leptons. This was calculated for various simulated configurations. The vertex (origin of a particle track) of particles passing through TOF was used to locate the area of major background concern.

A very early simulated picture of the photon beamline is shown in Fig. 47 (top). It consists of a very thin gold foil radiator (5% radiation length), a very thin gold

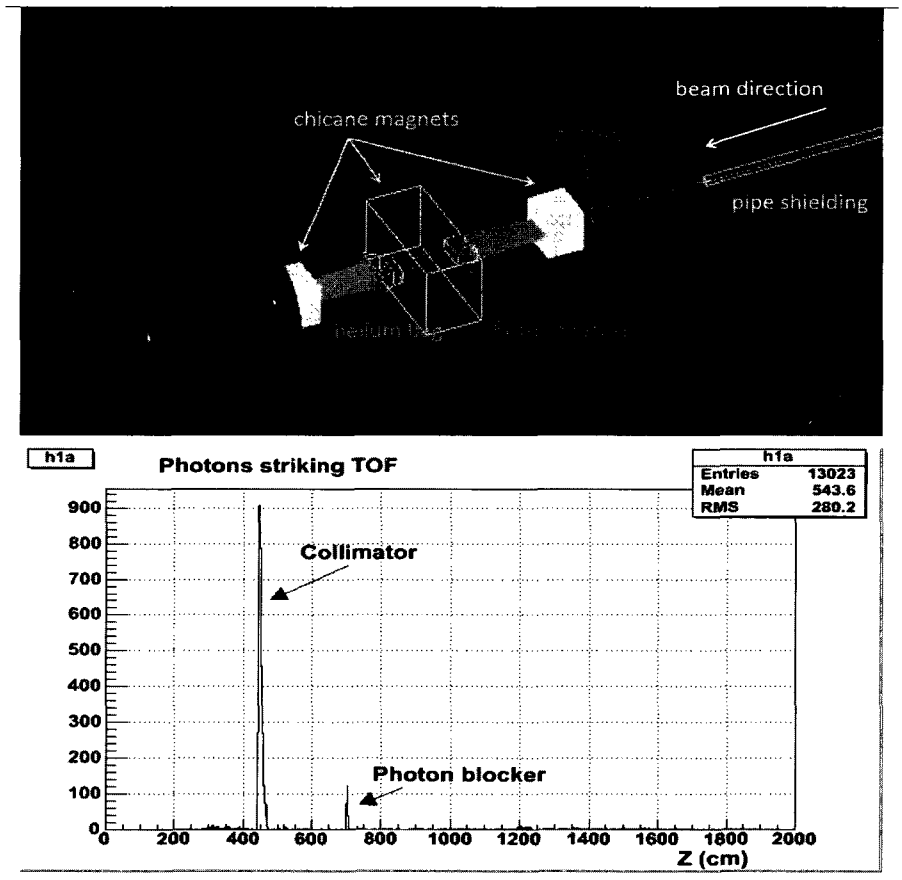

FIG. 47: Simulated photon beamline (top) and the production vertex of background source for the TOF detector (bottom). See text for details.

foil convertor (2% radiation length), a 30 cm long 2.8 mm inner diameter (ID) nickel collimator, chicane magnets, a 4 cm wide, 20 cm high, 50 cm long photon blocker placed just at the upstream end of pair spectrometer magnet (PS) aperture, a circular lead shield and snout collimator placed downstream of the third dipole magnet (ID2) and a vacuum pipe connecting the gap between the tagger yoke and the nickel collimator. The space between these components is filled with vacuum and helium as necessary. The remaining space in the experimental hall is filled with air. The origin of backgrounds for the above setup is shown in Fig. 47 (bottom). This shows that the beamline related background is dominated by the collimator and the photon blocker.

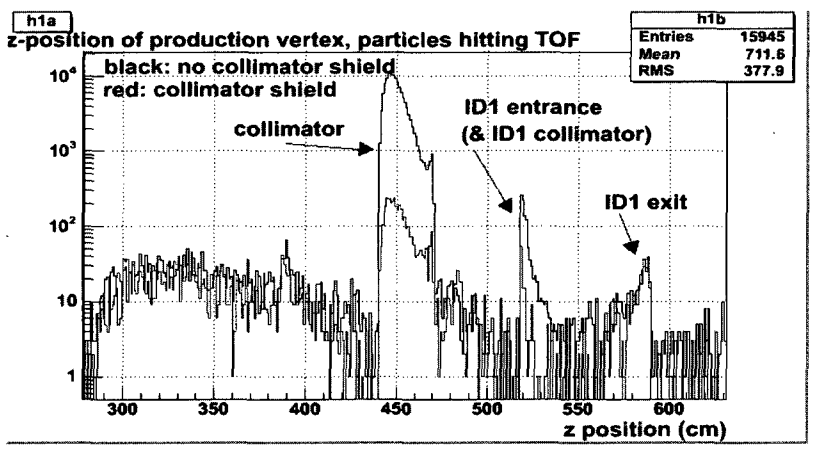

FIG. 48: Production vertex of particles hitting TOF sphere, with (lower counts) and without (higher counts) collimator shield.

A cylindrical lead shield around the collimator reduced the collimator background by 50%. The vertex plot with and without the collimator shielding is shown in Fig. 48. In this plot we can see the other small background sources in the photon beamline as well, such as the pipe between the tagger yoke and the collimator. Many collimator shielding options were tried, varying geometrical shapes, sizes, positions and materials. The result suggested that a very large wall just downstream of the collimator gives the largest background reduction. Similarly, many configurations of the snout collimator were simulated and the result was similar to the collimator shielding; the larger the outer radius of the shield, the greater the background reduction. This study also found that the backgrounds were not very sensitive to the length of cylindrical pipe portion of the snout collimator.

The study was repeated with a larger collimator ID (8.6 mm). Fig. 49 (top)

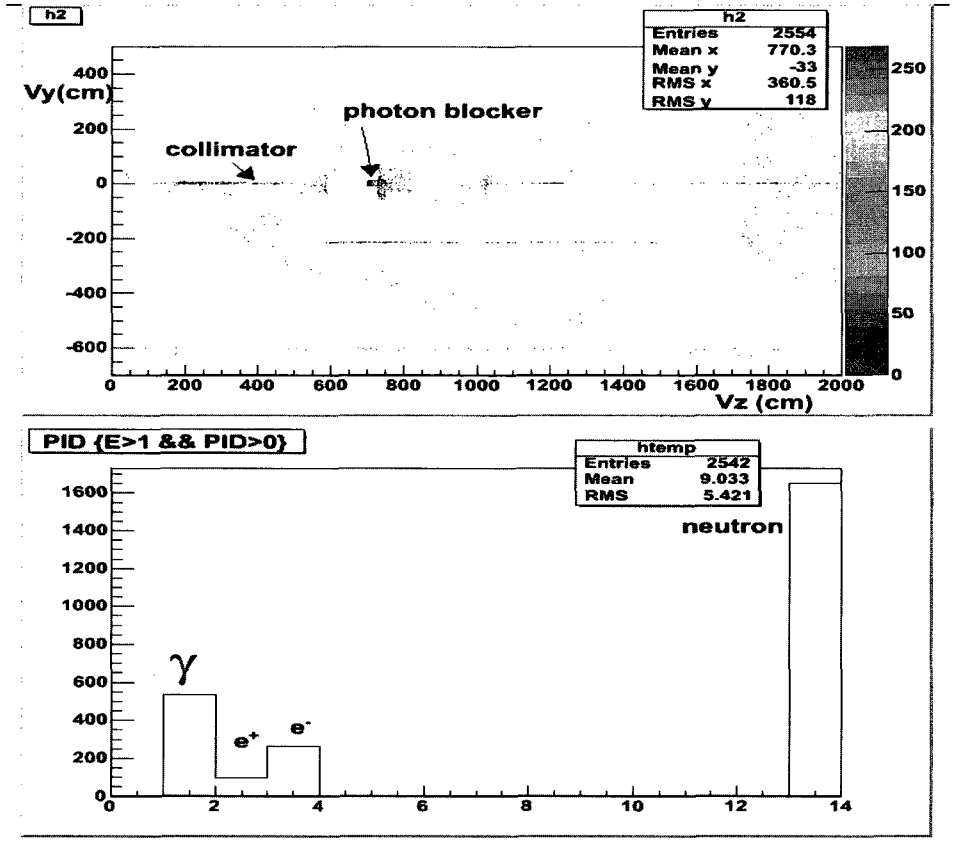

FIG. 49: Production vertex (top) and particles type (bottom) of all $E > 1$ MeV particles using 8.6 mm upstream photon collimator, snout collimator and no extra shielding in the photon collimator area.

shows the vertex y versus z of particles depositing more than 1 MeV on at least one TOF paddle. The background due to the collimator looks smaller than that of the photon blocker in this plot compared to earlier case shown in Fig. 47 (bottom). This could be due to the use of the larger ID collimator where more of the photon beam passes through the collimator without hitting it. The types of particles are shown in the particle identification plot in Fig. 49 (bottom). All the available collimators were simulated and we found that the one with the largest aperture (12.7 mm) gives the lowest background. Simulation also indicated that the background is lowest when no collimator is used. It indicates that the majority of the background is due to photons and neutrons produced at the collimator and the blocker respectively. The charged particle background is very small compared to the neutrals.

In order to estimate the neutron contribution to the TOF background the simulation was repeated with hadron physics processes switched off. The result showed that more than 50% of the TOF background is due to neutrons. Different positions of the blocker inside the pair spectrometer (PS) magnet were simulated but the result did not favor the blocker position far upstream inside PS. Different lengths and materials (lead and tungsten) of the blocker were also simulated but this did not make much difference in the backgrounds.

In order to shield the neutron backgrounds in the photon beamline several shielding configurations were designed and simulated. Two very large lead and Borated-Polyethylene (BPE) walls as shown in Fig. 50 (left) were placed just downstream of the second Italian Dipole (ID) magnet and the number of neutrons depositing energy greater than 1 MeV on TOF paddles was recorded. The result did not show a large background reduction compared to the previous snout shielding. Reversing the lead and BPE combination was also tried and this gave the same result.

Another beamline shield was designed and simulated. BPE chicane shielding was added, connecting the Italian dipoles (IDs) to the PS. The chicane shielding was hollow and rectangular in cross-section. The inner dimensions were chosen to match the larger of the two magnet apertures. The shield was 15 cm thick. Fig. 50 (right) shows both chicane shields. These reduced the neutron background by 30% and the photon background by 40%. This shielding was found to be insuficient during the 2006 test run and was replaced by a lead brick, concrete block and BPE chicane shielding. The details of this shielding will be described later in this chapter.

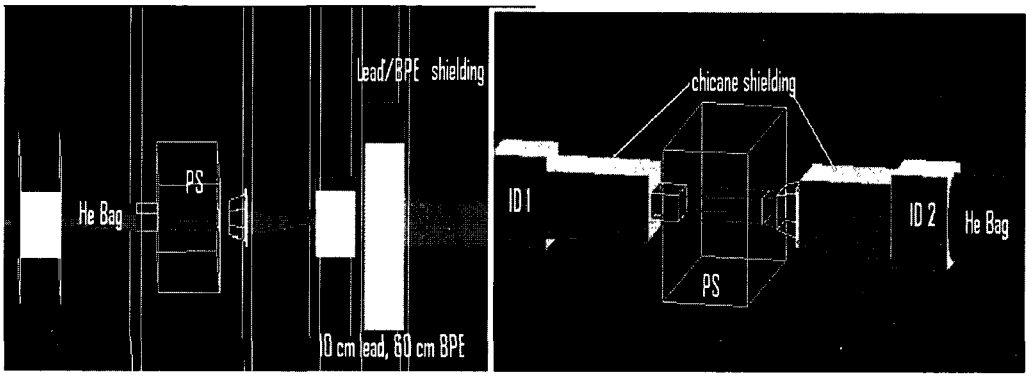

FIG. 50: Lead/Borated-Polyethylene shielding (left) and shielding between chicane magnets (right).

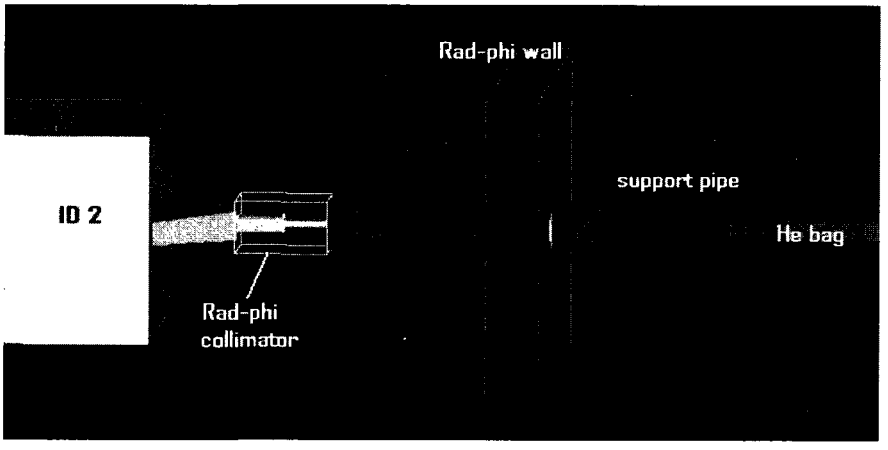

FIG. 51: Rad-phi wall, support pipe and Rad-phi collimator placed downstream of the second Italian Dipole magnet.

In order to shield the background generated upstream, the snout shielding described earlier was replaced by the Rad-phi wall. The Rad-phi wall (4 inch thick, 40 inch high and 40 inch wide lead wall with steel cladding) was placed in the beamline. This wall is supported by a support pipe (34 inch long, 6.69 inch OD and 4.2 inch ID) as shown in Fig. 51. A collimator (20 cm long) with outer diameter equal to the inner diameter of the support pipe was placed inside the support pipe and the inner diameter of the collimator was varied to optimize the background reduction. It was found that larger apertures allow more low energy backgrounds but very small apertures stop some of the good leptons as well. We found that the collimator with inner diameter 3 cm give the best signal to background ratio. Note that we reduced the ID of Rad-phi collimator to 2 cm in the 2006 test run.

Several other options for the collimator were also tried. The cylindrical collimator was replaced by two 10 cm long rectangular blocks of lead placed one upstream and the other downstream of the Rad-phi wall. The apertures of both the blocks were varied. The one with equal aperture of 3 cm ID gave the best signal to background ratio and was found consistent with the previous collimator. Finally this collimator was placed just downstream of the ID2 magnet (see green wire frame in Fig. 51) and the simulation was repeated as above, the result was found consistent with the earlier results.

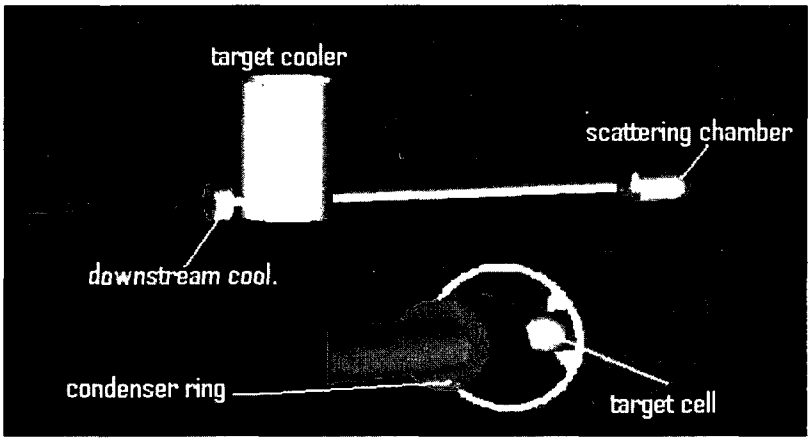

FIG. 52: GEANT4 picture of downstream collimator, condenser, target cooler, target cell, and scattering chamber.

The final beam collimation before the target region was done using a downstream collimator. The downstream collimator is a lead collimator made up of two concentric cylinders. The outer cylinder has inner and outer diameters of 10.5 cm and 30 cm

respectively. The inner cylinder has inner and outer diameters of 4.1 cm (6.0 cm in the 2006 test run) and 10.5 cm respectively.

The condenser ring is made of copper with dimensions 7 cm ID, 15 cm OD and 8.2 cm long. The downstream collimator, condenser, scattering chamber, target cooler and target cell are shown in Fig. 52. The combination of the 4.1 cm downstream collimator and the condenser removed the low energy part of the lepton beam and reduced the horizontal beam spread at the target as shown in Fig. 53. However, particles striking the condenser caused a very large background rate in DC region 1.

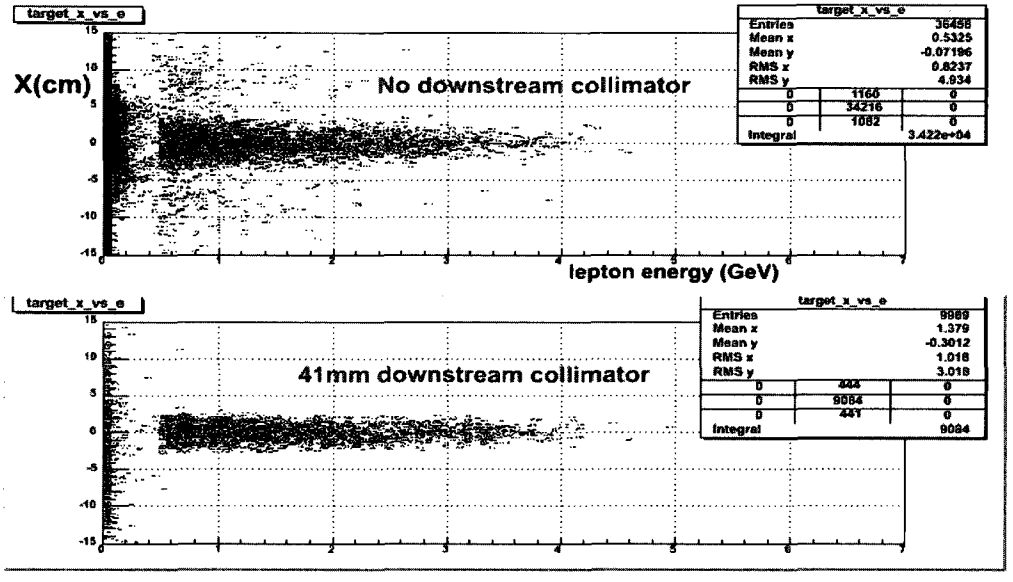

FIG. 53: x vs. energy distribution of leptons at the target plane without (top) and with (bottom) the downstream collimator for 5 GeV beam energy. The beamline has the 12.7 mm aperture photon collimator, Rad-phi wall and support pipe but no Rad-phi collimator or condenser.

IV.3.3 Target Area

The target region was also simulated to study the target related backgrounds. The important beamline components in the target region were added into the simulation. The vertex y vs. z of particles passing through DC R1 are plotted in Fig. 54. This shows that the condenser ring, scattering chamber, exit window, foam and air downstream of the target are the main sources of backgrounds. These backgrounds are primarily due to low energy Moller electrons.

Several shielding configurations were simulated prior to the test run to control

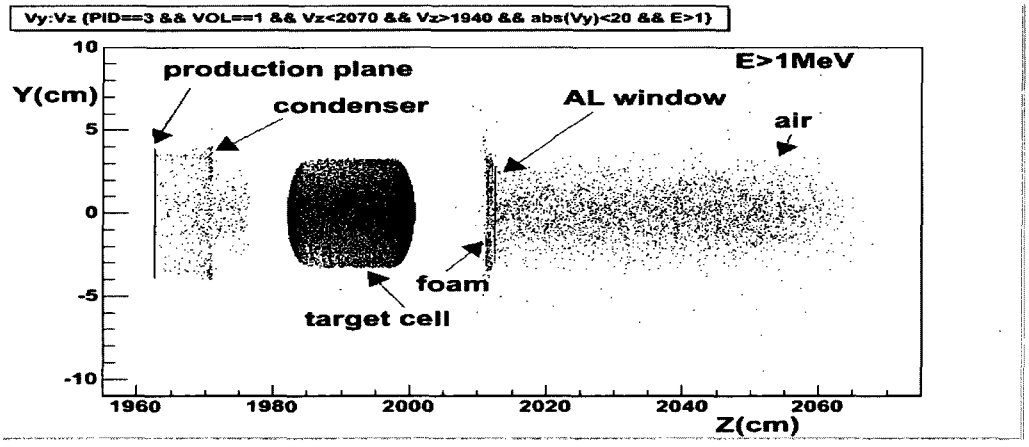

FIG. 54: The production vertex (y vs. z) for electrons passing through the DC R1 mother volume showing the background sources of low energy Moller electrons in the target area without using any shielding in this area.

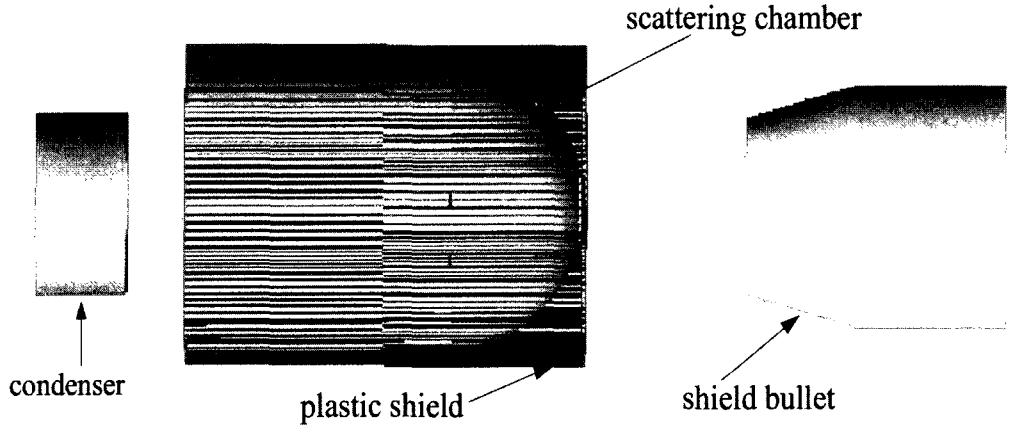

FIG. 55: Simulated picture of condenser, scattering chamber, plastic shield and the lead bullet shield. The plastic and lead bullet shields are intended to suppress Moller backgrounds.

these background sources. A plastic shield and a bullet shaped lead shielding (R1 shield) as shown in Fig. 55 were found to be very effective to shield these backgrounds. The effect of this shielding on the energy spectrum of electrons passing through region 1 drift chambers is shown in Fig. 56.

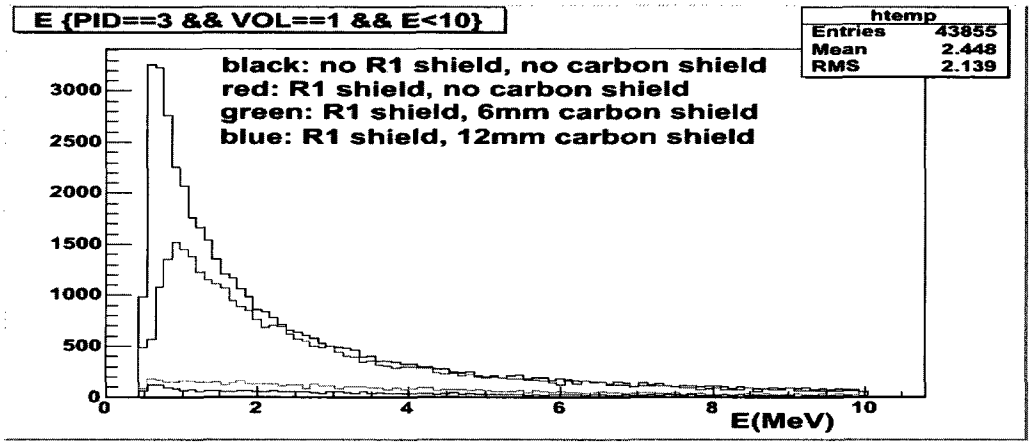

FIG. 56: The energy distribution of electrons in the target area before and after shielding. It clearly shows the effect of the R1 shield and plastic shield on the low energy Moller electrons that pass through the DC R1 mother volume. The black, red, green and blue correspond to highest to lowest counts respectively.

In the 2006 test run the bullet shield was mounted 14 inch downstream of the target cell. The aperture of the bullet had an angular clearance of 15° for the particles exiting the target cell. The cylindrical plastic shield over the scattering chamber was also constructed using two different thicknesses. One half of the plastic shield thickness was 0.8 cm and the other half was 1.2 cm. The effect of this shielding was not visible during the test run because it was implemented very early in the test run and at that time the R1 occupancy was dominated by backgrounds generated upstream of the target area. This was removed very early and could not be replaced later due to technical issues during the later part of the test run.

IV.4 MODIFICATION DURING TEST RUN

The test run was conducted in October 2006 to test the design of the electron-positron beamline. Most of the improvements in the beamline design found through simulation and earlier test runs were implemented in the 2006 test run beamline. We had developed the tagger beamline part of the simulation in detail but the photon

beamline and detectors were not developed fully. During the test run the luminosity (product of beam current, radiator thickness and convertor thickness) was very closely monitored and was found to be limited by the region 1 drift chamber occupancy. Several measurements were done by changing the beamline configuration to identify the background sources along the beamline and to shield them in order to reduce the region 1 occupancy. Some of the modifications during the test run that gave significant background reduction are described below.

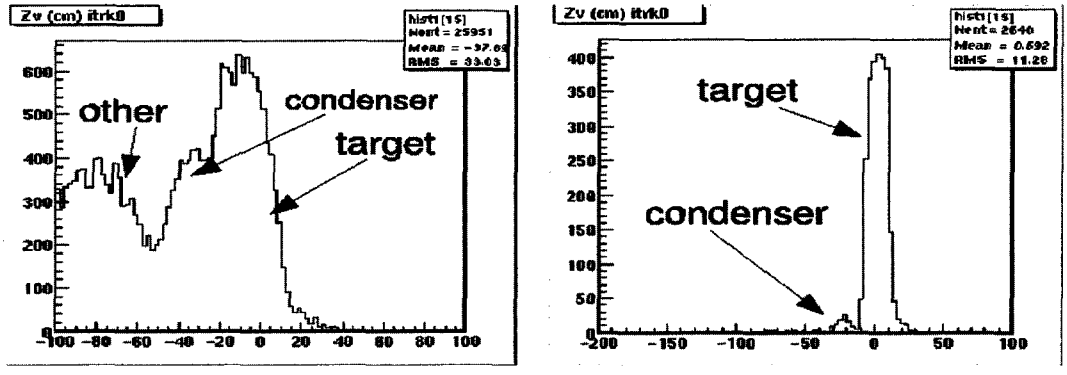

FIG. 57: Production vertex of tracks reconstructed using the fast online reconstruction algorithm. The result of the 3 cm collimator placed upstream of Rad-phi wall (left) and the 2 cm collimator (right). Note the reduction in the condenser and other backgrounds.

Reducing the inner diameter of the collimator just upstream of the Rad-phi wall from 3 cm to 2 cm significantly reduced the region 1 background. The vertex position of tracks measured by the fast online reconstruction for 3 cm and 2 cm diameter collimators is shown in Fig. 57.

The concrete blocks were stacked on the bottom of the torus cryoring in order to block the backgrounds in sectors 5 and 6 of the R1 drift chambers. This shielding reduced the sectors 5 and 6 occupancy in DC region 1 by about 30%.

Another major modification that helped reduce backgrounds was the addition of a clean up collimator downstream of the Rad-phi wall and a large concrete wall on the insertion cart. Addition of this shielding reduced the R1 DC occupancy by about a factor of two. The shielding location in the official engineering drawing and simulated 2006 test run configuration is shown in Fig. 58.

The Rad-phi collimator aperture was temporarily blocked by stacking lead bricks to check the background rate on DC region 1. The region 1 occupancy decreased from about 2.5% to 0.2% after blocking the Rad-phi wall. This also reduced the

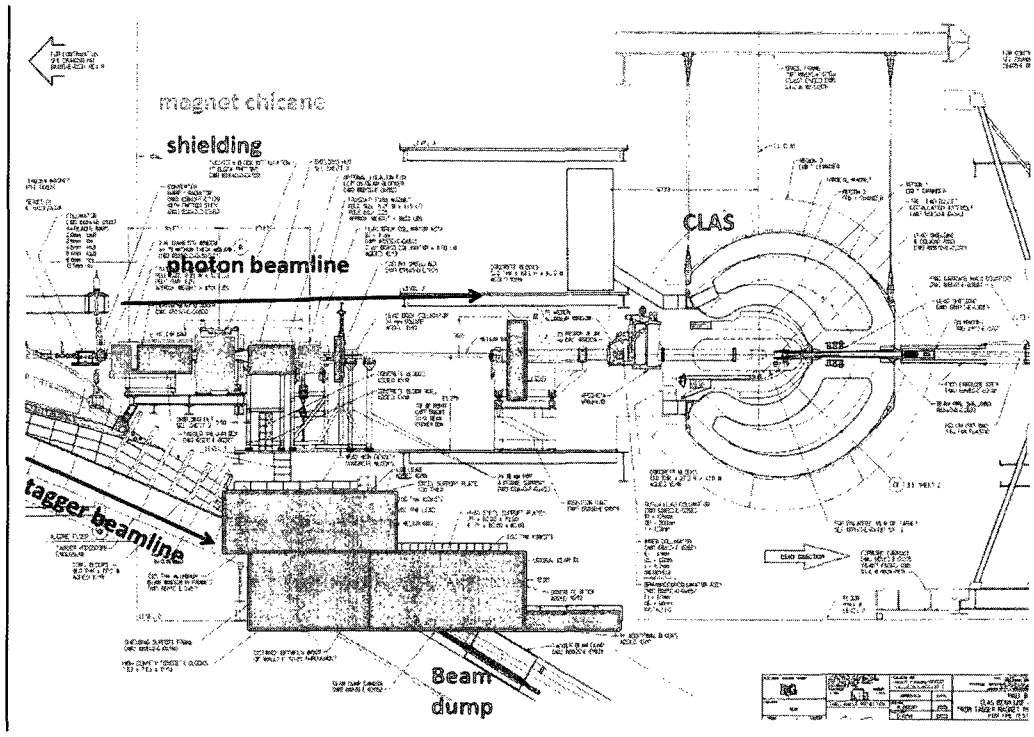

TPE Beamline: Geant4

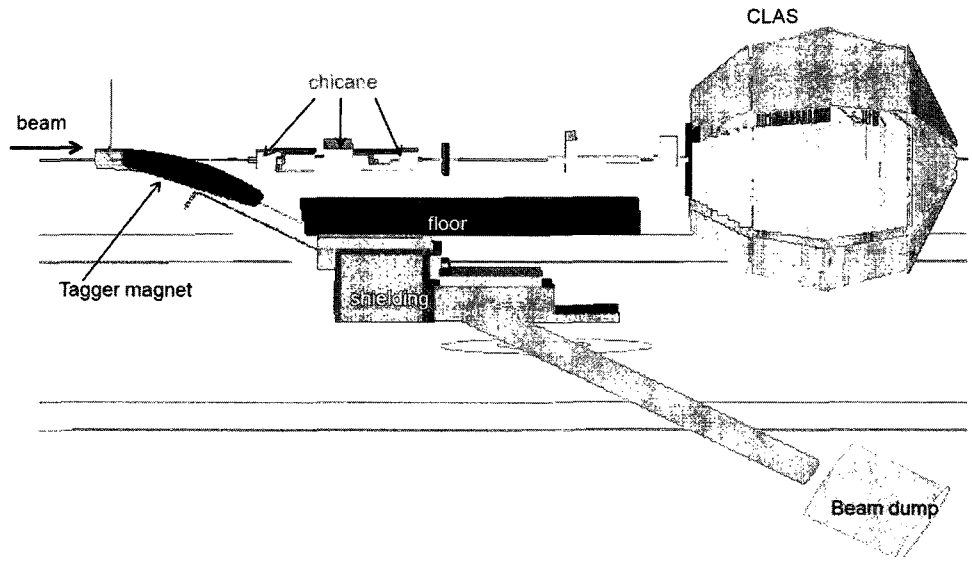

FIG. 58: The beamline and shielding configuration at the end of the 2006 engineering test run. Top: location of various shielding in the official engineering drawing, bottom: simulated picture of the beamline design.

trigger rate from 600 Hz to 200 Hz.

After implementing all of the above mentioned modifications, the R1 occupancy was measured with empty target and was found to be 20% less than the full target occupancy. This indicates that 80% of the R1 occupancy was not related to the target and was therefore due to interactions of the lepton beams with the beamline components and other sources.

These test run results were also used to validate the simulation after the test run. This is described in the next section.

IV.5 2006 TEST RUN AND SIMULATION COMPARISON

The detailed simulation of the experimental setup was done before the October 2006 test run. In this test run all the improvements in the beamline design found through simulation were implemented. During the test run some extra shielding was added and some was modified. Data was collected with various combinations of shielding and beamline components such as radiator, convertor and collimator.

We used the test run data to validate the simulation. We upgraded the simulation to match the test run configuration. We simulated several configurations similar to that of the test run to compare the results.

IV.5.1 Upgrading the simulation

In order to upgrade the simulation to match the test run, I added the following components to the simulation:

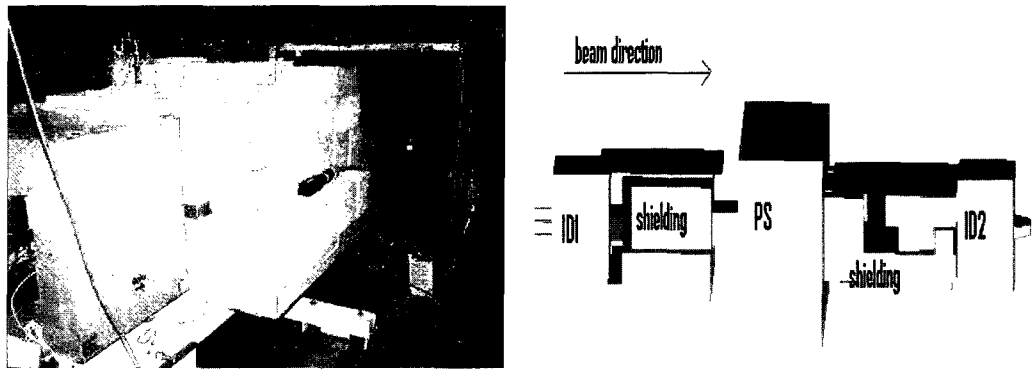

FIG. 59: Shielding between the chicane magnets. Left: photograph of the shielding between ID1 and PS. Right: simulated picture of shielding between chicane magnets.

Chicane Shielding

Prior to the test run we simulated shielding made of borated polyethylene (BPE) as shown in Fig. 50 (right) in the gaps between the Italian Dipoles (IDs) and the Pair Spectrometer (PS). In the test run this shielding was remade using lead bricks, concrete blocks and BPE to fill all the gaps possible as shown in Fig. 59 (left). The simulated picture of the test run shielding is shown in Fig. 59 (right).

Cryoring and Wall

The cryoring which is a part of the CLAS detector was not simulated prior to the test run. We placed a concrete wall on the cryoring during the later part of the test run to test whether it helps to shield sectors 5 and 6 of the region one drift chambers. These two components were added to the simulation which is shown in Fig. 60 (top).

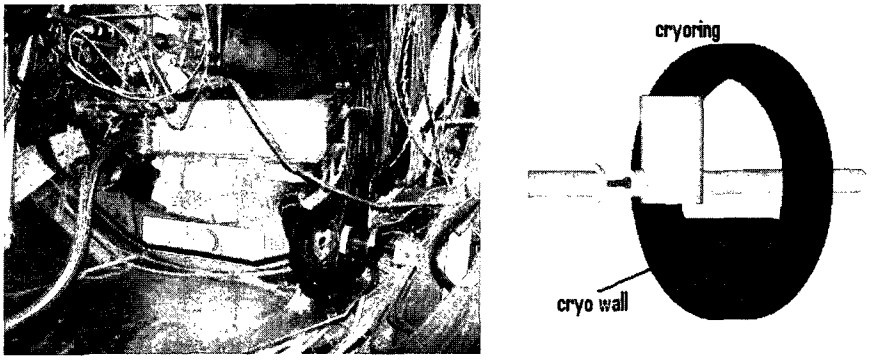

FIG. 60: Top: cryo ring and cryo wall, bottom: very upstream vacuum pipe and tagger magnet yoke before and after additional iron.

Addition of Vacuum and Beam Pipe

In the earlier version of the simulation there was a 200 cm air gap between the radiator and the tagger magnet. In reality this was vacuum. Electrons traveling through this air created large amounts of background in the DC region 3 and TOF detectors. This area of the beamline was covered with a vacuum pipe as shown in Fig. 60 (bottom). Note that this is not a background reduction that helps our luminosity. It only makes our beamline simulation more realistic. Addition of this pipe reduced the number of particles passing through the DC R3 mother volume as shown in Fig. 61. The DC R3 mother volume is a geometrical shape made up of segments of spheres which contains the DC R3 wires (daughter volumes).

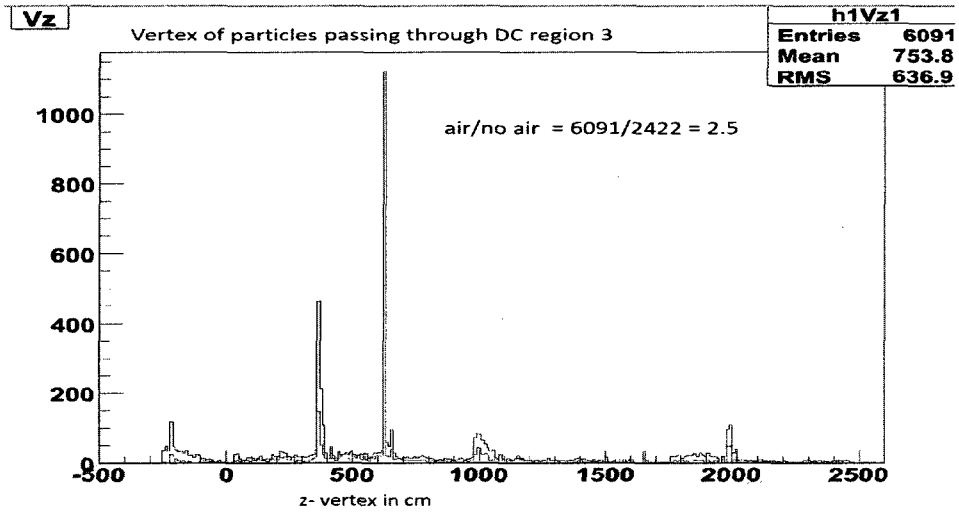

FIG. 61: z-vertex position of particles passing through the DC R3 mother volume before (higher counts) and after (lower counts) removing the air between the radiator and the upstream end of the tagger magnet.

Modifying the Tagger Magnet Iron

We upgraded the tagger magnet geometry to match the CLAS tagger magnet. The tagger magnetic field volume was not covered by the magnet iron (see Fig. 60 (bottom left)) as it should be. So we added extra iron at the upstream end of the tagger magnet to cover the magnetic field (see Fig. 60 (bottom right)). Addition of the extra iron made the tagger yoke more realistic and also blocked the line of sight for some of the upstream backgrounds as done by the real tagger magnet.

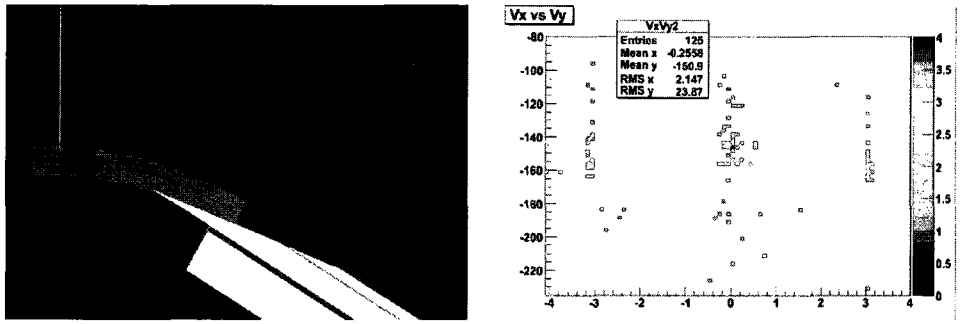

old tagger vacuum box and vertex x vs. y of charge particles passing through DC region 3

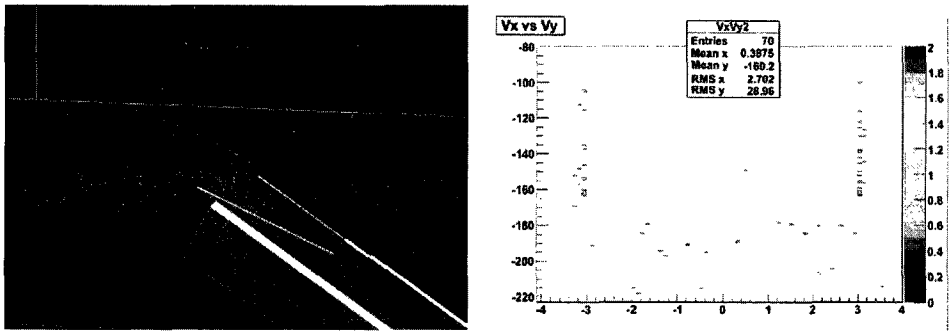

new tagger vacuum box and vertex x vs. y of charge particles passing through DC region 3

FIG. 62: The tagger vacuum box modification and the effect of modification to reduce backgrounds generated in this area of the tagger beamline. The black region is filled with air.

Modifying the Tagger Vacuum Box

In the vertex plot of charged particles tracks passing through the DC region 3 and TOF we saw some hot spots in the tagger magnet exit area. There was some air in the tagger vacuum box. Removing this air reduced the background generated in this particlular area by 50%. The existing and modified tagger exit area as well as the effect of the modification are shown in Fig. 62. Note that the backgrounds coming from $x = 0$ disappear after removing the air from the tagger vacuum box. The backgrounds coming from $x = -3$ cm and $x = 3$ cm are due to the beam hitting the pole faces of the tagger. There is no way to reduce this background without adding some kind of mass shielding.

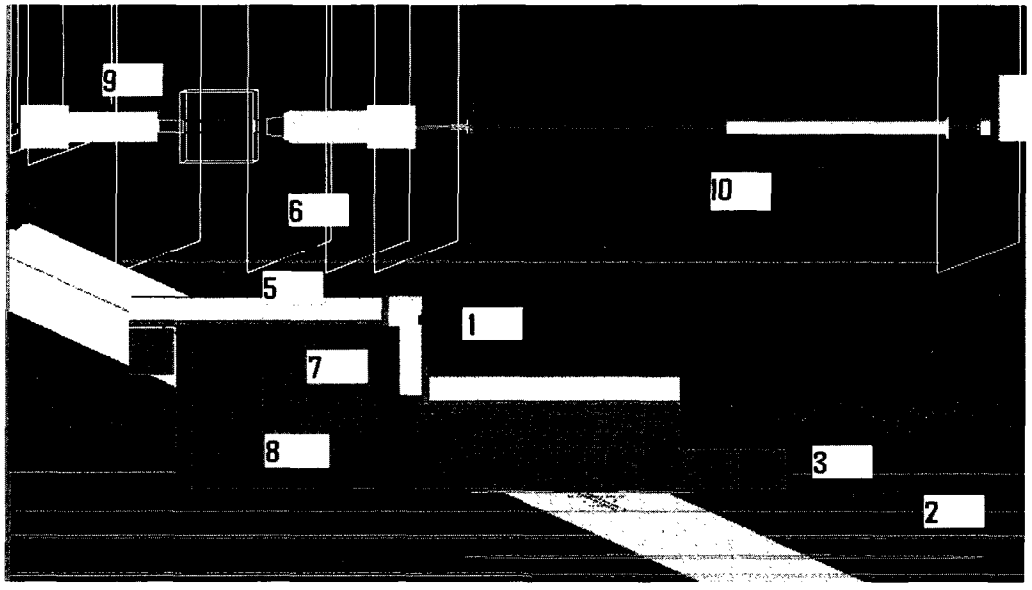

FIG. 63: The locations of scintillator counters placed in the hall during 2006 test run.

Scintillator Background Measurements

Two plastic scintillator detectors of size 4 cm × 4 cm × 8 cm were placed at different locations inside the hall to measure background rates during the test run. One scintillator was fixed at position number 10 whereas the other was moved to various locations labeled 1 through 9 in the hall as shown in Fig. 63. Position 4 is not visible in Fig. 63 because it lies on the center of the left wall of the shielding between ID1 and PS whereas position 9 is at the top of the shielding. Note that the scintillator can

be seen in position 4 in Fig. 59. Locations were chosen based on the possible major background sources. The data was very useful to see the effectiveness of shielding and to find further improvements. We added these scintillators into the simulation in order to compare to the test run results for validation. The comparison will be discussed later in this chapter.

Time of Flight Counters

In earlier versions of the simulation, the TOF was made up of two concentric spherical shells of steel and lead. From this we could get only the number of tracks that passed through this geometry or the origin of those tracks that deposited certain amounts of energy greater than the energy threshold (1 MeV). This was enough to find the primary background sources for the TOF detectors and to design shielding to reduce those backgrounds. But it could not give TOF rates for each sector or the energy deposited on individual scintillator paddles. We replaced the old TOF geometry by more realistic TOF counters as in CLAS. The position and orientation of the TOF scintillators was taken from the respective CLAS SC banks. The scintillator paddles for one sector are shown in Fig. 64. Scintillators were made sensitive detectors in order to get energy deposited information. The outer 1/8 inch steel and inner 5 mm lead sheets are also added into the simulation. It is now very similar to the CLAS TOF as in CLAS gsim. This is now capable of recording TOF rates and energy deposited in each scintillator paddle which we can compare with the test run data from the TOF counters.

Region 1 and 3 Drift Chambers

Before the test run we focused on reducing the rates in the TOF and maximizing the ratio of beam leptons on the target to hits in the TOF. This was only enough to study TOF related backgrounds. The test run showed that the limiting factor for the luminosity was the region one drift chambers. But the DC region 1 occupancy was not studied or well simulated in the earlier study. The drift chambers were implemented in the simulation as solid spherical segments filled with gas without any internal structure such as DC wires. This can give only the number of tracks passing through this volume or the origin of those tracks. We could not extract the DC occupancy using that information. A new DC geometry was implemented using the DC wire position, orientation and length of each wire as taken from the CLAS

DC package. The drift cells were made as a tube of DC gas with uniform radius of 6.6 mm around each wire for DC region 1 and 17.5 mm for DC region 3. This gives a uniform circular cell which approximates the hexagonal cell of the CLAS DC. Note that the wires themselves were not implemented. This makes our DC geometry more realistic but not exact. This is accurate enough for this kind of simulation. The DC mother volume, a large geometrical shape that encloses all the drift cells, and the wires for DC R1 and R3 are shown in Fig. 64. DC R2 is not simulated in detail because it is protected by the CLAS torus magnetic field and thus has much lower backgrounds.

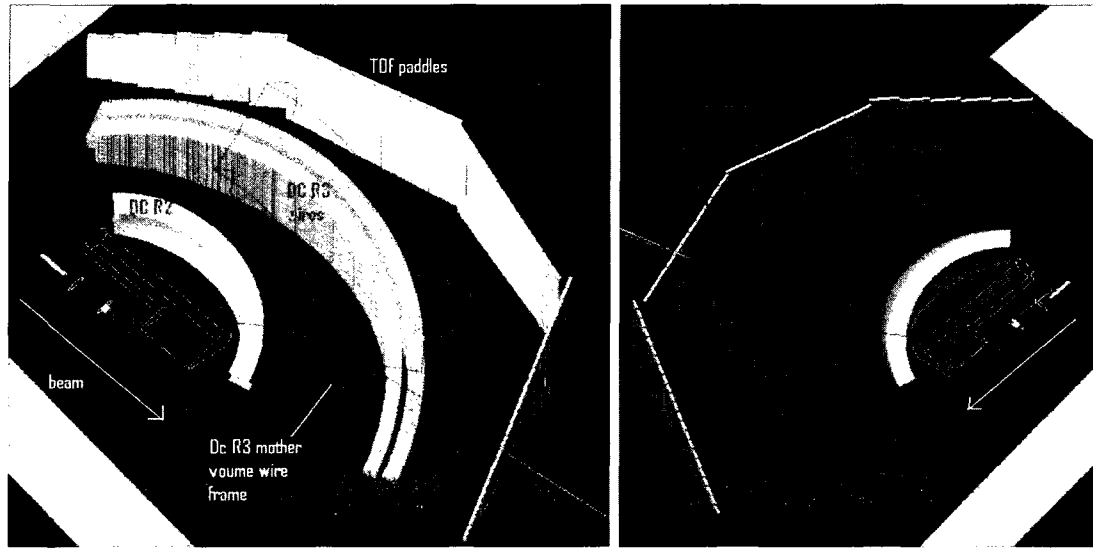

FIG. 64: Simulated picture of DC and TOF detectors for one of the sectors of CLAS. An electron track of momentum 500 MeV fired at an angle of 45o to the beamline for positive (left) and negative (right) torus polarity is also shown.

Torus Magnetic Fields

We added a torus magnetic field similar to the CLAS into the simulation. The reliability of the torus field was tested by generating an electron track at the center of the target and at some angle to the beamline. The electron was tracked with both positive and negative torus polarity and its path in the field was observed by the OpenGL visualization of GEANT4. An electron track of momentum 500 MeV at an angle of 45o to the beamline is shown in Fig. 64 (left) for positive torus polarity and Fig. 64 (right) for negative torus polarity. We found the bending of the simulated track in all the trials as expected for the CLAS torus field.

Still Not in the Simulation

It is not possible to simulate everything inside the experimental hall. We simulated most of the components that we think important and were likely sources of background. The electronic racks, cables and wires, and space frame floors are still not in the simulation. The tagger magnet geometry is not exactly the same as the real tagger. This may account for some of the differences between simulation and test run results for the background comparison.

IV.5.2 Validating the Simulation

We used the data collected in the October 2006 test run to compare with the simulation for validation. The DC occupancy for region 1 and 3 and the TOF rates were extracted from the data files using the CLAS Event Display (CED).

To compare the test run and simulation result for the DC and TOF we had to convert our simulated hits into DC occupancy and TOF rates. We converted the number of wires hit in the DC by the charged particles to the occupancy. In order to do this we need to convert the simulated number of events in terms of time equivalent to a particular beam current (40 nA). By knowing the number of wires hit in the particular time window (0.625 μsec for DC region 1, 2.4 μsec for DC region 3 and 100 nsec for TOF), the time equivalent to the simulated hits can be converted to the occupancy as

$$Occupancy(\%) = \frac{N_{hit} \times T_{detector}}{T_{events}} \frac{1}{N_{wire}} \times 100, \tag{36}$$

where N_{hit} is the total number of DC (region 1 or 3) wires hit, $T_{detector}$ is the detector (DC region 1 or 3) time window, T_{events} is the time equal to the simulated number of events for a particular beam current and N_{wire} is the total number of wires per sector for DC region 1 or 3. The same technique can be used to convert simulated TOF hits to TOF rates.

We had data for several configurations depending upon the different shielding and aperture of the various beamline components such as collimator, Rad-phi wall etc. We simulated the same configurations and determined the same quantity as in the test run. The configurations and the results of the comparison is described below.

Nominal

This configuration consists of ground floor shielding in the later part of the test run (24 concrete blocks on the floor above the tagger dump), the test run shielding in between chicane magnets, 2 cm inner diameter of the Rad-phi collimator, and 6 cm inner diameter of the downstream collimator.

Rad-Phi Blocked

This configuration is similar to the nominal except the Rad-phi collimator aperture was blocked. The lepton beam passing through the beamline is blocked by the Rad-phi so we should not see any occupancy in the region one drift chambers.

Cryowall

We added a concrete wall on the cryoring (see Fig. 60 (top)) during later part of the test run. The purpose of this was to shield the background coming from below the beamline which can be seen in sectors 5 and 6 of the region 1 drift chambers. Unfortunately we do not have the correct data set to check the effect of this test with the simulated data because it was done with combination of other changes and its effect only is not visible in the data.

Insertion Cart Wall

Some extra shielding such as the insertion cart wall, wall on top of the bunker, wall below the second tunnel, concrete wall on the cryoring and clean up collimator after Rad-phi wall were added to the nominal configuration to test all the possibilities to reduce background and hence to improve the luminosity.

Downstream Collimator Blocked

This configuration is similar to the insertion cart wall option but the aperture of the downstream collimator is blocked by using a lead brick. This stops the beam completely and whatever we see in the DC and TOF is the unwanted backgrounds that hurt our luminosity.

The comparison of test run and simulation result for the above mentioned configurations are shown in tables and graphs below for DCs R1, and R3 and TOF.

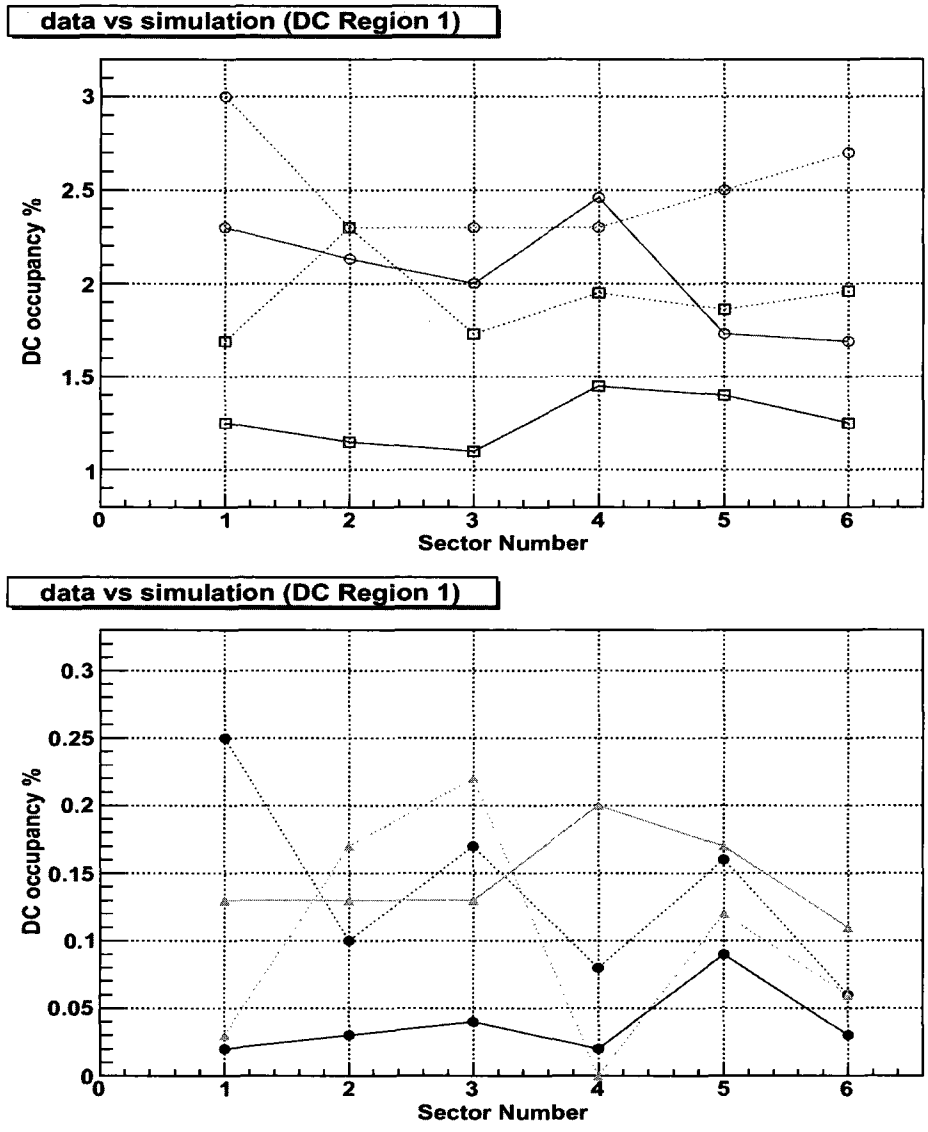

FIG. 65: DC R1 occupancy graph for various configuration indicated by different markers. Nominal, insertion cart wall, Rad-phi blocked and downstream collimator blocked configurations are shown by open circles, open squares, filled circles and filled triangles respectively. The plot of occupancy (%) vs. sector number for data and simulation are shown in solid and dotted line respectively.

TABLE 1: Region 1 DC occupancy

% occupancy R1 for each sector							
		sec1	sec2	sec3	sec4	sec5	sec6
Nominal	data:	2.3	2.13	2.0	2.46	1.73	1.69
	simulation:	3.0	2.3	2.3	2.3	2.5	2.7
Rad-Phi Blocked	data:	0.02	0.03	0.04	0.02	0.09	0.03
	simulation:	0.25	0.10	0.17	0.08	0.16	0.06
Icart Wall	data:	1.25	1.15	1.1	1.45	1.4	1.25
	simulation:	1.69	2.30	1.73	1.95	1.86	1.96
DS Coll. Blocked	data:	0.13	0.13	0.13	0.20	0.17	0.11
	simulation:	0.03	0.17	0.22	0.0	0.12	0.06

The measured and simulated results of four different experimental configurations for DC R1 are shown in Table 1 and also shown graphically in Fig. 65. Overall the simulated and test run results reasonably agree with each other. When we blocked the hole in the Rad-phi wall collimator and the downstream collimator, the occupancy dropped to almost zero for both the simulation and test run data. The Icartwall option reduced the occupancy by about 50% compared to the nominal option in both the simulated and test run results.

There is about a factor of three difference between the simulated and test run results for DC R3 occupancy and TOF rates. The measured and simulated results of four different experimental configurations for DC R3 and time of flight are shown in Tables 2 and 3 respectively. The same result is shown graphically in Fig. 66. This difference could be due to not including everything in the experimental hall into the simulation. Another possibility could be due to the incorrect choice of software time window while converting simulated DC wire hits into occupancy. Even though there is a large disagreement between the simulation and data for the R3 and TOF, a close observation revealed that the occupancy for R3 and rates for TOF decreased by about the same factor while going from nominal configuration to the Rad-phi blocked configuration for both the simulation and data as shown in Table 4. We also saw same trend of background reduction going from one configuration to the other in simulation as well as test run.

TABLE 2: Region 3 DC occupancy

% occupancy R3 for each sector							
Nominal		sec1	sec2	sec3	sec4	sec5	sec6
	data:	1.25	0.79	0.72	1.18	0.93	0.95
	simulation:	4.3	3.5	3.5	4.3	3.0	2.8
Rad-Phi Blocked	data:	0.36	0.32	0.30	0.44	0.78	0.75
	simulation:	1.57	2.58	1.68	1.78	2.43	1.76
Icart Wall	data:	0.35	0.25	0.25	0.45	0.5	0.45
	simulation:	2.19	3.6	2.97	1.93	2.68	1.93
DS Coll. Blocked	data:	0.29	0.21	0.25	0.38	0.48	0.42
	simulation:	1.77	2.26	2.43	2.19	1.13	1.27

TABLE 3: TOF average hits per sector per event.

TOF rates for each sector							
Nominal		sec1	sec2	sec3	sec4	sec5	sec6
	data:	1.81	2.02	0.96	1.60	1.42	1.01
	simulation:	0.30	0.43	0.51	0.33	0.29	0.24
Rad-Phi Blocked	data:	0.45	1.16	0.69	0.41	1.25	0.93
	simulation:	0.17	0.32	0.29	0.17	0.21	0.14
Icart Wall	data:	0.64	0.85	0.51	0.58	0.81	0.60
	simulation:	0.29	0.33	0.28	0.22	0.22	0.22
DS Coll. Blocked	data:	0.62	1.01	0.55	0.56	0.93	0.62
	simulation:	0.26	0.36	0.37	0.26	0.26	0.21

TABLE 4: Average DC occupancy and TOF rates.

Average DC (% occupancy) TOF (rates)				
Nominal		DC R1	DC R3	TOF
	data:	2.05	0.97	1.47
	simulation:	2.52	3.57	0.35
Rad-Phi Blocked	data:	0.04	0.49	0.82
	simulation:	0.14	1.97	0.22
Icart Wall	data:	1.27	0.38	0.67
	simulation:	1.92	2.55	0.26
DS Coll. Blocked	data:	0.15	0.34	0.72
	simulation:	0.10	1.84	0.29

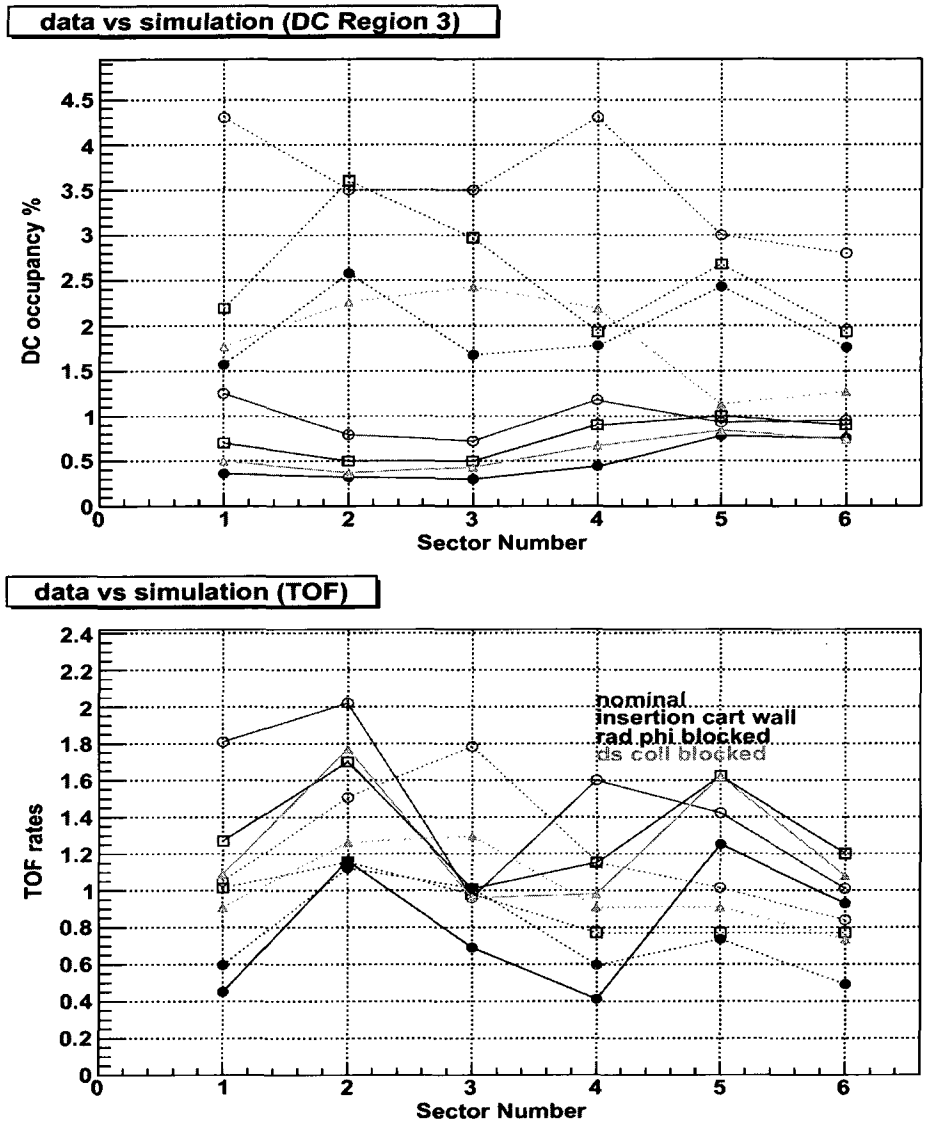

FIG. 66: Top: DC R3 occupancy graph for various configuration indicated by different markers. Nominal, insertion cart wall, Rad-phi blocked and downstream collimator blocked configurations are shown by open circles, open squares, filled circles and filled triangles respectively. The plot of occupancy (%) vs. sector number for data and simulation are shown in solid and dotted line respectively. Bottom: TOF rates for various configuration indicated by different markers same as DC R3. The plot of average hits per sector per event vs. sector number for data and simulation are shown in solid and dotted line respectively. Note that the simulated result is multiplied by a factor of 3.5 to make the result comparable.

TABLE 5: Scintillator count ratio comparison between simulated and test run results.

Position	Simulated ratio	Test Run ratio
1	0.6	0.3
2	0	0
3	0	0.2
4	42	1.0
5	1.8	0.1
6	4.6	8.4
7	6.2	6.6
8	6.8	7.3
9	11	1.0
10	1.0	1.0

Scintillator Count Ratio

The counts from scintillators placed at different locations in the halls as shown in Fig. 63 were recorded during the test run. The scintillators were simulated and the similar count rates were reproduced. The ratio of the number of counts of a scintillator at positions 1 through 9 to that of the scintillator at position 10 is calculated from the simulated counts and the test run data.

The result of the comparison is shown in Table 5. For most of the cases, the test run agrees qualitatively with the simulation. But for locations 4 and 9 scintillator simulation result is higher than the test run. Some of this is due to the fact that there was air in between the radiator and the tagger magnet iron in the simulation, which created a lot of background at those locations. This can be seen clearly by comparing Fig. 63 and Fig. 61. The scintillator positions 4 and 9 are located near the spike at $z = 600$ cm which corresponds to the photon blocker.

The data for scintillator position 5 looks unrealistic. Scintillator positions 5 and 6 were very close to each other but their counts differed by a factor of 84 implying that something is wrong with that data.

During the test run we also recorded the scintillator counts after blocking the Rad-phi collimator. This should reduce the counts in scintillator position 10 but not in position 6 so the ratio of scintillator position 6 to 10 must be larger than the unblocked case. These ratios for the test run and the simulation are found to be as

expected.

Full and Empty Target Occupancy

We collected data with empty and full target. The DC R1 occupancy for the full and empty target were 2.3% and 1.84% respectively. This result showed that 80% of the DC R1 occupancy was not target related. Our simulated result for the similar configuration showed that 88% of the DC occupancy was not related to the target. This is a good agreement for this kind of simulation.

We could reproduce most of the observed facts found in the test run through our simulation. The simulation and the test run results are found to be in good agreement from our detail comparison as discussed above. So we use this simulation tool to find further background sources, design shielding and optimize the luminosity for the final experimental preparation.

IV.6 SIMULATION FOR THE FINAL EXPERIMENT PREPARATION

We achieved 4% of the proposal luminosity in October 2006 test run. Our luminosity was limited by the drift chamber occupancy. After the test run we continued our simulation efforts. After finding reasonable agreement between the simulation and the test run for the same beamline configurations, we selected the best test run result and then started working for further improvements in the beamline design. Our projected background rates for a given configuration are the ratio of the measured to simulated test run occupancies times the simulated occupancy for that configuration. So any error in the simulation should be the same for all the simulated results and should cancel in the comparison.

We used vertex plots of particles passing through a specific mother volume as a guiding tool to find the sources of backgrounds for the detector corresponding to that mother volume. The vertex origin of tracks are analyzed before and after any modification to the experimental configuration to find the improvement of one configuration over the other. The quantitative result of background reduction or luminosity increase is estimated by finding the differences between the DC occupancy for the simulated test run and any trial option.

To find the background sources that cause the drift chamber occupancies and

limit the luminosity, we studied R1 DC and R3 DC separately. The major sources of R1 and R3 related backgrounds were identified and controlled by designing suitable shielding. Some of the existing beamline elements were also modified in order to optimize the signal to background ratio as well as the beam spot size at the target. The detailed studies of R1 and R3 related backgrounds are described in the following sub-sections. Since TOF and DC R3 background sources are very similar we did not study the TOF in detail.

IV.6.1 DC R1 Backgrounds

There are two main remaining sources of R1 backgrounds that were not completely identified and taken care of during the engineering test run.

Small Aperture Beamline Components

Due to the large beam size, some of the beam hit the beamline components such as the condenser and heat exchanger. This resulted in a large number of background particles hitting the R1 DC. The shoulder upstream of the target in the online reconstruction plot as shown in Fig. 57 is due to scattering from the condenser.

The background due to the small aperture of the beamline components can be reduced by enlarging the apertures of the condenser and heat exchanger pipe. Increasing these apertures by 25% can reduce the R1 backgrounds by a factor of two. However, this option is expensive and time consuming. So we tried another option.

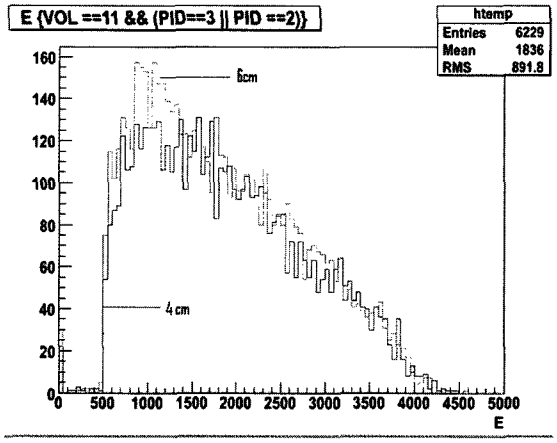

FIG. 67: The energy distribution of leptons at the center of the downstream collimator using 6 cm and 4 cm apertures.

As a second option we reduced the aperture of the downstream collimator from 6 cm to 4 cm so that the collimated beam does not hit the existing condenser and heat exchanger pipe. This reduced the R1 background by a factor of four but loses 10% of the low energy part of the beam as shown in Fig. 67. Losing 10% of the low energy part of the beam does not affect our physics goal. Therefore we chose this option.

Moller Electrons in the Target Region

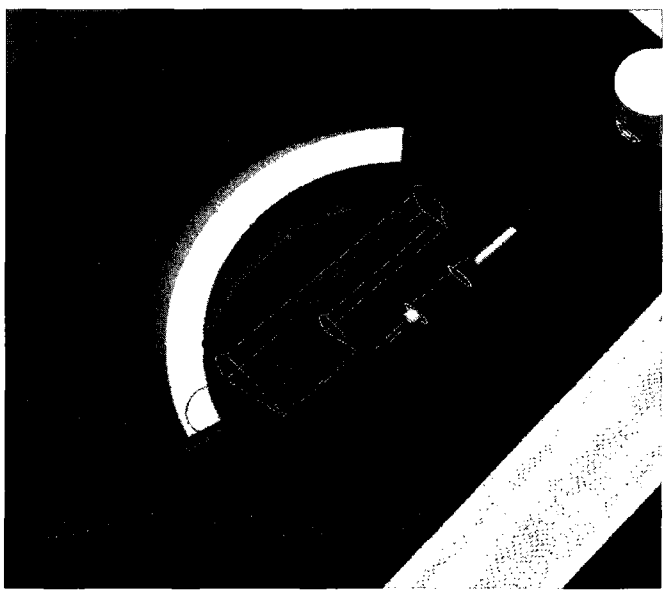

FIG. 68: Simulated picture of an electron track affected by the tagger magnetic field. The track is originated at the target and bend by the tagger magnetic field back to the DC R1 giving multipe hits by a signle track.

The test run data as well as the simulation showed that the low energy charged particle tracks originating in DC R1 got reflected by the torus magnetic field and traveled back to the DC R1 giving multiple hits from the same track. This phenomena is shown in Fig. 68 where a simulated electron track of 100 MeV fired at an angle of 10° reflects back from the torus field and hits R1 again. The simulated hits for R1 with the torus field is found to be 2.5 times higher than without the torus field.

There are some ways to reduce this kind of background. We simulated several options such as mass shielding downstream of the target along with a carbon shield to cover the scattering chamber (see Fig. 55), magnetic shielding, and both mass and magnetic shielding. Mass shielding was used in the test run but its effect was

not visible due to large backgrounds from other sources. When we reduced the background sufficiently in the later part of the test run, this shielding was already removed. So we do not have any reliable data from the test run to check the effect of mass shielding. Our simulation showed about a 25% background reduction from this shielding by stopping low energy electrons in the target region.

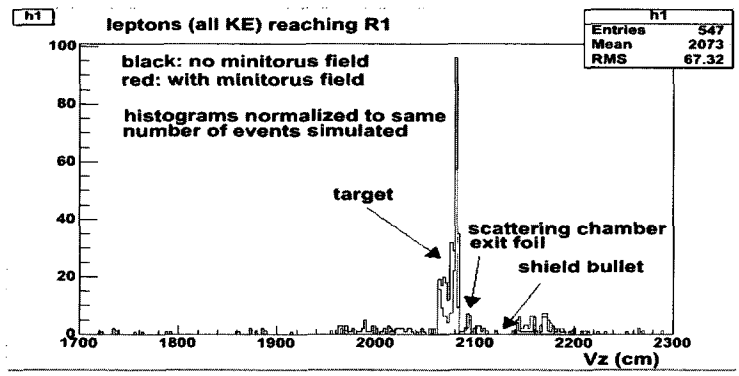

FIG. 69: Vertex z of particles passing through DC R1 mother volume before (higher counts) and after (lower counts) minitorus and mass shielding.

In order to test the effect of magnetic shielding in reducing DC R1 backgrounds, we added a simple solenoid field around the target. This reduced the DC R1 occupancy by 40%. So we tried the actual CLAS minitorus magnetic field, but without its physical magnet coils. The minitorus field along with the mass shielding described above gave a factor of more than two reduction in the background. The effect of this combination of shielding is shown in Fig. 69 where the vertex z of leptons passing through DC R1 is shown. But in reality we needed to add the materials of the physical minitorus magnet. Adding the physical minitorus increased the background by a factor of five because of its small beam aperture. Several other options with minitorus and mass shielding in the area downstream of the target were tried and the one with minitorus and mass shielding as shown in Fig. 70 was found to be the most effective. This gave a factor of 3.4 background reduction for the DC R1. Fig. 71 (left) and Fig. 71 (right) show the electron tracks before and after the shielding described above.

The above study showed the importance of the minitorus in reducing R1 backgrounds. The challenge was to design the minitorus so it does not add to the background. The existing minitorus aperture is the main problem because of the large beam size. A close observation of the minitorus revealed that its aperture is 3.0 cm

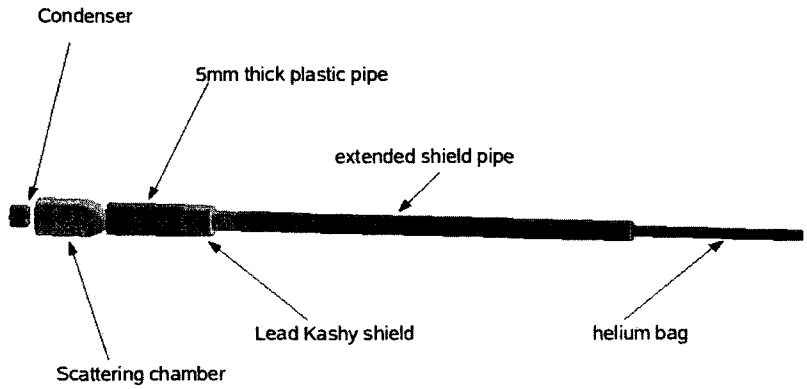

FIG. 70: Mass shielding designed to shield low energy electron in the target region.

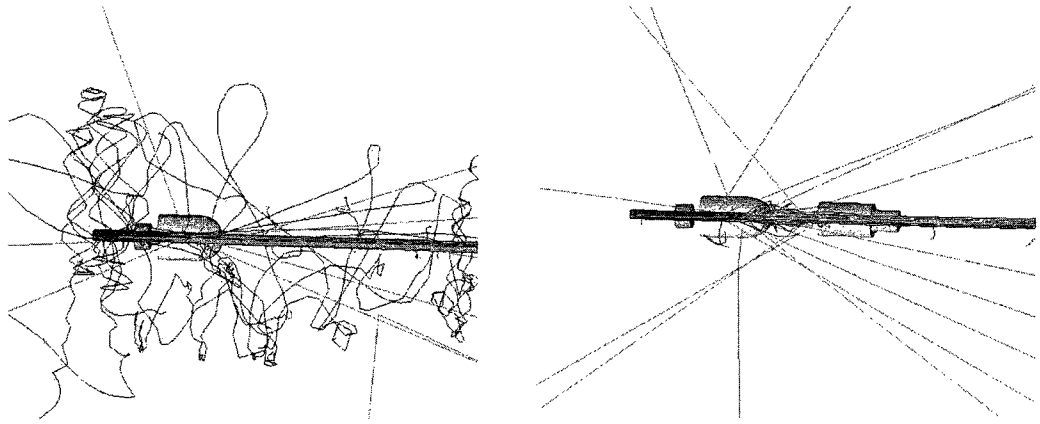

FIG. 71: Left: particles track at the target region before magnetic and mass shielding. The neutral particle tracks are straight, electron tracks are bent by the magnetic field in random directions. Right: with magnetic and mass shielding.

and can be enlarged to 5.5 cm by removing the inner lead layer of shielding. The engineering drawing of the existing minitorus is shown in Fig. 72. The 4 cm ID downstream collimator is reasonably well-matched to the minitorus aperture. The simulation has shown that we need at least a 5.5 cm aperture in the minitorus with the use of 4 cm ID downstream collimator and existing condenser and heat exchanger pipe.

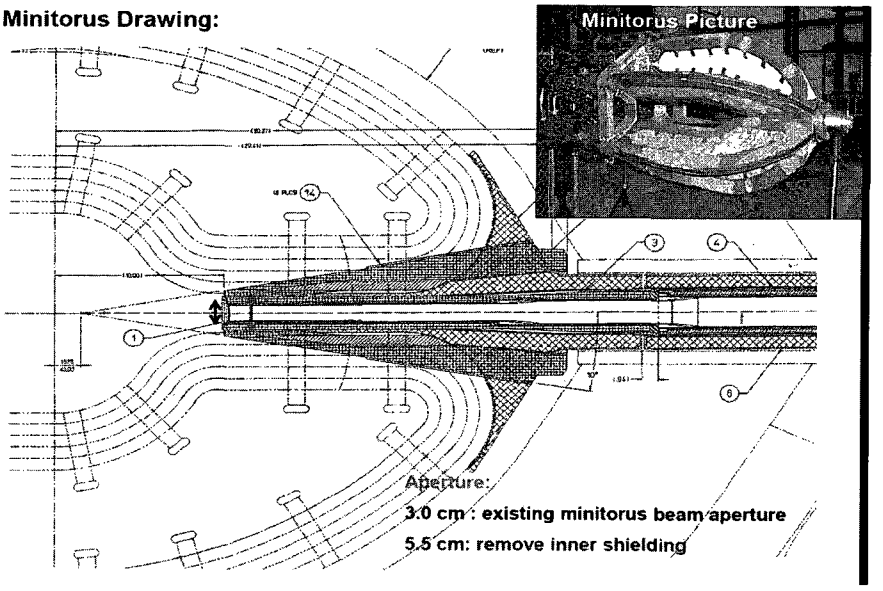

FIG. 72: Engineering drawing of the minitorus.

Another important modification is to optimize the Moller electron mass shielding shown in Fig. 70. This shielding is not compatible with the physical minitorus and does not give an angular acceptance of 20° for a track coming out of the target.

The new Moller mass shield is a combination of cone and cylinder made of tungsten as shown in red in Fig. 73. It has an inner diameter of 8 cm. We need 22 cm separation between the target end point and the mass shielding to provide 20° angular acceptance for particles coming out of the target. To achieve this we moved the 30 cm long target by 31.6 cm upstream from the CLAS nominal target position. The new shielding catches the Moller electrons and also stops the widely spread tail of the beam. The lead cone shown in blue in Fig. 73 is a part of the minitorus. Its inner diameter (5.5 cm) is the limiting aperture. This also works as a blocker for the beam wider than its aperture.

We simulated the three run configurations and compared the result with the test run configuration to find the improvement factor. The simulated configurations are

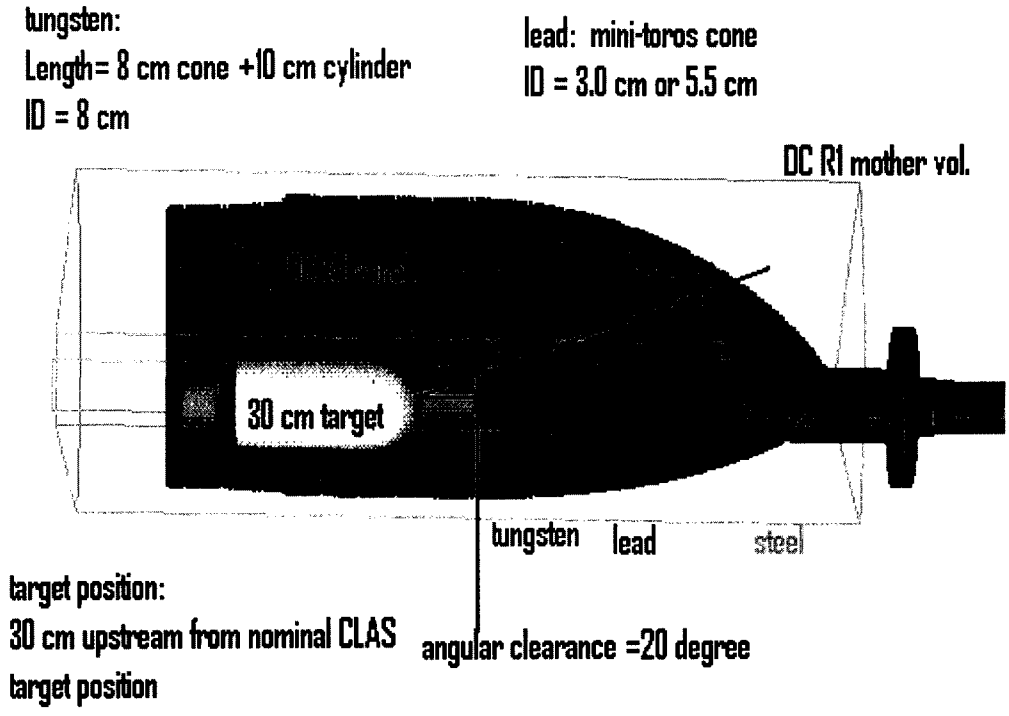

FIG. 73: Target area with DC R1 mother volume, wires, condenser, target and mass shielding.

TABLE 6: Simulation result for test run, option 1 and option 2 scaled by the target length.

Configurations:	% occupancy R1	% occupancy R3
Test Run:	2.20	2.0
Option 1:	0.37	0.58
Option 2:	0.24	0.56

described below:

- Test run: Beam energy = 3.2 GeV, Target Length = 18cm, Downstream Collimator ID = 6cm, no Mini-torus, no Moller Catcher, no Lead Covering on Vacuum Box and no Concrete Disc

- Option 1: beam energy = 5.5 GeV, Target Length = 30cm, Downstream Collimator ID = 4cm, Mini-torus with 3 cm aperture, Moller Catcher, Lead Covering on Vacuum Box and Concrete Disc (see section IV.6.2 for a discussion of the lead covering and concrete disc).
  Note: Occupancy shown in table is scaled by the target length.

- Option 2: Beam energy = 5.5 GeV, Target Length = 30cm, Downstream Collimator ID = 4cm, Mini-torus with 5.5 cm aperture, Moller Catcher, Lead Covering on Vacuum Box and Concrete Disc.
  Note: Occupancy shown in table is scaled by the target length.

Table 6 shows the simulated test run and the latest improved configuration results. The 5.5 cm minitorus clearance is significantly better than the 3 cm clearance. Comparison of the test run with the improved run with 5.5 cm minitorus clearance gives us a factor of about 10 background reduction for R1 DC.

The effect of magnetic and mass shielding on suppressing Moller backgrounds is shown in Fig. 74 and Fig. 75.

IV.6.2 DC R3 Backgrounds

We studied the remaining sources of DC R3 background after the test run in detail. The R3 background is found to be dominated by various upstream and tagger

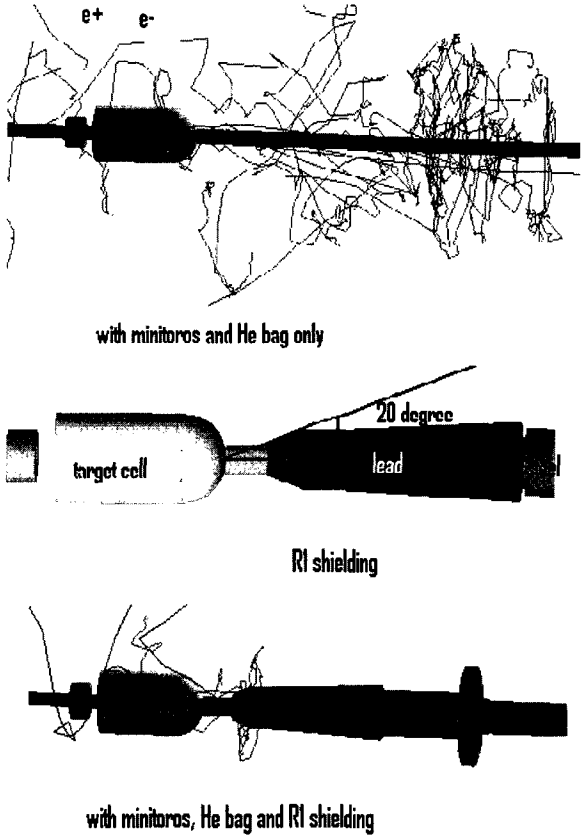

FIG. 74: DC region 1 with magnetic and mass shielding. The top picture shows the tracks of electrons and positrons with only the minitorus field and a He bag downstream of the target. The middle picture shows the R1 shielding that catches Moller electrons and the bottom picture shows the electron and positron tracks with the improved shielding.

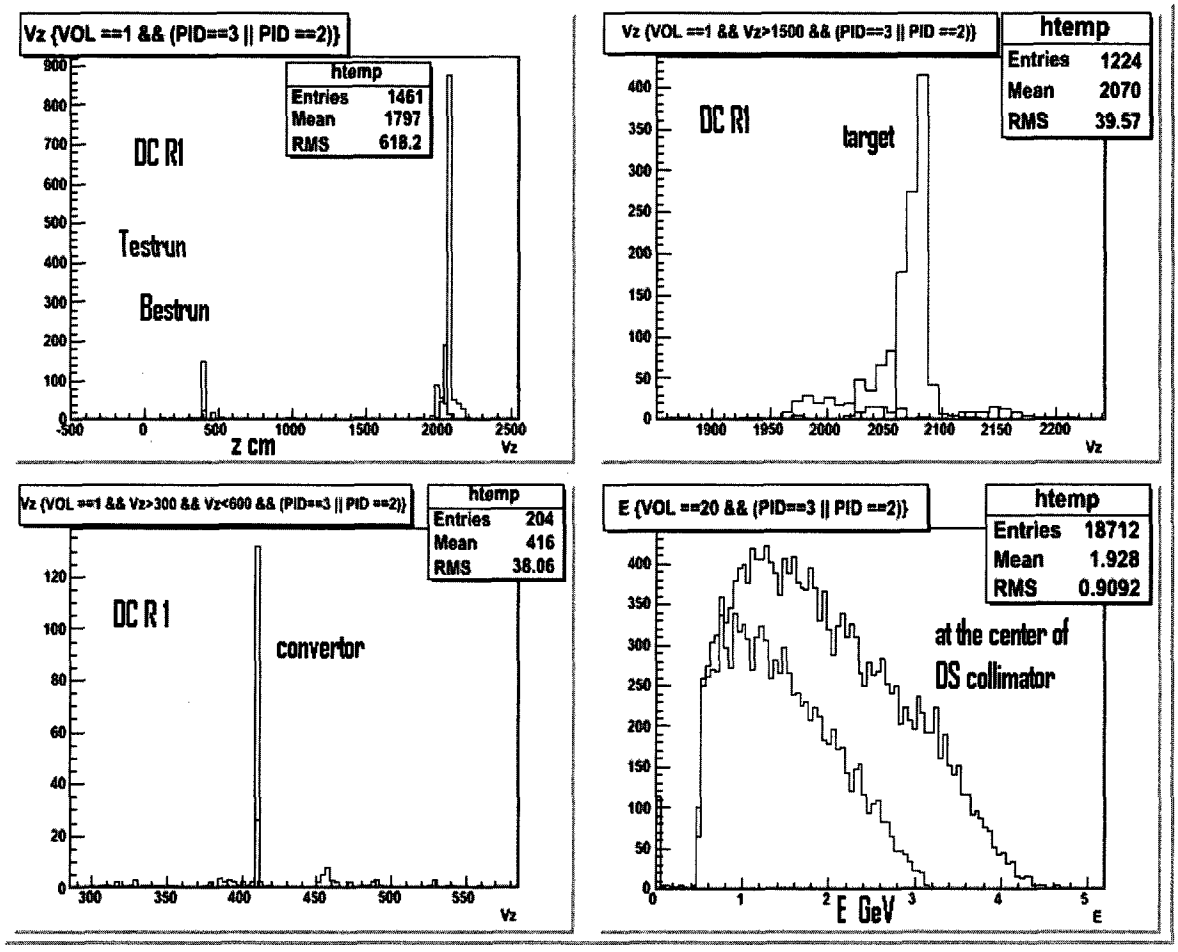

FIG. 75: Vertex z of charged particles passing through DC Region 1 mother volume for the test run (higher counts) and option 2 (lower counts) configurations. The top left, top right and bottom left plots show the production vertices of all, target area and convertor area charged particles respectively. The bottom right plot shows the energy distribution of the charged particles at the center of the downstream collimator. Note that the test run and option two beam energies were 3.2 and 5.0 GeV respectively.

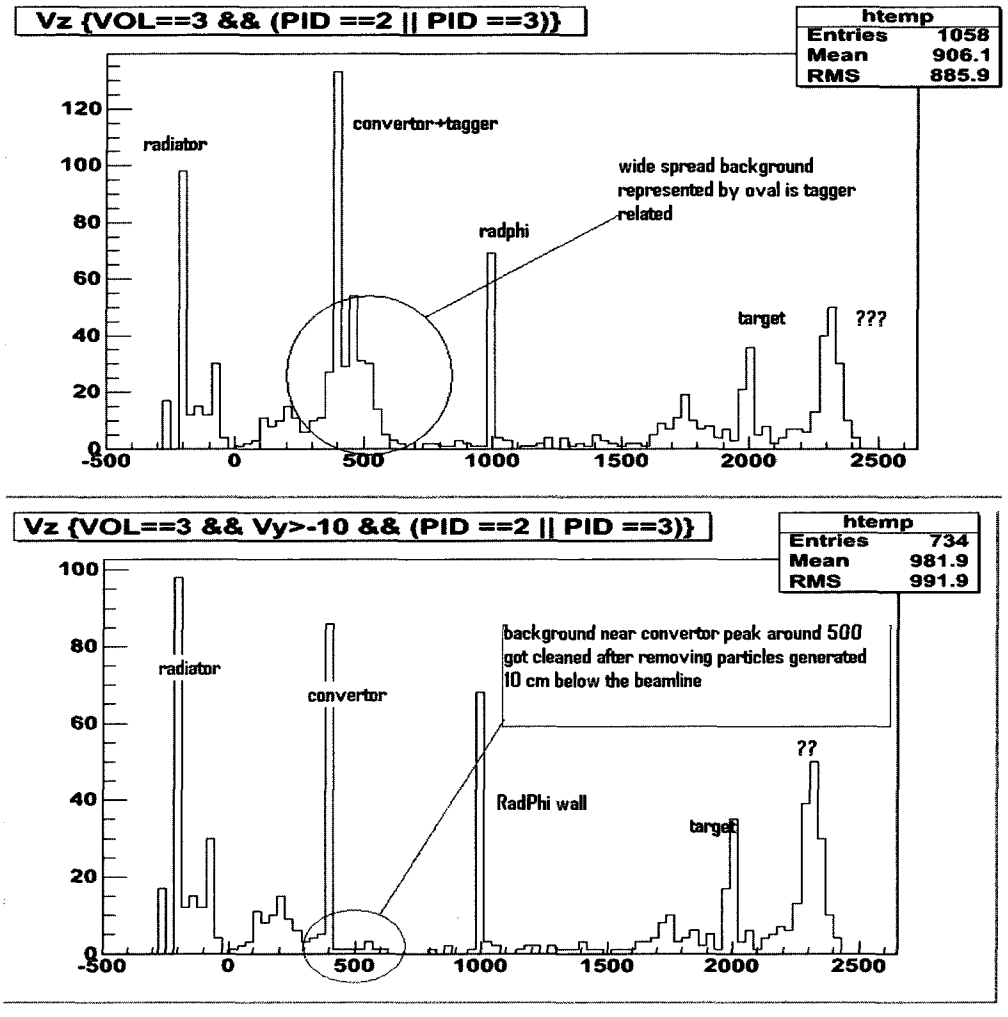

FIG. 76: Top: vertex z of all the particles passing through the DC R3 mother volume. Bottom: vertex z of particles passing through the DC R3 excluding particles coming from 10 cm below the beamline.

beamline related sources as shown in Fig. 76. The simulation shows a significant amount of background coming from the electron beam exiting the tagger magnet. This wide background around the peak at $x = 500$ cm in the vertex plot shown in Fig. 76 (top) is due to particles generated by interactions at the tagger magnet exit area and the peak corresponds to the convertor. Fig. 76 (bottom) shows the vertex plot of particles excluding all the particles generated more than 10 cm below the photon beamline. Thus it represents only the photon beamline related source of DC R3 background. The difference is the tagger vacuum box contribution. The best way to shield backgrounds is to put shielding closest to the source or closest to the detector. Due to physical constraints present in the Hall we decided to shield in two places.

Covering the Tagger Vacuum Box

We put a lead covering over the tagger vacuum box to catch particles generated in this area. Several lead thicknesses are simulated. We found that 0.25 inch of lead is sufficient and physically possible to use as shielding in this area of the tagger.

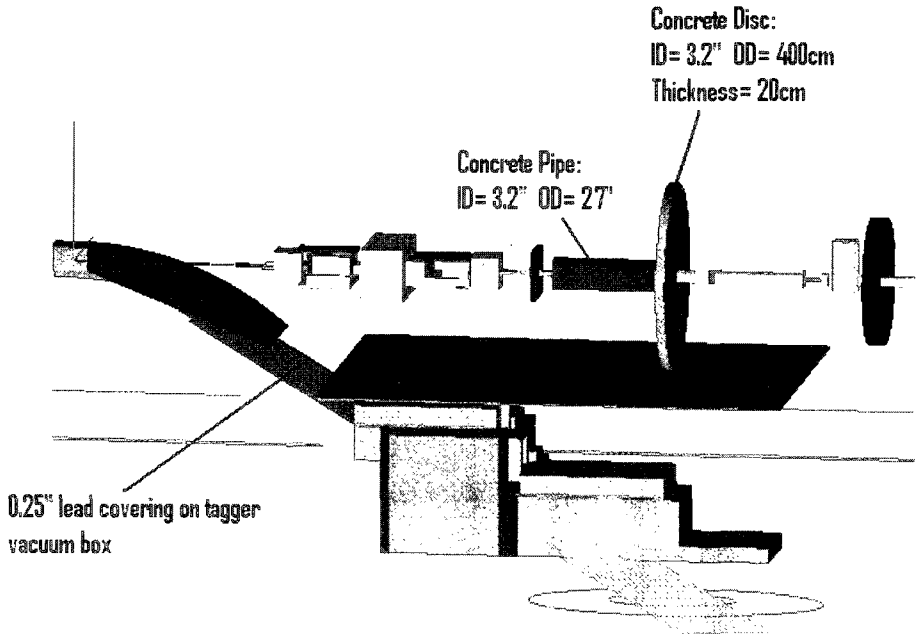

FIG. 77: DC R3 shielding: Concrete disc, concrete pipe and lead covering on the tagger vacuum box.

TABLE 7: Simulation result for DC R3 test run and improved beamline configurations.

Configurations:	% occupancy R3
Test run	1.98
Improved	0.49

Mass Shielding Upstream of CLAS

As the outer detector of CLAS, the DC R3 is highly affected by backgrounds generated anywhere in the experimental hall, especially in the upstream part of the beamline and tagger. We improved the tagger beamline before the test run as described above, but it is still a significant source of background for DC R3 as shown in Fig. 76. Some of the sources are known and shielded if possible. In order to take care of unknown sources and sources that are impossible to shield directly we decided to put a large mass shielding upstream of CLAS. To begin with, a huge steel disk was placed at the location of the downstream collimator. We found that a one inch thick steel disk of diameter 8 m can reduce the R3 background by a factor of two. This shielding was found impossible to implement. So we modified this shielding to make it almost as effective and physically possible. A one foot thick concrete disk of diameter 4 m was placed at the upstream end of the insertion cart pipe as shown in Fig. 77. This shielding along with the lead covering over the tagger vacuum box as described above gave us more than a factor two background reduction for DC R3. The result of the simulation is summarized in Table 7 and the vertex plot is shown in Fig. 78. Finally, we also found that a concrete shielding pipe as shown in Fig. 77 reduces DC backgrounds. This pipe gave about 20% background reduction for DC R1 and a little improvement for DC R3.

IV.6.3 TOF Backgrounds

The TOF and DC R3 background sources are primarily the same so we did not study the TOF backgrounds in detail. I found that the TOF back panel scintillators are mostly affected by backgrounds compared to the forward panels. A detailed study revealed that this is due to the neutral particles that are generated in the photon blocker and not well shielded by the mass shielding (see the bottom right picture of

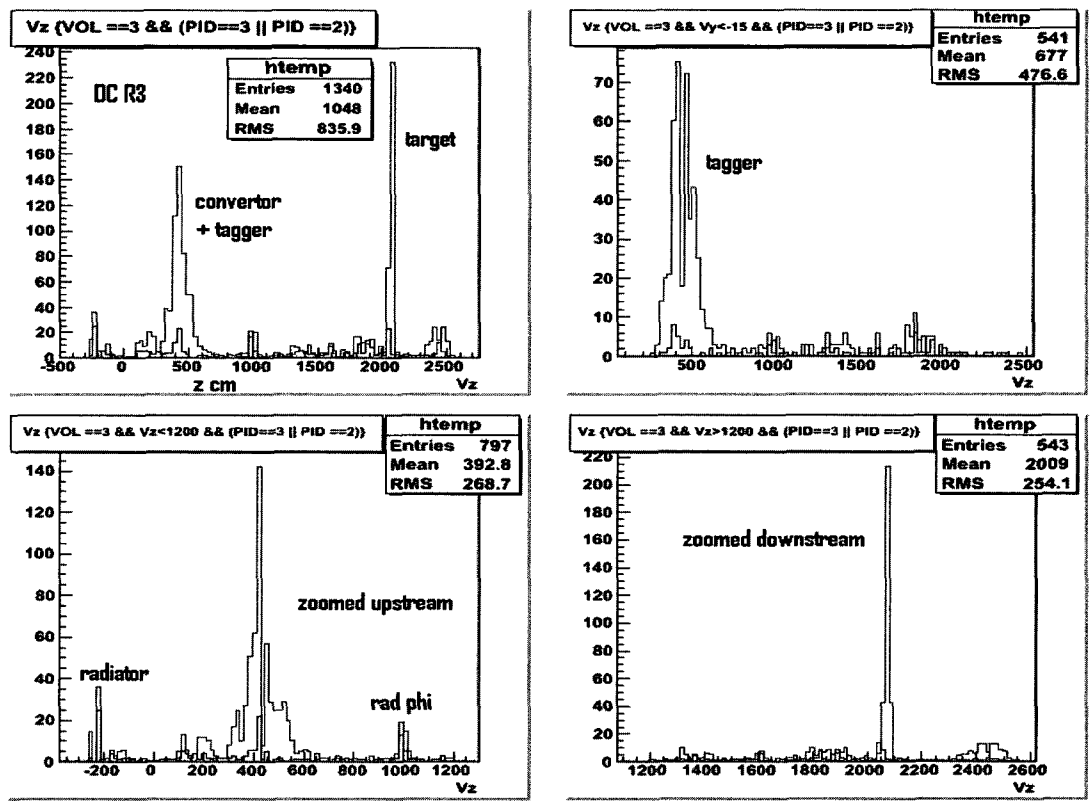

FIG. 78: Vertex z of charge particles passing through DC Region 3 mother volume for the test run (higher counts) and option 2 (lower counts) configurations. See text for details.

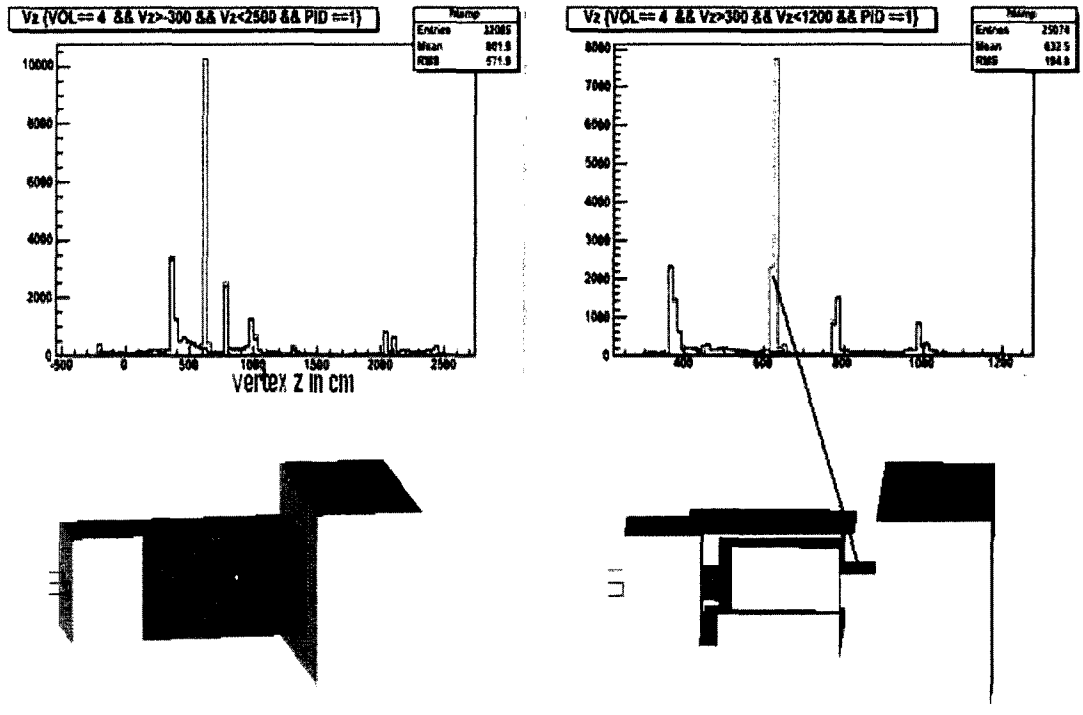

FIG. 79: The chicane shielding modification to control TOF backgrounds due to neutrals. The vertex origin of neutral particles before and after modification. The spikes at vertices other than 600 cm are not reducible source of backgrounds. The spike at 600 cm is due to the imperfect shielding used in the test run and disappears after the shielding modification.

Fig. 79) placed between the chicane magnets ID1 and PS. So I modified the test run shielding used in this region of beamline as shown in bottom right Fig. 79. The modified shielding is made by three layers of different materials. The inner, middle and outer layers are made up of lead, concrete and BPE with each of thickness 3 inches respectively. This shielding effectively reduced 35% gamma and 50% neutrons as shown in Fig. 79 where the spike at $z = 600$ disappears after using the modified shielding. It significantly reduced the TOF backgrounds because more than 50% of the total TOF rates was due to neutral particles.

IV.7 SUMMARY

The several short test runs done in the earlier part of the TPE experimental feasibility study showed us several possible background sources and provided very useful data that we used as a guideline to develop and test our GEANT4 simulation package. The preliminary simulation package before the October 2006 test run helped us identify the major background sources, eliminating unnecessary components in the tagger beamline, and designing shielding to control the remaining background sources. As a result we could develop a better experimental setup for the 2006 test run compared to the previous test runs. This test run produced a higher luminosity electron-positron beam as well as useful physics data. The tagger related backgrounds were reduced by more than a factor of 20 in this test run compared to the previous one. The existing simulation was then upgraded to match the exact 2006 test run experimental setup and was used to reproduce the test run data to validate the simulation. The valid simulation was used to further improve the beam luminosity by reducing the backgrounds that limit our luminosity.

At present we have completed the detailed study of background sources and shielding required to control the backgrounds. Most of the components and shielding required for designing the electron-positron beam line for the final experiment are optimized and ready for engineering design. We now know the cost effective way of running the experiment with very little or no modification to the existing CLAS beamline and detectors. The maximum luminosity can be achieved by using magnetic shielding from the existing minitorus, reducing the downstream collimator ID from 6 cm to 4 cm, using mass shielding to catch low energy Moller electrons in the target region, and increasing the target length from 18 cm to 30 cm. The region 3 and TOF background can be reduced by putting a thin lead covering over the tagger

vacuum box, shielding upstream and remaining tagger related background by putting mass shielding upstream of the CLAS and putting a steel shielding pipe between the insertion cart wall and downstream collimator. Based on this study we can run the experiment with luminosity 10 times greater than the test run luminosity.

CHAPTER V

DATA ANALYSIS

The Two Photon Exchange (TPE) experiment test run took place from October 3 through October 23 of 2006. The lepton beam required for the experiment was produced using the 3.2 GeV primary electron beam from the CEBAF accelerator as described in chapter III.2. The mixed e^+/e^- beam struck a 18 cm long, 6 cm diameter cylindrical liquid hydrogen target. The scattered leptons and recoil protons were detected in the CLAS detector. A trigger that requires a hit in TOF counters in opposite sectors was used to select $e^{\pm}p$ coincidence events. The estimated average e^+/e^- beam current for the experiment was about 60 pA (varying from 20-80 pA) and the estimated luminosity achieved was 5×10^{31} cm^{-1} s^{-1}. The data were collected with two torus polarities and the torus was used at a current of 1500 A for most of the runs. The data rate was between 0.5 kHz and 5 kHz depending upon the beam current, radiator thickness and convertor thickness selection. The run conditions are summarized in Table 8.

During the experimental run about half of the run time was used to identify the background sources and to shield them to achieve as high luminosity as possible. The data collected during this time were full of background and unusable.

The raw data were saved on tapes for further analysis. The data were saved in BOS bank [42] format. The TDC and ADC values from the detector channels as well as beam related information were stored in the data files. During analysis these files were processed using RECSIS, the standard CLAS data reconstruction software

TABLE 8: Test Run Summary.

Item	Value
Pirmary electron beam energy (GeV)	3.2
Average primary beam current (pA)	60
Tertiary lepton beam energy (GeV)	0.5 - 3.2
Tertiary lepton average current (pA)	15
Radiator thickness (% X_0)	0.5
Converter thickness (% X_0)	5
Target length (cm), diameter (cm) and material	18, 6, liquid H_2

package, in order to determine physical quantities such as particle types, positions, energies, momenta etc. In order to get the data for the physics analysis, the data need to be processed and calibrated. We used only information from the time of flight (TOF) detectors and drift chambera (DCs) for the data analysis. The calibration of DC and TOF were done by others and will be briefly discussed in the next section of this chapter. I did the DC alignment, which will be described in detail.

V.1 DATA PROCESSING AND CALIBRATION

The TPE test run data were processed using RECSIS. It is a FORTRAN based computer program for the reconstruction of the CLAS data. During processing, the raw times and amplitudes measured by the various detectors are converted into physical quantities such as times, momenta, vertex positions and energies. RECSIS consists of a software module for each detector. The detector module is designed to reconstruct hits from the raw data. Then the output from all the detectors is passed into the Simple Event Builder (SEB) [43]. SEB combines the hits from various detectors and produces output containing reconstructed events that can be used for further physics analysis The main goals of SEB are [43]:

- find the groups of geometrically matched tracks and hits;
- get the trigger particle and trigger time;
- identify particles;
- build an event and output BOS banks.

The information about the hits and tracks is read from the reconstructed BOS banks in order to perform the geometrical matching. The geometrical matching uses the relative distance between the detector (DC and TOF) hit positions (a_i) and the position on the detector planes (a_{pl}) generated by a Master track. DC tracks are considered as Master tracks and are matched with hits in TOF counters to find charged particle tracks. For each hit, the squared sum of the difference between the coordinates of the track and the detector hit is divided by the error on the coordinate of the detector hit position σ_{a_i}:

$$C_i^2 = \sum_{a=x}^{z} \frac{(a_{\rm pl} - a_i)^2}{\sigma_{a_i}^2}, \tag{37}$$

where i indicates the axis x, y or z for the given detector coordinates. The hit with minimum C_i is considered as a matched hit. The matching is done for all the tracks.

The next step is to identify the trigger particles that fulfill the experimental requirements. The TPE experiment did not use the conventional CLAS trigger because the usual single-electron trigger would miss electrons and positrons at large angles, limiting the coverage in ε. The trigger particles for this experiment were those that hit the TOF counters in the opposite sectors. Once this requirement was fulfilled the event was recorded.

V.1.1 Drift Chamber Calibration

The CLAS drift chamber (DC) system consists of six identical sectors. Each of the six sectors has an identical set of drift chambers which are divided into three regions. Each region is a separate physical volume containing two superlayers (axial and stereo). The schematic view of the Drift Chamber arrangement is shown in Figure 80. Each superlayer of each sector is calibrated separately which gives a total of 36 sets of parameters.

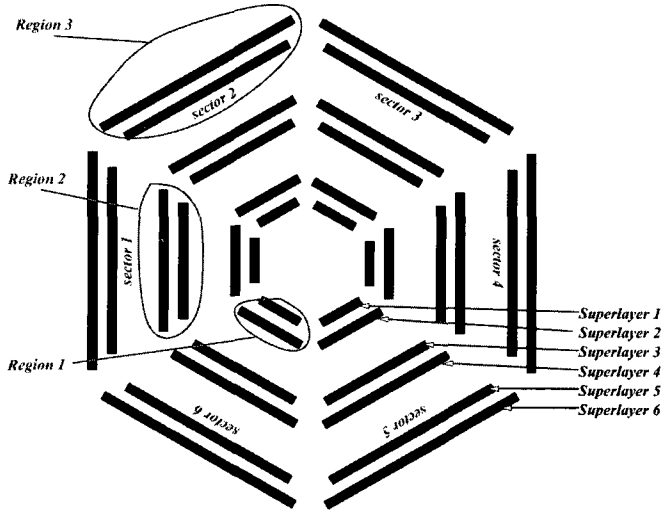

FIG. 80: Schematic view of the CLAS Drift Chambers. This view represents a vertical slice through the drift chambers at the target position. The schematic shows how the regions and superlayers are placed and named.

The main purpose of the Drift Chamber calibration is to refine the drift time to drift distance conversion to optimize position measurement. The constants for the drift time to drift distance conversion have to be systematically calibrated and

checked for stability over the run period. The calibration procedure consists of several iterations of running the reconstruction program followed by refitting the calibration constants.

The reconstruction of charged particles in the Drift Chambers is done in two stages. In the first stage, individual tracks are fit to hit-wire positions called hit-based tracking. In hit-based tracking the hits inside the superlayer are combined into track segments and then they are linked together to form tracks across all the three regions within one sector. Due to the comparatively small size of the drift cells and the large number of wire layers, the track momenta can be reconstructed with $3-5\%$ resolution [37] in hit-based tracking.

In the second stage, the time-of-flight information obtained from scintillator counters is used to correct the measured drift times for each wire hit. The drift time is given by

$$t_{\text{drift}} = t_{\text{TDC}} + t_0 - t_{\text{start}} - t_{\text{flight}} - t_{\text{prop}} - t_{\text{walk}}, \tag{38}$$

where t_{start} is the event start time defined in section V.1.3, t_0 is the fixed-time delay for the wire, t_{TDC} is the raw time measured by the wire, t_{flight} is the particle flight time from the reaction vertex to the wire, t_{prop} is the signal propagation time along the wire, and t_{walk} is a time-walk correction made for short times due to different ionization for slow and fast particles [44]. These drift times are then converted to drift distances using the constants we are calibrating. These drift distances give the Distance of Closest Approach (DOCA) of the charged particle track to the sense wire. This stage of tracking is called time-based-tracking (TBT). The final track is then fit to minimize the residual distance from the track to each of the calculated distance from the wire (DIST).

When a charged particle passes through the drift chambers, each of the 34 layers should get at least one hit. Each hit detected in the chamber is used to determine the particle's track with a least squares fit done in the CLAS reconstruction program. The distance of a charged particle track from a sense wire is described by two quantities called DOCA and DIST.

- *DOCA* (Distance Of Closest Approach) is the distance from the sense wire to the fitted track based on a fit to all the hit wires.

- *DIST* is the measured distance from the sense wire to the track, which is

calculated from the drift time and other parameters.

The difference between these quantities is called the "residual", defined as

$$Res = |DOCA| - |DIST|. \tag{39}$$

The sign of the residual is determined by the sign of any systematic time shift. The residuals are the primary means of measuring the resolution of the drift chambers. Note that $DIST$ is defined as positive definite, while $DOCA$ is assigned a sign determined by whether the track passes to the right or to the left of the wire. A more detailed description of the drift chamber calibration procedure is given in [44].

The Drift Chamber calibration is done in order to optimize the parameters of the drift velocity function for each superlayer in each sector. The drift velocity function is the relation between the distance of a particle track from the sense wire and the drift time. The time to distance correlation function is determined by the drift chamber geometry and operating conditions and the gas mixture. The non circular DC cells (hexagonal) leads to angle dependent corrections.

The track angle is the angle of the track relative to the side of the hexagon $0°-30°$. The drift time to drift distance function at a given track entrance angle is given by

$$x(t) = v_0 t + \eta\Big(\frac{t}{t_{\max}}\Big)^p + \kappa\Big(\frac{t}{t_{\max}}\Big)^q, \tag{40}$$

where v_0 is the saturated drift velocity near $t = 0$, and the coefficients η, κ, p and q are determined by fitting the time-to-distance correlation.

For tracks near the outer edge of the cell, the first arriving ions follow the electric-field line from the field wire to the sense wire, independent of entrance angle [37]. Their corresponding drift time is referred to as t_{max}. A normalized drift time $\hat{t} = t/t_{max}$ is used as an argument of the time-to-distance function that satisfies the cell boundary constraint:

$$x(\hat{t} = 1, \alpha) = C \cdot \cos(30° - \alpha), \tag{41}$$

where α is the track entrance angle and C represents the cell size. For a given entrance angle the time-to-distance function is deduced using a correction function:

$$x(\hat{t}, \alpha) = x_0(\hat{t}, \alpha_0) + C(\cos(30° - \alpha) - \cos(30° - \alpha_0))f(\hat{t}), \tag{42}$$

where x_0 represents the drift distance expected for a given normalized drift time assuming an entrance angle α_0. This entrance angle represents the average entrance

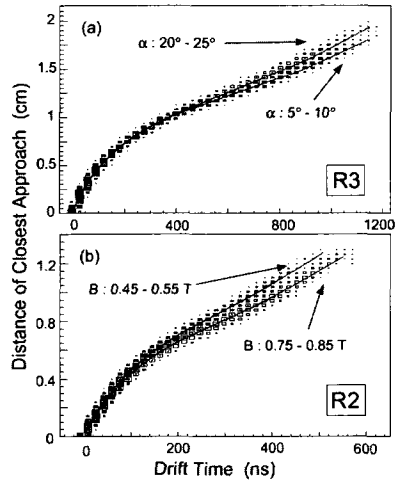

FIG. 81: Scatter plot of DOCA versus the corrected drift time for a) R3 axial wires showing the track local angle dependence, and b) R2 axial wires showing the magnetic-field dependence where the local angle ranges between 23° and 25°. The overlaid curves represent the fitted time-to-distance function [37]

angle for the full fitted data sample. The function $f(\hat{t})$ is used to correct the extracted drift distance for the true entrance angle of the track.

Since the Region 2 drift chambers are located between the torus cryostat, the inhomogeneous magnetic field affects the drift velocity. These effects are modeled by a modification to the effective entrance angle of the track and by an increase in $t_{\max}$. These issues are studied and described in [37]. Examples of fitted time-to-distance distributions are shown Figure 81.

The positive and negative torus polarity data were calibrated separately by following the usual DC calibration procedure described in [44]. The result of calibration is checked by plotting the mean and sigma of the double Gaussian fits to the residual distributions against the run number. Figure 82 shows the result of calibration where different colors corresponds to different superlayers.

V.1.2 Drift Chamber Alignment

Drift chamber alignment is a procedure to find the current position of the chambers in the hall. The relative wire to wire positions in each CLAS drift chamber and the chamber to chamber positions relative to each other are required to measure the

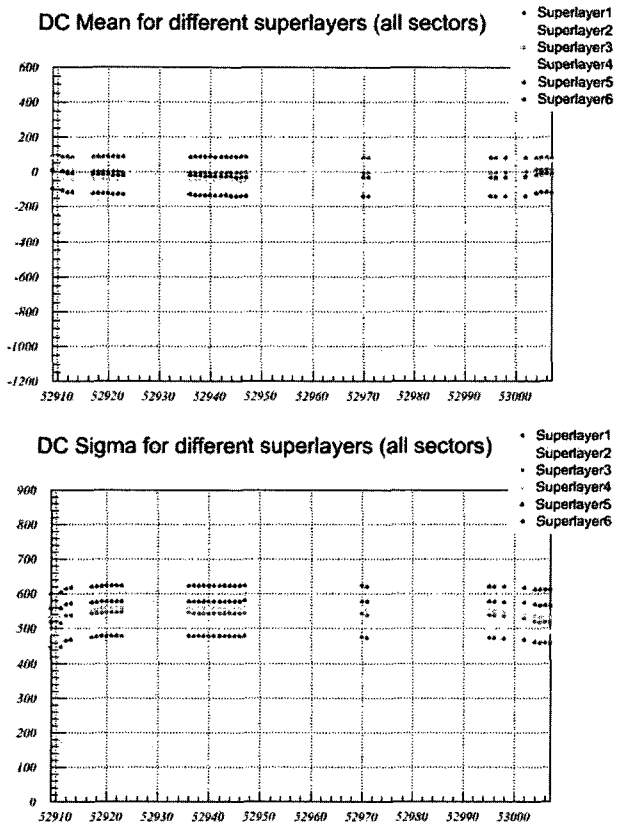

FIG. 82: Residuals weighted means (top) and standard deviations (bottom) in units of μm for all sectors versus run number for positive polarity runs [45]. The standard deviation of the residual corresponds to the spatial resolution of each wire.

momenta of particles with better resolution [46]. Small chamber misalignments can have a large effect on the momentum resolution due to reconstructing an incorrect radius of curvature of a track. The wire to wire position inside a single drift chamber is assumed to be fixed and is not taken into account in this alignment procedure. Only the individual drift chambers in the CLAS detector are aligned.

Straight tracks through the drift chambers are used for the alignment. So the data for the drift chamber alignment must be taken with torus magnetic field off. We used the g13 data taken just after the TPE experiment for the alignment. Immediately before the TPE run only the region 3 drift chambers were moved. So the alignment was done by varying the DC region 3 locations keeping the other two regions fixed. The alignment procedure began with several assumptions:

- The individual chambers are rigid bodies;
- Drift chamber twists and wire sag due to gravity can be neglected;
- Sectors are independent;
- Region 1 and 2 locations are correct.

The location and orientation of each of the chambers is described by a set of 6 offsets (3 translational (dx, dy and dz) and 3 rotational (θ_x, θ_y and θ_z). Initially the offsets are the difference between the chambers' ideal locations as in the engineering drawing and their measured locations determined by optical survey. The translational offsets are in cm and the rotational offsets are in rad. A set of these offsets are stored in a data file for each of the 18 chambers. The offsets are in the sector coordinate system in which [47]:

- x is along the ideal mid-plane of a drift chamber sector, pointing radially outwards;
- z is horizontal along the beam axis and in the beam direction;
- and y is defined by the right handed set with x and z.

We used the region 1 and 2 chambers as reference chambers. The straight tracks were fitted at the time based level to the reference drift chambers and at the hit based level to region 3 (only region 3 was moved during our experimental run period). The quantity defined below is minimized in order to find the best set of parameters [47].

$$\chi^2 = \sum_{tracks} \sum_{hits} \frac{(|DOCA_{track,hit}| - |DIST_{hit}|)^2}{\sigma^2_{track,hit} + \sigma^2_{hit}}, \tag{43}$$

where $DOCA_{track,hit}$ is the calculated distance of closest approach of the track to the hit wire, $DIST_{hit}$ is the drift distance calculated from the x vs. t function, $\sigma_{track,hit}$ is the uncertainty in the track position and σ_{hit} is the time based resolution of the hit.

The spatial residual is a parameter which determines the quality of the alignment. It is defined as

$$SRESI = DOCA_{track,hit} - DIST_{hit}. \tag{44}$$

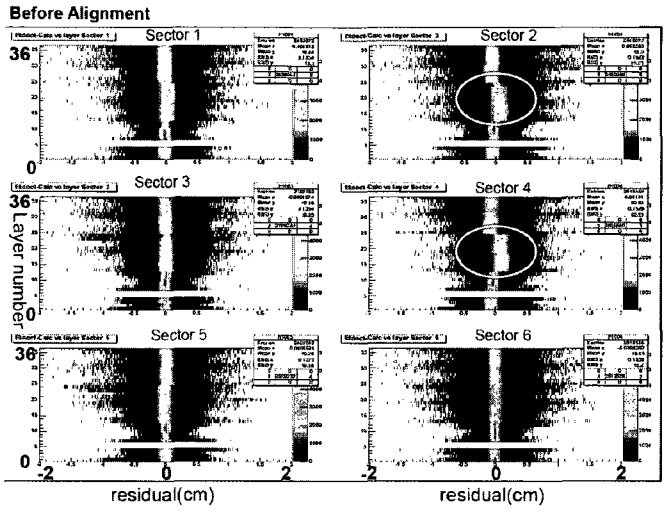

FIG. 83: DC layer number versus residual for each sector before the DC alignment. Layers 1–12 are in region 1, layers 13–24 are in region 2 and layers 25–36 are in region 3.

The DC alignment package consists of two main functions called *useralign* and *aligndc*. *Useralign* finds the straight tracks through the drift chambers, and produces useful histograms and ntuples and the BOS files needed to run *aligndc*. *Aligndc* fits the offsets to minimize the residuals of the straight tracks by selecting region, sector or parameter offset and creates new offset parameters. In order to limit the number of free parameters in the fit, only dx, dz and θ_y of region 3 were varied in the first pass. The residual was examined in each pass and the new offsets were updated in the database. In the second iteration only dy and θ_x were varied keeping the others unchanged and finally only θ_z was varied [48, 49]. After completing these three passes we found the set of offset parameters that aligned the chambers to a reasonable accuracy and further iterations did not improve the results. The layer number versus residual plots before and after the alignment are shown in Figs. 83 and 84. The plot of residual versus super layer number as shown in Fig. 85 shows that the average residual is less than the intrinsic DC resolution (200–500 μm).

V.1.3 TOF Calibration

The TOF counters are essential components of the CLAS detector. They are used to identify charged particles. The quality of particle identification primarily depends

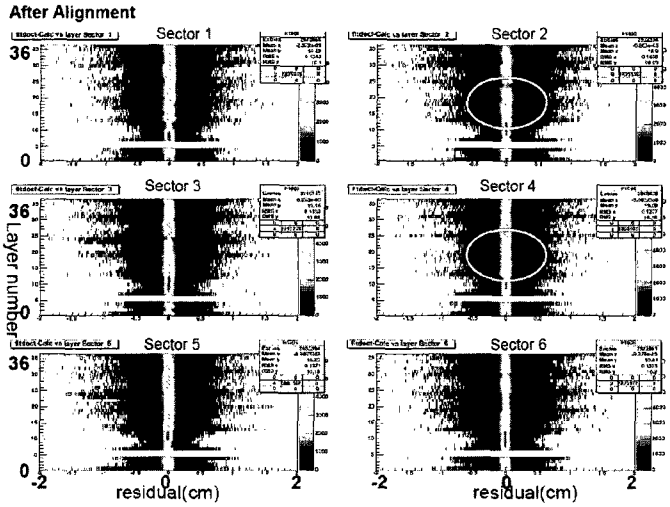

FIG. 84: DC layer number versus residual for each sector after the DC alignment. Layers 1–12 are in region 1, layers 13–24 are in region 2 and layers 25–36 are in region 3.

on the time of flight measurements.

The time of flight information is obtained from the scintillator paddles. There are two PMTs attached to each paddle. The data from each channel consists of an ADC pulse height and a TDC time. These ADC and TDC values are converted to energy and time during data reconstruction. The calibration of the time of flight system requires ADC pedestal determination, gain matching of the pulse heights, determination of time walk correction functions, and relative time offsets of each counter. The gain matching is done to make sure that each counter contributes equally to the trigger for a common threshold discriminator level. The timing of this threshold depends on the amplitude of the pulse that affects the steepness of the rising edge of the pulse. This gives rise to a dependence of the TDC signal on the ADC amplitude and is called the time-walk. The PMTs need to be calibrated to take the time-walk corrections into account. The ADC vs. TDC signal is fitted for each PMT in order to find the time-walk correction parameters. An example of the dependence of the TDC times on ADC pulse height is shown in Fig. 86. The solid line shows the fitted time-walk function.

Once the calibrations are completed the trigger start time can be calculated as

$$t_{\text{start}} = t_{\text{TOF}} - \frac{l_{\text{path}}}{\beta c}, \tag{45}$$

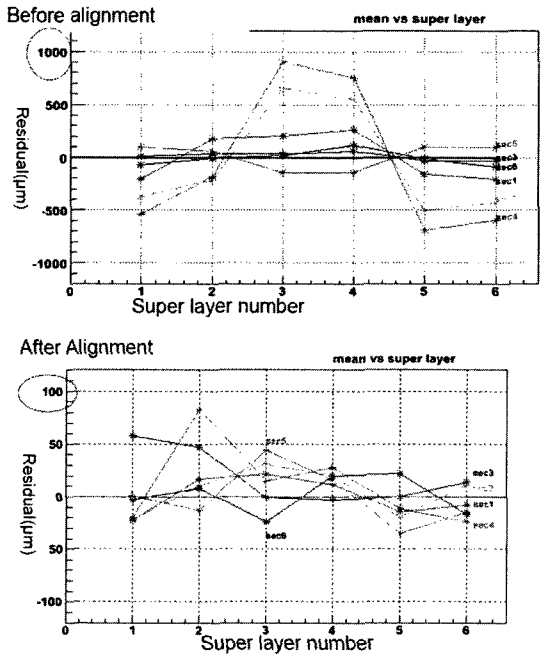

FIG. 85: DC residual versus super layer number. Top: before alignment, bottom: after alignment.

where t_{TOF} is the time measured by the scintillator counter, l_{path} is the path length obtained by tracing the charged particle back to the vertex along its track and β is 1 for electrons. For a detailed description of the TOF calibration refer to [39, 50].

V.2 SELECTING GOOD EVENTS

The events with two charged particles in the final state were chosen for the physics data analysis. This eliminates a large amount of non-elastic data and backgrounds. In order to select good elastic events from the two charged events, several cuts were applied. Their effect on eliminating non-elastic events and backgrounds are described below.

Vertex (V_Z) Cut

In order to get rid of events that are not related to the target, a cut on vertex-z, location along the beamline where the particle originated, was applied. We used a 18 cm long target placed along the beamline. So only events with $-10 < V_Z < 10$

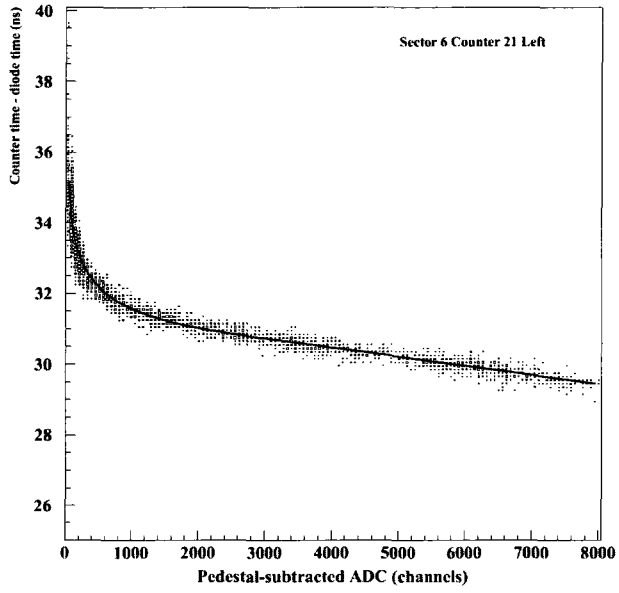

FIG. 86: Dependence of the TDC times (ns) vs. the pulse height (ADC counts). The line shows the fitted time-walk function.

cm were selected. The V_Z distribution of events without (black) and with all the cuts (blue) except itself is shown in the top left plot of Fig. 87. The azimuthal angle versus V_Z plot without any cut is shown in the top right plot of Fig. 87 where the high density region in the plot represents the length of the target.

Proton Identification Cut

If both tracks have positive charge then we do not know which particle in the event is the positron. For one positive and one negative track event, the negative track is always the electron but the other particle might be a π^+. So a cut on time of flight was applied to identify protons. All the events with both the tracks positive were tested twice to determine which matched the positron-proton better. The determination of the proton time of flight and the selection of cut is described below.

The arrival time of the proton at the TOF is calculated as shown below. First we calculated the event start time from the lepton time measured at the TOF.

$$t_{\text{start}} = t_{\text{lepton}} - \frac{l_{\text{path}}}{c}, \tag{46}$$

where t_{start} is the time lepton leave the target, t_{lepton} is the measured lepton time at the TOF, l_{path} is the path length of the lepton and c is the velocity of light.

So the proton time at the TOF can be calculated as

$$t_{\text{proton}} = t_{\text{lepton}} - \frac{l_{\text{path}}}{c} + \frac{p_{\text{path}}}{\beta c}, \tag{47}$$

where t_{proton} is the calculated proton TOF, p_{path} is the path length of the proton and $\beta = \frac{P}{E}$ is the proton velocity.

A loose cut ($\pm$ 10 ns) on the difference between the measured and calculated proton time (δ_{TOF}) is applied to select protons. The δ_{TOF} distribution without and with all cut is shown in the bottom right plot of Fig. 87.

Angle of the Total Momentum of the Final State Particles (θ_{Pt})

The beam has no transverse momentum component so the angle made by the total momentum of the final state particles (θ_{Pt}) with the beamline axis should be very small. Any final state particles that have θ_{Pt} large should correspond to undetected non-elastic events. In order to remove this kind of background we put a cut $\theta_{Pt} < 5°$. Effect of this cut on removing the background is shown in the bottom left plot of Fig. 87.

V.3 ELASTIC EVENT SELECTION

In order to select elastic events from the good events, several elastic kinematic cuts were applied. Their effect on eliminating non-elastic events and backgrounds are described below.

Azimuthal Angle Difference ($\delta\phi$) Cut

The difference between the lepton and proton azimuthal angles for elastic scattering should be 180° to satisfy co-planarity. To set a cut on the azimuthal angle difference for the elastic event identification, the difference is fitted with a Gaussian function. See the top left plot of Fig. 88. Based on this we selected the azimuthal angle difference range, $176.5° < \delta\phi < 183.5°$, which lies within $\pm 3\sigma$ from the centroid. The azimuthal angle difference without and with all the cuts except itself is shown in the top right plot of Fig. 88.

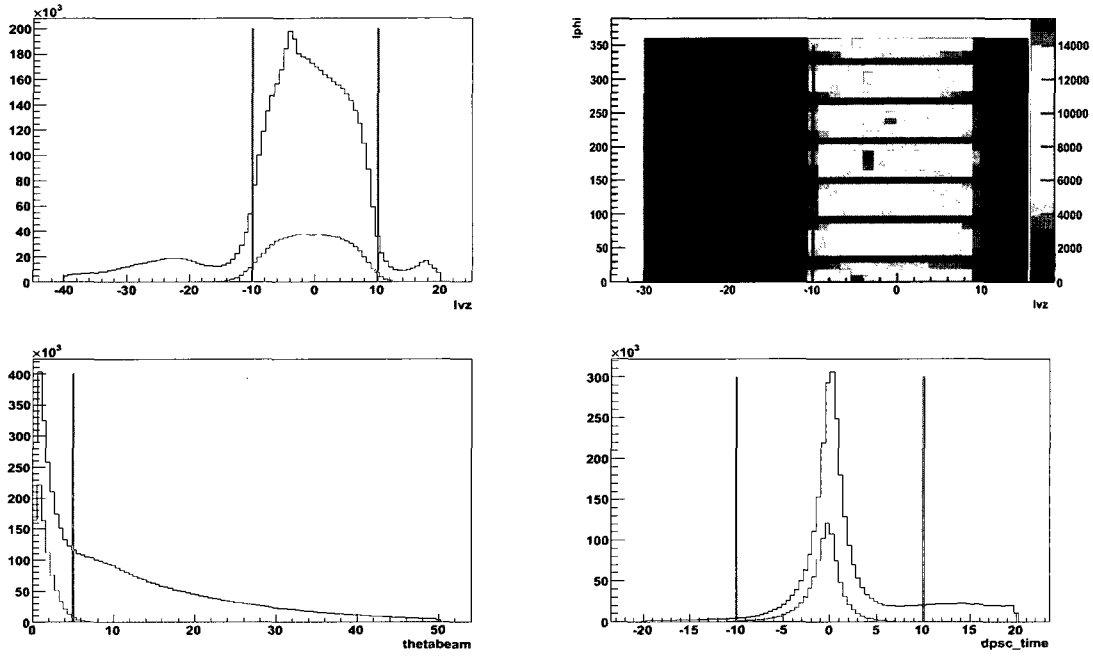

FIG. 87: Cuts applied to select good events. Top left: vertex-z (cm) distribution, top right: azimuthal angle ϕ (degree) vs. vertex-z (cm), bottom left: angle made by the total momentum of the final state particles (degree) and bottom right: proton time of flight difference (ns). Before and after cuts have higher and lower counts respectively. The vertical lines show the locations of the cuts.

Beam Energy Difference (δE_{beam}) Cut

The energy of the lepton beam is not known so we have to determine it from the measured kinematic variables. Since elastic scattering is over determined we can determine the beam energy in two ways. One uses the total momentum of the scattered particles along the beam direction and the other uses the scattering angles of the lepton and proton. Equations (48) and (49) give the lepton beam energy based on momentum and angles respectively.

$$E_{beam} = m_p \left(\cot \frac{\theta_e}{2} \cot \theta_p - 1 \right), \tag{48}$$

$$E_{beam} = p_e \cos \theta_e + p_p \cos \theta_p, \tag{49}$$

where the subscript e represents the lepton (electron or positron).

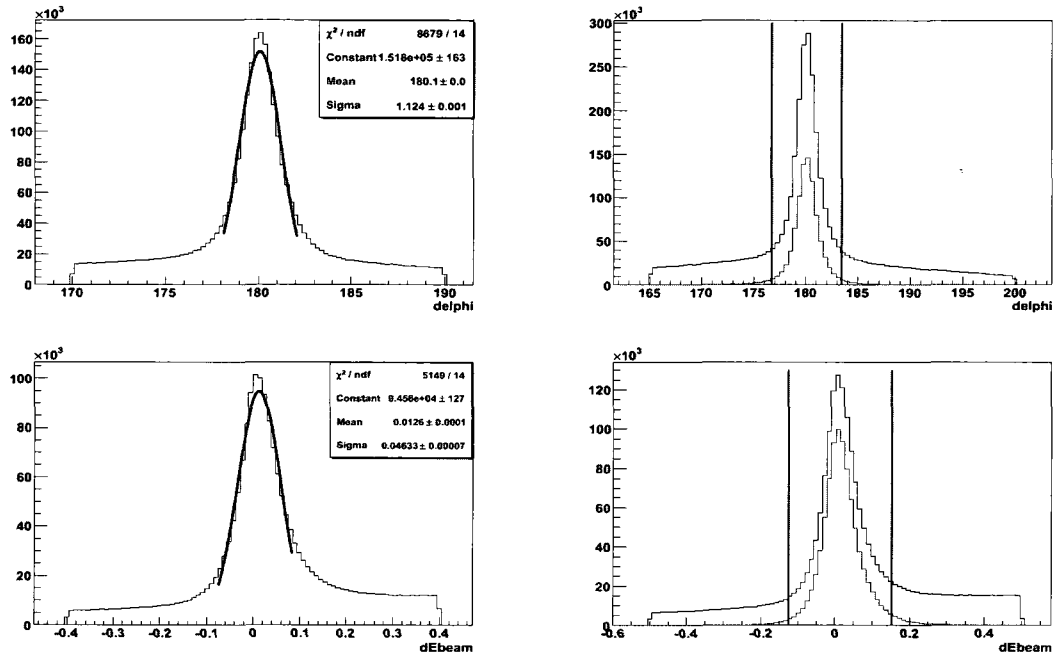

FIG. 88: Kinematic cuts applied to select elastic events. Top left: $\delta\phi$ in degree fitted with a Gaussian function, top right: $\delta\phi$ before (higher counts) and after (lower counts) all cuts except in itself, bottom left: δE_{beam} in GeV fitted with a Gaussian function, bottom right: δE_{beam} before (higher counts) and after (lower counts) all cuts except itself. The vertical lines show the locations of the cuts.

For elastic scattering, these two energies must be the same and hence the difference between these two should be zero. To find a suitable cut range for the difference in beam energy (δE_{beam}), the difference is fitted with a Gaussian function and the range, $-0.126 < \delta E_{beam} < 0.152$ GeV, within $\pm 3\sigma$ from the centroid is selected (see bottom left plot of Fig. 88). The δE_{beam} without and with all the cuts except itself is shown in the bottom right plot of Fig. 88.

Transverse Momentum Difference (P_t)

The electron and positron beam travels along the z-axis. For elastic scattering events, the total transverse momentum in the final state must be zero. So we applied this kinematic cut to remove inelastic background events. In order to find a suitable cut value, the total transverse momentum (P_t) was plotted and fitted with a Gaussian function as shown in the top left plot of Fig. 89. The cut value range, $-0.05 < P_t <$

0.076 GeV, within $\pm 3\sigma$ from the centroid is selected for this cut. The transverse momentum plot without and with all the cuts except itself is shown in the top right plot of Fig. 89.

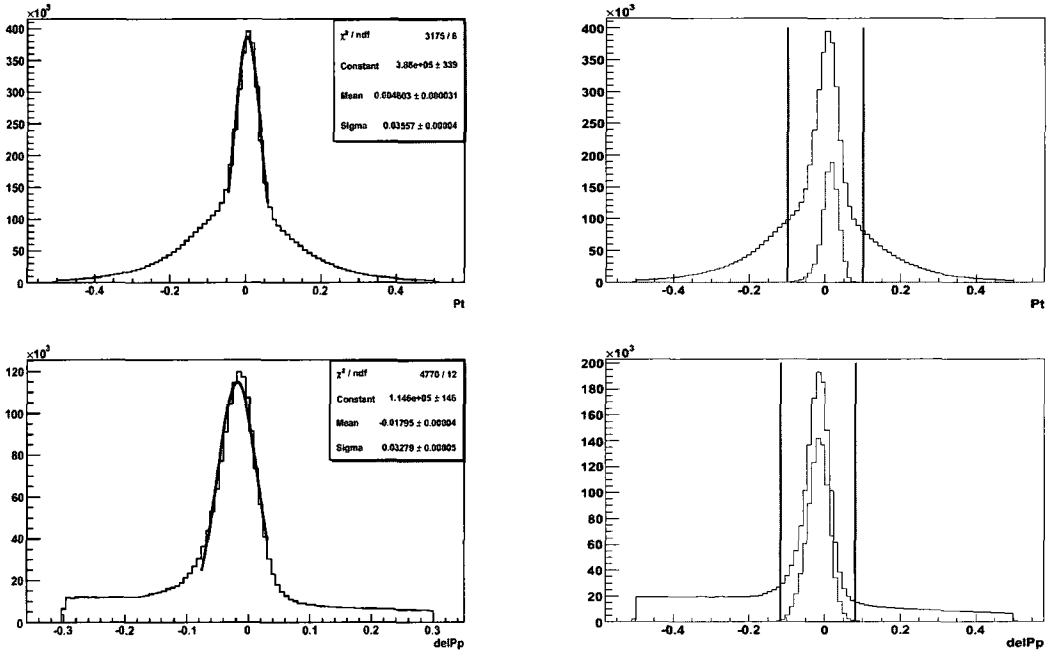

FIG. 89: Kinematic cuts applied to select elastic events. Top left: P_t in GeV fitted with a Gaussian function, top right: P_t before (higher counts) and after (lower counts) all cuts except in itself, bottom left: δP_p in GeV fitted with a Gaussian function, bottom right: δP_p before (higher counts) and after (lower counts) all cuts except itself. The vertical line shows the locations of the cuts.

Proton Momentum Difference (δP_p)

The difference between the measured and calculated momentum of the proton (δP_p) is used as another cut to select elastic events. The proton momentum is calculated as

$$P_p = \frac{E_{beam} - E'_e \cos\theta_e}{\cos\theta_p}, \tag{50}$$

where E'_e is the energy of the scattered lepton, and θ_e and θ_p are the scattering angles of the lepton and proton respectively. The events within the range $-0.1 < \delta P_p < 0.1$ GeV/c that lie within $\pm 3\sigma$ from the centroid are selected and rest discarded. The fit to the δP_p distribution and the δP_p without and with all the cuts except itself are shown in bottom left and right plots of Fig. 89.

V.3.1 Invariant Mass (W) cut

The invariant mass of the recoil hadron is calculated using the known four momenta of the initial state particles and the final state of the outgoing lepton. The four momenta of the incident particles can be written as

$$E^{\mu} = E_0(1, 0, 0, 1), \tag{51}$$

$$P^{\mu} = m_p(1, 0, 0, 0), \tag{52}$$

where E^{μ}, E_0 and P^{μ} are the incident electron 4-momentum, incident beam energy and target proton 4-momentum respectively.

Using 4-momentum conservation, the recoil proton 4-momentum can be expressed as:

$$h^{\mu} = E^{\mu} + P^{\mu} - E'^{\mu}, \tag{53}$$

where E'^{μ} is the measured 4-momentum of the scattered electron. The square of the invariant mass of the recoil proton can be calculated as:

$$W^2 = h^{\mu} h_{\nu}. \tag{54}$$

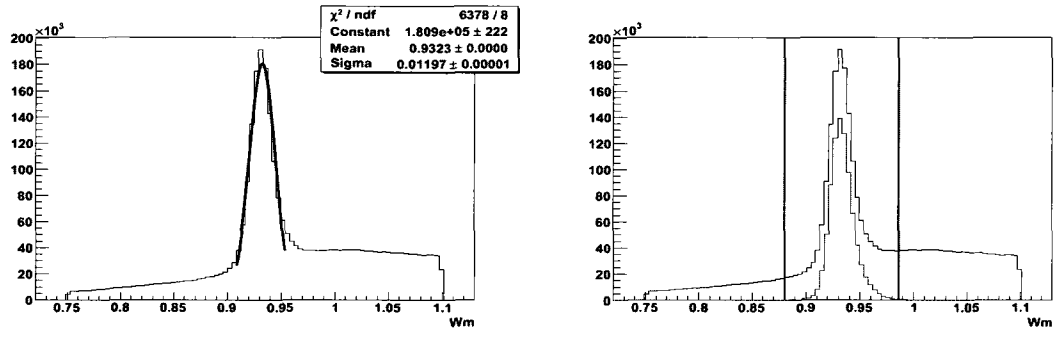

FIG. 90: Invariant mass W distribution. Left: Gaussian fit to W distribution, right: W without (higher counts) and with (lower counts) all the kinematic cuts except W itself. Red vertical lines indicate the location of the cuts.

As a final kinematic cut to select elastic events, a W cut in the range $0.87 < W < 0.99$ GeV which is within $\pm 5\sigma$ from the centroid is applied. The W distributions without and with cuts are shown in Fig. 90 for all the events with mixed torus polarities and particle types. The W distributions for different torus polarities and particle types are shown in Fig. 91.

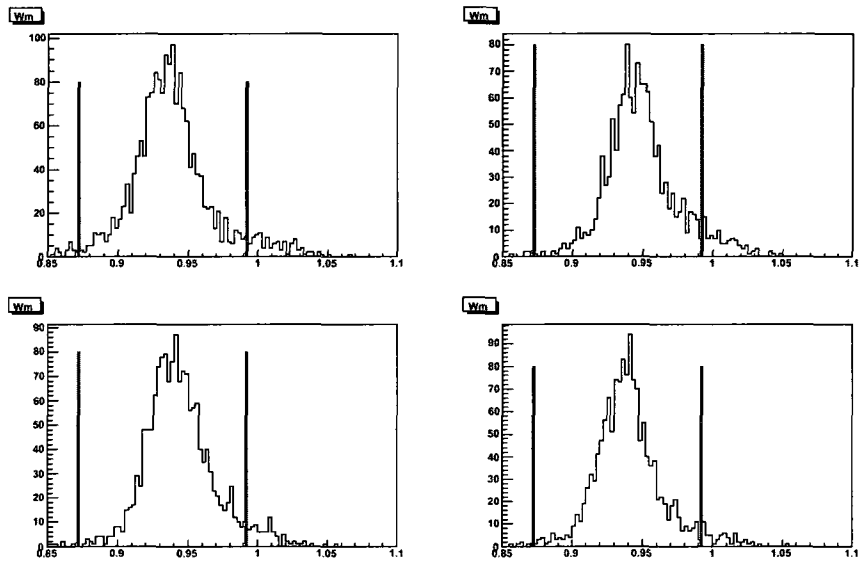

FIG. 91: Invariant mass W distribution for different torus polarities and particle types. Electron-proton events with positive and negative torus polarities are shown in top left and right plots respectively for small ε ($0.3 < \varepsilon < 0.55$) region. Positron-proton events are shown in bottom plots. Red vertical lines indicate the position of the cuts.

V.3.2 Fiducial Cut

In order to control the systematic uncertainty due to acceptance differences on the cross section ratio, a fiducial volume is selected where the acceptance was large and uniform. The fiducial volume is a smooth function of the momentum, scattering angle θ and azimuthal angle ϕ of the particle. We used the fiducial cut function from the g10 collaboration due to insufficient data to determine one from this data set. This function depended upon the momentum and charge of the particle for a particular torus magnetic field setting. We applied it twice for each particle, once for each possible charge. This ensured that the particle will lie in the good fiducial region for any torus polarity and any charge. The plot of azimuthal angle ϕ versus scattering angle θ for electron and positron without and with fiducial cuts are shown in Fig. 92 and Fig. 93 respectively. This shows that a large number of events are cut out by the fiducial cut at small scattering angle where the acceptance for in bending and out bending particles differs.

TABLE 9: Kinematic cuts used to select elastic events.

Parameter	Cut value range
$\delta\phi$	$176.5° < \delta\phi < 183.5°$
δE_{beam}	$-0.126 < \delta E_{beam} < 0.152$ GeV
δPt	$-0.05 < Pt < 0.076$ GeV/c
δPp	$-0.1 < \delta Pp < 0.1$ GeV/c
W	$0.87 < W < 0.99$ GeV

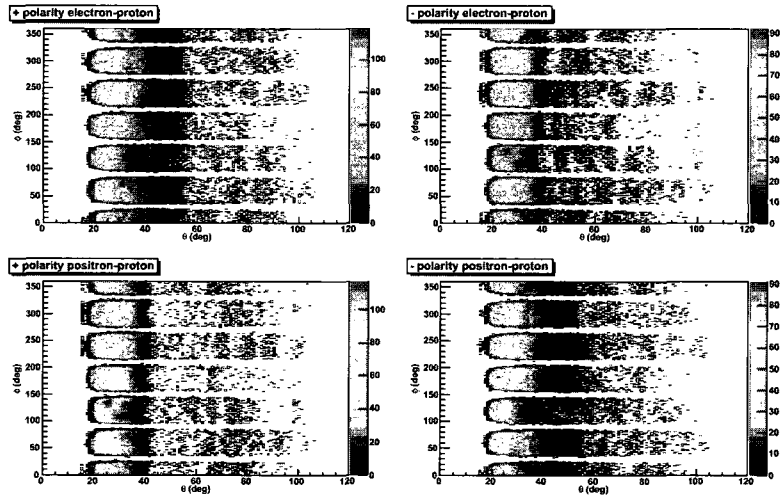

FIG. 92: Azimuthal angle (ϕ) versus polar angle (θ) distributions of leptons before the fiducial cuts.

V.3.3 Acceptance Matching

In order eliminate the time of flight (TOF) paddles that were dead or malfunctioning, the number of counts for each scintillator paddle was plotted as shown in Fig. 94 for mixed data types and polarities. The TOF paddles that had very low counts compared to the neighboring paddles were identified and removed from the data as described below. The identified TOF bad paddles are listed in Table 10.

Another technique called "swimming" was also applied to reduce acceptance effects due to differences in detecting electron and positron events by a good scintillator paddle. A charged particle track with particular momentum and scattering angle was traced out to the scintillator paddles and was required to strike a good scintillator

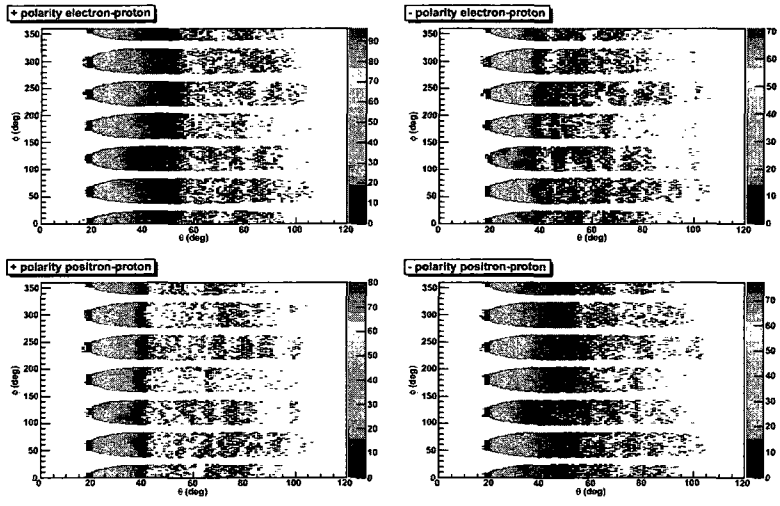

FIG. 93: Azimuthal angle (ϕ) versus polar angle (θ) distributions of leptons after the fiducial cuts.

TABLE 10: TOF bad paddles.

Sector Number	Bad Paddle Numbers
1	8, 31
2	8, 34
3	7, 10, 11, 24
4	26, 32
5	36
6	1, 10, 24, 25

paddle. The process was repeated for the opposite charge track with the same momentum and scattering angle. If both the particles would have been detected by a good scintillator paddle it was considered a good event otherwise the event was discarded. The acceptance matching technique made sure that the electrons and positrons have the same chance of getting detected by a good scintillator paddle for any torus polarity setting. The acceptance matching technique is illustrated in Fig. 95 for positive torus polarity.

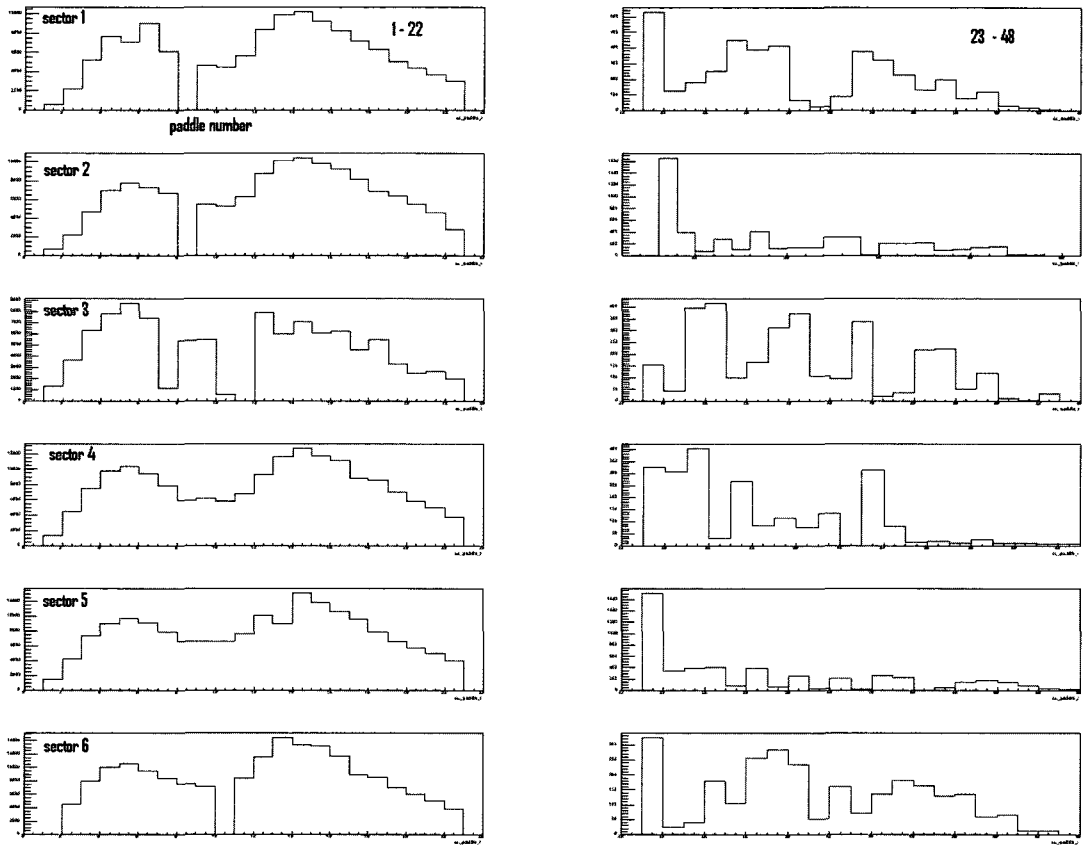

FIG. 94: TOF counts for each paddle number in order to find bad paddles. Paddles from 1 to 22 are plotted in the left and the rest of the paddles are plotted in the right side plots for each sector.

V.3.4 Elastic Events and Binning

After applying all the kinematic cuts, fiducial cuts and acceptance matching cuts the clean elastic events were identified. Some of the kinematic variables for the selected elastic events are shown in Fig. 96 and Fig. 97. Due to the low luminosity and small beam energy the majority of our data lies in the large ε and small Q^2 region. This data covered Q^2 up to 1.0 GeV^2 and ε in the range $0.2 < \varepsilon < 1.0$ although little data exists for epsilon in the range $0.2 < \varepsilon < 0.7$.

The majority of the data that lies in the large ε and small Q^2 region was already analyzed by M. Moteabbed at Florida International University [45]. My effort is to add two more data points, one in the small ε and moderately high Q^2 and the other at larger ε and moderately high Q^2. After all the cuts and corrections, the available

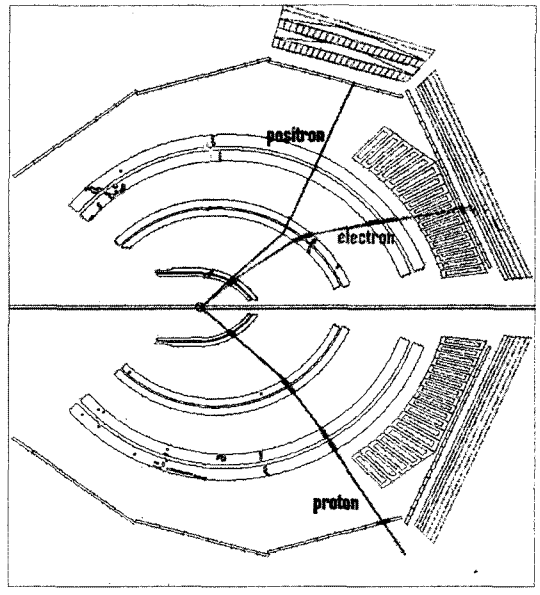

FIG. 95: Acceptance matching using the "swimming" technique for positive torus polarity. The in bending electron is shown. The corresponding track for an identical positron is required to hit a good TOF paddle for the event to be accepted.

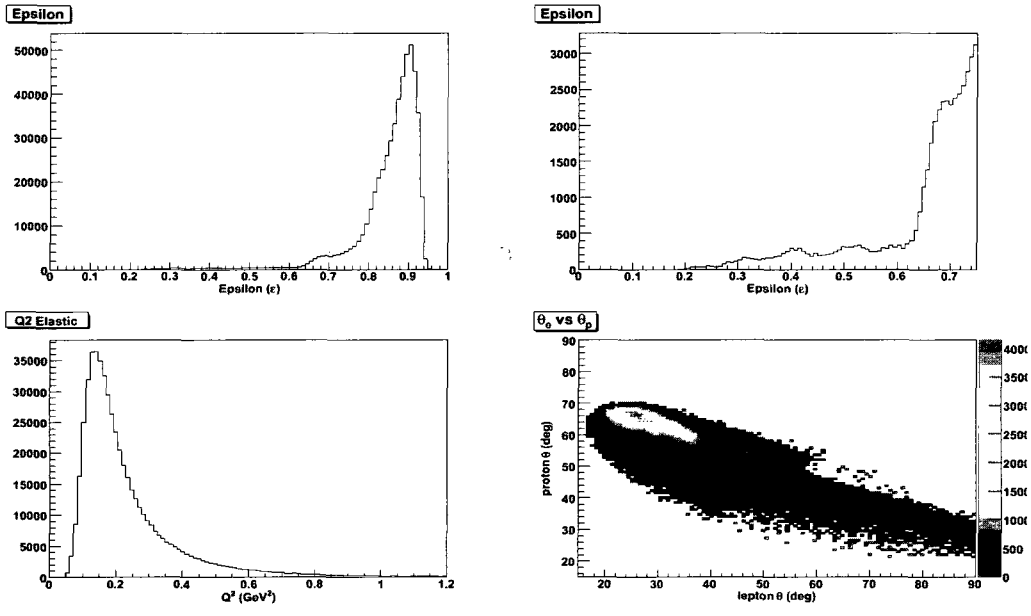

FIG. 96: Kinematic variables for the elastic events for mixed particle types and torus polarities. Top plots show the ε distribution of the elastic events (left all and right $\varepsilon < 0.75$). The Q^2 distribution is shown in bottom left and bottom right plot shows the electron scattering angle versus recoil angle of the proton.

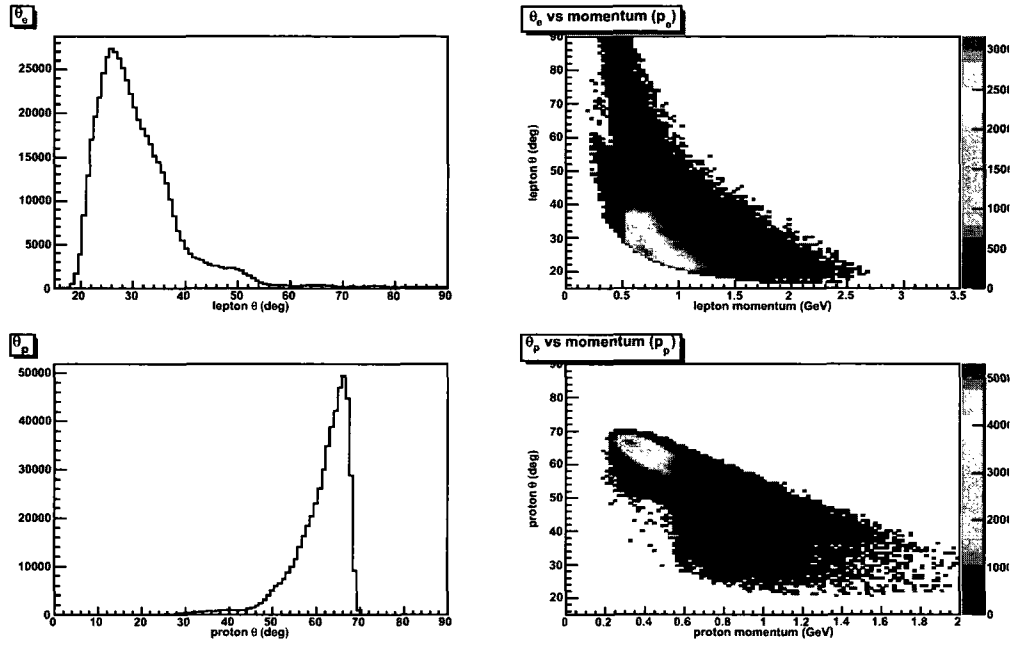

FIG. 97: The scattering angle and scattering angle versus momentum are shown for leptons (top left and right) and for protons (bottom left and right). Both torus polarities are included.

data in the Q^2 and ε space is shown in Fig. 98 for different polarity and particle types. Due to the very limited statistics in the region of interest, I chose a very large Q^2 and ε range for each bin. The bins are chosen so that there exists data in all the four combination of torus polarity and particle types as shown in Fig. 98.

V.4 RESULTS AND DISCUSSION

V.4.1 The Cross-Section Ratio

For elastic scattering the cross-section can be written as

$$\sigma_{elastic} = \frac{N_{elastic}}{\mathcal{L}\Delta Q^2 \Delta\varepsilon}, \tag{55}$$

where $\mathcal{L}$ is the integrated luminosity and $N_{elastic}$ is the number of elastic scattering events.

Using Eq. (55) we can calculate the cross-section ratio by dividing the number of elastic positron-proton events by the number of elastic electron-proton events if the luminosity of the electrons and positrons are equal. But in reality the ratio

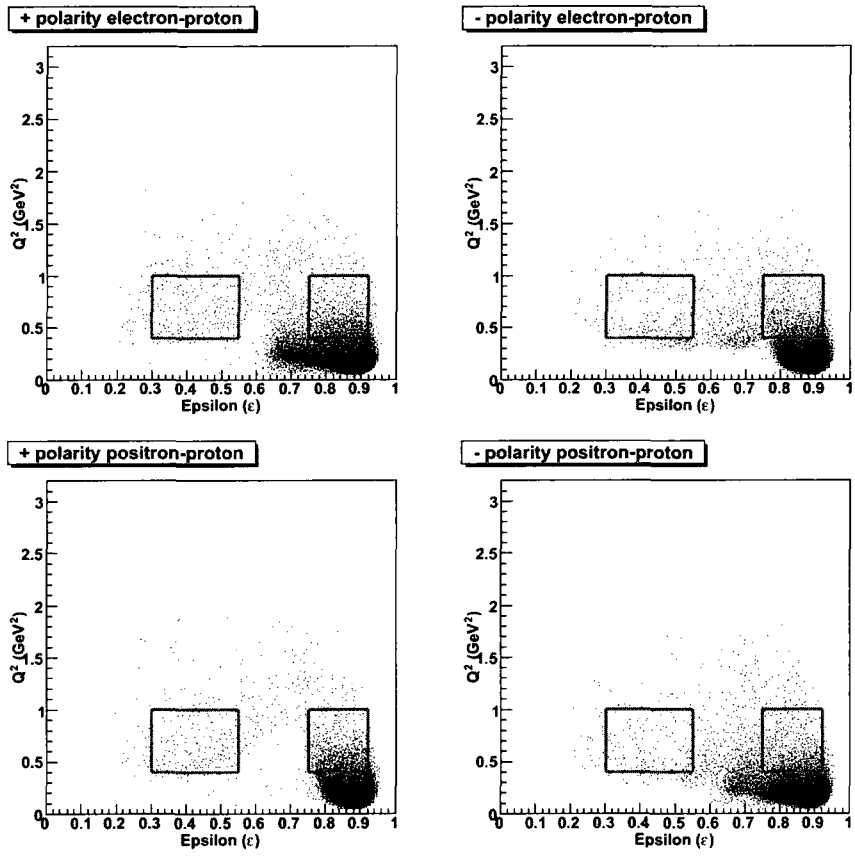

FIG. 98: Q^2 versus ε for different torus polarities and particle types.

TABLE 11: Positron-proton to electron-proton ratio for positive torus polarity.

Cuts and Corrections	$< Q^2 >= 0.6$, ε=0.42	$< Q^2 >$=0.54, ε=0.83
Elastic	0.92±0.03	1.0±0.012
Elastic + Fiducial	0.918±0.032	0.966±0.013
Elastic + Acceptance	0.906±0.031	0.908±0.012
Elastic + Fiducial + Acceptance	0.905±0.032	0.89±0.012

also depends on the geometrical acceptances and the luminosity differences. The acceptance related differences between electron and positron were carefully studied and minimized. An upper limit on the luminosity difference was estimated using the GEANT4 simulation and included in the systematic uncertainty.

After selecting the elastic events, the number of electron-proton and positron-proton events for each torus polarity and bin are counted. The ratio and uncertainty for each polarity are calculated as

$$R_+ = \frac{N_+^{e^+p}}{N_+^{e^-p}}, \tag{56}$$

$$R_- = \frac{N_-^{e^-p}}{N_-^{e^+p}}, \tag{57}$$

$$\delta R_\pm = R_\pm \sqrt{\left(\frac{\delta N_\pm^{e^+p}}{N_\pm^{e^+p}}\right)^2 + \left(\frac{\delta N_\pm^{e^-p}}{N_\pm^{e^-p}}\right)^2}, \tag{58}$$

where N represents the number of counts and $\pm$ represents the torus polarity.

The ratio of positron-proton to electron-proton elastic events for each bin for positive and negative torus polarity are shown in Table 11 and Table 12 respectively. This ratio is expected to be close to unity within a few percent but we see that it varies from 0.9 to 1. Note that the fiducial and acceptance cuts have a much larger effect on the ratio at large ε where the acceptance for in bending and out bending leptons is very different.

Acceptance matching and fiducial cuts are applied to reduce the acceptance differences between the in bending and out bending leptons. The bad TOF scintillator paddles are also removed while doing acceptance matching.

TABLE 12: Electron-proton to positron-proton ratio for negative torus polarity.

Cuts and Corrections	$< Q^2 >= 0.6$, ε=0.42	$< Q^2 >$=0.54, ε=0.83
Elastic	0.87±0.033	1.0±0.014
Elastic + Fiducial	0.87±0.034	0.98±0.015
Elastic + Acceptance	0.87±0.034	0.93±0.014
Elastic + Fiducial + Acceptance	0.89±0.035	0.91±0.015

TABLE 13: Positron-proton to electron-proton ratio independent of torus polarity.

Cuts and Corrections	$< Q^2 >= 0.6$, ε=0.42	$< Q^2 >$=0.54, ε=0.83
Elastic	1.02±0.05	1.0±0.018
Elastic + Fiducial	1.02±0.05	0.996±0.02
Elastic + Acceptance	1.02±0.05	0.99±0.019
Elastic + Fiducial + Acceptance	1.01±0.05	0.987±0.02

In order to reduce the remaining acceptance differences in the positron-proton to electron-proton elastic scattering cross-section ratio, the square root of the double ratio is calculated as

$$R = \sqrt{\frac{R_+}{R_-}}, \tag{59}$$

$$\delta R = R\sqrt{\left(\frac{\delta R_+}{R_+}\right)^2 + \left(\frac{\delta R_-}{R_-}\right)^2}. \tag{60}$$

The result so obtained is independent of the torus polarity. The acceptance differences for the two torus polarities cancel in the ratio because the acceptance for a positron-proton event for positive torus polarity is similar to the acceptance for an electron-proton event for negative torus polarity and vice versa. The ratio for the selected bins with the combination of cuts and corrections are shown in Table 13. Note that the positron-electron cross section ratio R extracted from the double ratio (see Eq. 59) is not significantly affected by acceptance and fiducial cuts.

V.4.2 Systematic Uncertainties

The goal of the experiment is to measure the electron-positron cross section ratio very precisely in order to extract the very small TPE correction. We used several techniques to reduce the systematic uncertainty during the data analysis procedure but still there are some systematic uncertainties that affect our final result. The main sources of uncertainty and their estimates are described below.

Luminosity Differences

The luminosity differences come from the differences in electron and positron transport from the convertor where they are created to the target. Most of these differences can be taken care of by reversing the torus polarity as well as the chicane magnets polarity which interchange the incident lepton beams. The torus polarity was reversed in the test run but not the chicane polarity. The chicane polarity will be reversed in the future run. Even though the leptons are created symmetrically, there might be differences in their attenuation in various beamline components as well as in their transport through the chicane [17].

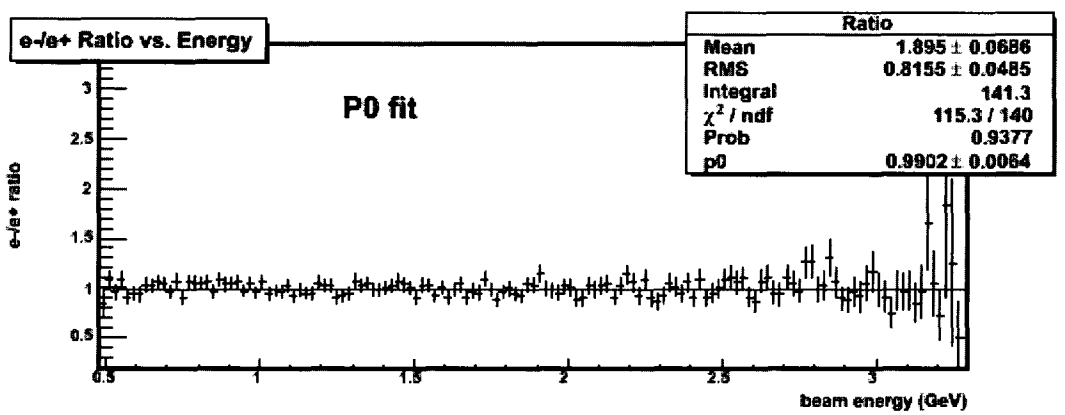

FIG. 99: Ratio of electron to positron beam flux plotted as a function of beam energy. The ratio is $1.0 \pm 0.6\%$.

The systematic uncertainty due to luminosity differences (ΔR_L) is calculated with the help of the GEANT4 simulation developed for the background study and luminosity optimization. The lepton beams were created starting from the radiator and transported using the October 2006 test run beamline to the target. The electron and positron beam profiles were recorded at the target and the ratio of the electron

TABLE 14: Systematic uncertainties for each bin (%) due to acceptance cut, fiducial cut and luminosity differences are ΔR_{Acc}, ΔR_{Fid} and ΔR_L respectively.

($< Q^2 >$ GeV^2, ε)	ΔR_{Acc}	ΔR_{Fid}	ΔR_L
(0.6, 0.42)	0.9	0.5	1
(0.54, 0.83)	0.9	0.5	1

to the positron flux was plotted as a function of beam energy. A constant fit to the ratio as shown in Fig. 99 showed $1.0 \pm 0.6\%$ more positrons than electrons. Thus we assigned a 1% systematic uncertainty due to the possible differences in lepton flux. The uncertainty due to luminosity differences is shown in Table 14.

Acceptance Differences

The acceptance effects were reduced by using several techniques. The torus polarity was reversed and the ratio was calculated for each torus polarity. This way the differences in electron and positron acceptance cancel in the double ratio. The fiducial region was selected in such a way that electrons and positrons will have the same acceptance. Further acceptance matching was done by swimming the lepton through the CLAS detector and choosing only leptons that would have been accepted if one is replaced by other. This makes sure that the electron and positron will have the same probability of detection by a good scintillator paddle irrespective of the torus polarity. The systematic uncertainties due to acceptance differences (ΔR_{Acc}) and fiducial cut selection (ΔR_{Fid}) are determined by calculating the difference in the double ratio without and with acceptance and fiducial cuts respectively. These uncertainties are shown in Table 14.

Kinematic Cut Studies

The systematic uncertainty due to the kinematic cuts is estimated by removing the cuts one at time. The weighted mean of the difference between the ratio with all the cuts and all the cuts except itself is calculated and this value is assigned to the systematic uncertainty due to that cut. The systematic uncertainty due to each kinematic cut is summarized in Table 15.

TABLE 15: Systematic uncertainties for each bin (%) due to $\delta\phi$, δE_{beam}, P_t, δP_p and W cuts are ΔR_ϕ, ΔR_E, ΔR_{Pt}, ΔR_{Pp} and ΔR_W respectively. The total uncertainty is ΔR_{Sys}.

($< Q^2 >$ GeV^2, ε)	ΔR_ϕ	ΔR_E	ΔR_{P_t}	ΔR_{P_p}	ΔR_W	ΔR_{Sys}
(0.6, 0.42)	1.58	0	0	1.23	1.2	2.58
(0.54, 0.83)	0.42	0.07	1.0	0.04	0.06	1.52

The total systematic uncertainty is the quadratic sum of the individual uncertainties for the selected bin. The total systematic uncertainty (ΔR_{Sys}) for the low ε bin is found to be almost double (2.58%) to that of high ε bin (1.52%).

V.4.3 Comparison to Existing Data

The final result of the data analysis is plotted with the existing world data for the cross section ratio, $R = \sigma_{e+}/\sigma_{e-}$, as a function of ε in Fig. 100 and as a function of Q^2 in Fig. 101. The result is consistent with the previous measurements with equal or better statistical uncertainties for the data points in the same range of Q^2 and ε.

The cross-section ratio was extracted by the FIU group at low Q^2 and large ε. The result was found to be consistent with previous measurements in the same kinematic range [26, 27, 29, 33] with better statistical uncertainty [45] as shown in Fig. 102.

V.4.4 Conclusion

The test run was intended to produce an identical mixed electron-positron beam for the future experiment and to determine the maximum luminosity as well as limiting factors. But we also collected significant amounts of elastic scattering data in the final part of the run period.

My analysis of the remaining data showed similar results compared to the previous analysis. I added two more data points to the previously analyzed data as shown in Fig. 102. This is a very good result from an engineering test run that was performed to test the beamline design and finding the luminosity limiting factor.

Due to the luminosity limitation we could not measure the TPE correction at high Q^2 and low ε where the TPE effect is expected to be largest. The future TPE experiment will run at higher luminosity and higher beam energy with a longer target.

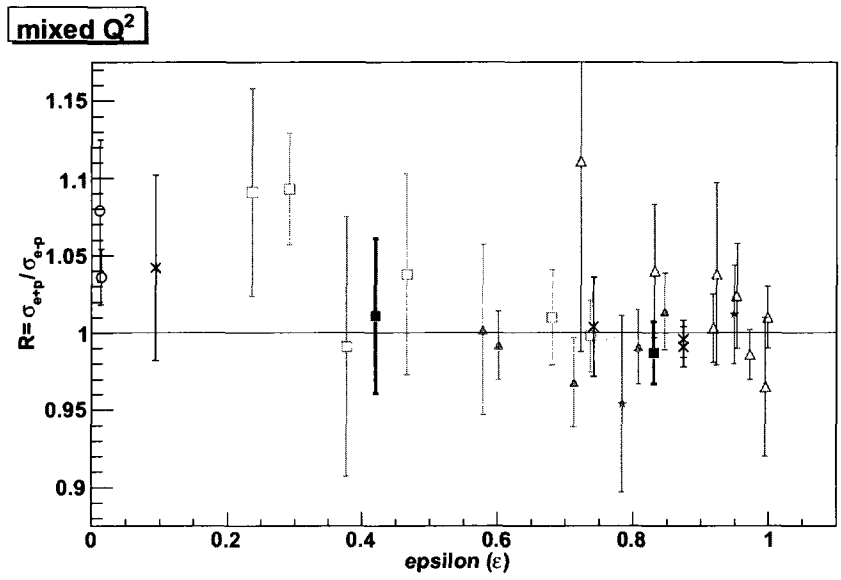

FIG. 100: The existing world data for the cross section ratio, $R = \sigma_{e+}/\sigma_{e-}$, as a function of ε. The different colors and symbols differentiate the experiments. crosses [26], squares [27], filled circle [28], filled triangles [29], open circles [32], open triangles [33], stars [31], filled squares TPE test run (this experiment).

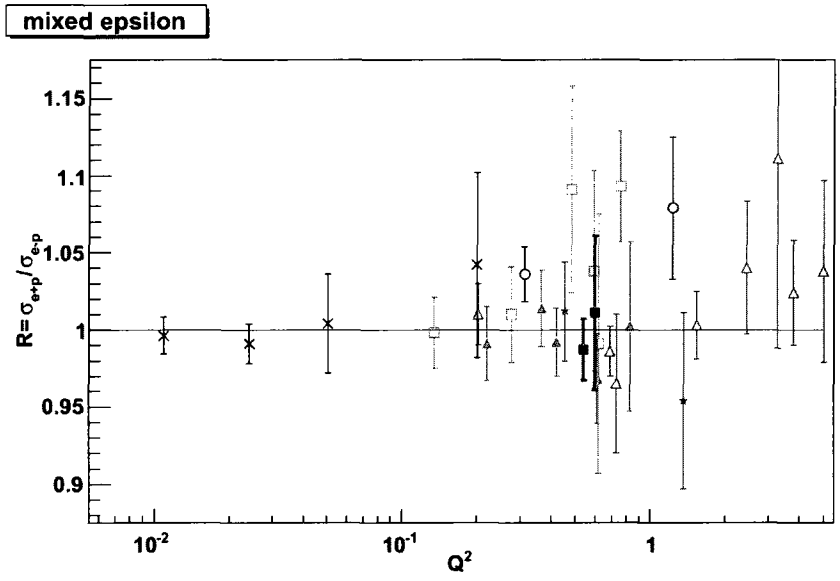

FIG. 101: The existing world data for the cross section ratio, $R = \sigma_{e+}/\sigma_{e-}$, as a function of Q^2. The markers are same as in Fig. 100.

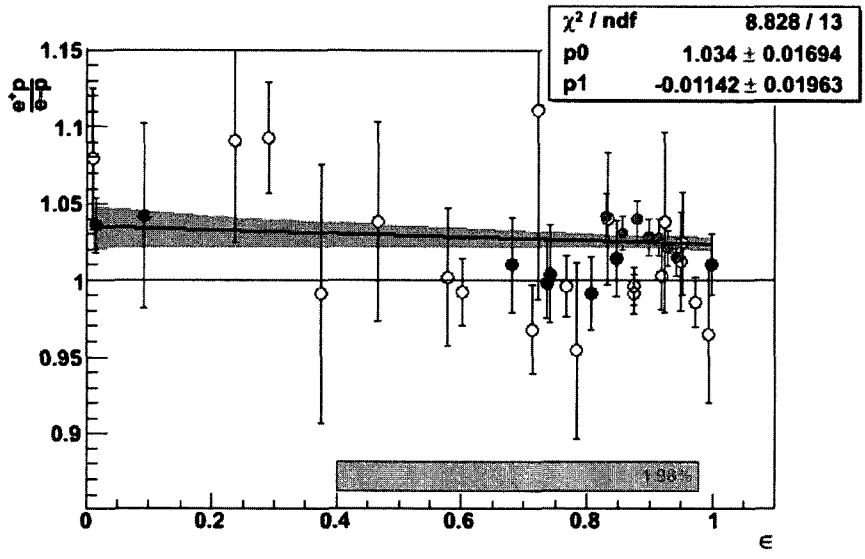

FIG. 102: Cross section ratio, $R = \sigma_{e+}/\sigma_{e-}$, as a function of ε extracted by FIU group is shown in red filled circles [45]. Hollow circles represent the world data and the world data with a comparable Q^2 to this measurement are shown in filled circles [26, 27, 29, 33]. A linear fit to this data along with the world data with a comparable Q^2 is also shown in the plot.

This experiment will be able to collect more data and to extract a more precise TPE correction needed to explain the existing discrepancy between the Rosenbluth and polarization transfer methods of measuring the electromagnetic form factors of the proton.

BIBLIOGRAPHY

[1] B. Povh, K. Rith, C. Scholz, and F. Zetsche, *Particles and Nuclei*, New York: Springer (1995).

[2] F. Halzen and A. D. Martin, *Quarks and Leptons*, New York: John Wiley & Sons (1979).

[3] M. N. Rosenbluth, Phys. Rev. **79**, 615 (1950).

[4] M. C. Christy *et al.*, Phys. Rev. C **70**, 015206 (2004).

[5] L. Andivahis *et al.*, Phys. Rev. D **50**, 5491 (1994).

[6] O. Gayou, "Measurement of the Proton Form Factors Ratio up to $Q^2 = 5.6$ GeV^2 by Recoil Polarimetry," Ph.D. diss., The College of William and Mary (2002).

[7] O. Gayou *et al.*, Phys. Rev. Lett. **88**, 092301 (2002).

[8] M. K. Jones *et al.*, Phys. Rev. Lett. **84**, 1398 (2000).

[9] I. A. Qattan *et al.*, Phys. Rev. Lett. **94**, 142301 (2005).

[10] P. A. M. Guichon and M. Vanderhaeghen, Phys. Rev. Lett. **91**, 142303 (2003).

[11] J. Arrington, Phys. Rev. C **68**, 034325 (2003).

[12] I. A. Qattan, "Precision Rosenbluth measurement of proton elastic electromagnetic form factors and their ratio," Ph.D. diss., Northwestern University (2005).

[13] J. Arrington, Phys. Rev. C **69**, 032201 (2004).

[14] J. Arrington, Phys. Rev. C **69**, 022201 (2004).

[15] P. G. Blunden *et al.*, Phys. Rev. Lett. **91**, 142304 (2003).

[16] N. Kivel and M. Vanderhaeghen, arXiv:hep-ph/090502822v1 (2009).

[17] W. K. Brooks *et al.*, "Beyond the Born approximation : A Precision Comparison of $e + p$ and $e - p$ Scattering in CLAS," Proposal for an Experiment E-04-116 at Jlab.

[18] L. W. Mo and Y. S. Tsai, Rev. Mod. Phys. **41**, 205 (1969).

[19] Y. S. Tsai, Phys. Rev. **122**, 1898 (1961).

[20] S. Kondratyuk *et al.*, Phys. Rev. Lett. **95**, 172503 (2005).

[21] S. Kondratyuk *et al.*, Phys. Rev. C **75**, 038201 (2007).

[22] Y. C. Chen *et al.*, Phys. Rev. Lett. **93**, 122301 (2004).

[23] A. V. Afanasev *et al.*, Phys. Rev. D **72**, 013008 (2005).

[24] Y. C. Chen *et al.*, arXiv:hep-ph/0403058 (2004).

[25] M. Kohl, "The OLYMPUS Experiment at DESY," International Workshop on Positrons at Jefferson Lab (2009).

[26] D. Yount and J. Pine, Phys. Rev. **128**, 1842 (1962).

[27] A. Browman, F. Liu, and C. Schaerf, Phys. Rev. **139**, 1079 (1965).

[28] R. L. Anderson *et al.*, Phys. Rev. Lett. **17**, 407 (1966).

[29] R. L. Anderson *et al.*, Phys. Rev. **166**, 1336 (1968).

[30] G. Cassiday *et al.*, Phys. Rev. Lett. **19**, 1191 (1967).

[31] W. Bartel *et al.*, Phys. Lett. B **25**, 242 (1967).

[32] B. Bouquet *et al.*, Phys. Lett. B **26**, 178 (1968).

[33] J. Mar *et al.*, Phys. Rev. Lett. **21**, 482 (1968).

[34] J. Arrington, arXiv:nucl-ex/0311019 (2004).

[35] B. A. Mecking *et al.*, Nucl. Instr. and Meth. A **503**, 513 (2003).

[36] D. I. Sober *et al.*, Nucl. Instr. and Meth. A **440**, 263 (2000).

[37] M. D. Mestayer *et al.*, Nucl. Instr. and Meth. A **449**, 81 (2000).

[38] G. Adams *et al.*, Nucl. Instr. and Meth. A **465**, 414 (2001).

[39] E. S. Smith *et al.*, Nucl. Instr. and Meth. A **432**, 265 (1999).

[40] M. Amarian *et al.*, Nucl. Instr. and Meth. A **460**, 239 (2001).

[41] "GEANT4 User's Guide for Application Developers," GEANT4 Collaboration (2009).

[42] V. Blobel, "The BOS System for CLAS Detector," CLAS Internal Document (1995).

[43] S. Stepanyan, "Simple Event Builder (SEB) in the Framework of RECSIS,"

`http://www.jlab.org/~stepanya/seb_man.html`

[44] D. Lawrence and M. D. Mestayer, "CLAS Drift Chamber Calibration Procedures," CLAS-NOTE **99-011** JLAB (1999).

[45] M. Moteabbed, "A Precise Seasurement of the Two Photon Exchange Effect," Ph.D. diss., Florida International University (2009).

[46] R. Feuerbach, "CLAS Drift Chamber Alignment Technique and Results," CLAS-NOTE **2001-22** JLAB (2001).

[47] S. A. Morrow and M. D. Mestayer, "Drift Chamber Alignment," CLAS-NOTE **2002-010** JLAB (2002).

[48] M. Bellis, Private communications.

[49] A. Tkabladze, Private communications.

[50] E. S. Smith *et al.*, "Calibration of the CLAS TOF System," CLAS-NOTE **1999-011** JLAB (1999).

[51] J. Lachniet, "A High Precision Measurement of the Neutron Magnetic Form Factor Using the CLAS Detector," Ph.D. diss., Carnegie Mellon University (2005).

VITA

Megh Raj Niroula
Department of Physics
Old Dominion University
Norfolk, VA 23529

EDUCATION:

- Ph.D. Physics, Old Dominion University, Norfolk, Virginia anticipated 2010, "Beyond the Born Approximation: A Precise Comparision of e^+p and e^-p Elastic Scattering in CEBAF Large Acceptance Spectrometer (CLAS)," adviser Larry Weinstein
- M.Sc. Physics, Tribhuvan University, Kathmandu, Nepal, 1998
- B.Sc. Physics, Tribhuvan University, Kathmandu, Nepal, 1996

EXPERIENCE:

- 2003 - Present: Research Assistant, Old Dominion University, Norfolk, VA
- 2001 - 2003: Part time Lecturer of Physics, Department of Physics, Amrit Campus, Kathmandu, Nepal
- 2001 - 2002: Assistant Lecturer of Physics, Brookfield Academy, Kathmandu, Nepal
- 2000 - 2003: Physics Teacher, Sathya Sai Shiksha Sadan, Kathmandu, Nepal

Typeset using LaTeX.